공학박사학위논문

소듐 이온 전지에서 음이온 산화 환원 반응에 의해 작동되는 $Na(Li_{1/3}Mn_{2/3})O_2$ 양극재의 멀티스케일 설계

Multiscale Design of $Na(Li_{1/3}Mn_{2/3})O_2$ Cathode Material Operated by Anionic Redox Reactions for Sodium-Ion Batteries

2018 년 2 월

서울대학교 대학원

기계항공공학부

김 두 호

서울대학교
SEOUL NATIONAL UNIVERSITY

Abstract

To discover new high-energy-density cathode materials for sodium-ion batteries (SIBs), multiscale design is highly considered to be an essential manner because cathode materials occur in complicated physical and chemical reactions from atomic scale to macro scale. Considering the intrinsically larger ionic radius of Na^+ than that of Li^+, cathode materials for SIBs are operated by electrochemical reactions accompanied by severe structural changes and phase transformations in comparison to those for lithium-ion batteries (LIBs) owing to insertion and extraction of Na^+, which leads to cyclic degradation during charge/discharge. That is, the Na-migration affect qualitative and quantitative variations of cathode materials in atomic scale, which are the results of electrochemical performance for the overall system. In addition, the intrinsically lower redox window (by ≈ 0.3 V) of the cathode for SIBs compared to the LIBs result in low-energy-density properties. Therefore, multiscale-based analysis and design approach in light of the two intrinsic features of Na^+ are critical for the rational design of cathode materials for SIBs.

Using the multiscale-based framework from first-principles calculations including thermodynamic mixing enthalpies associated with phase stabilities, kinetic properties, mechanical constants, chemomechanical strain, and qualitative and quantitative electronic structures in the perspective of atomic scale not only to phase separation kinetic simulations consisting of homogeneous chemical potentials originating from homogeneous free energy coupled with the thermodynamic values of atomic calculations, but also to

chemomechanical stress obtained by the fitted mechanical constants and chemomechanical strain using polynomial functions, we rationally design and experimentally realize $Na(Li_{1/3}Mn_{2/3})O_2$ as a high-energy-density cathode material ($\approx$4.2 V versus Na/Na^+ with a high charge capacity of 190 mAh g^{-1}) operated by the new reaction paradigm (anionic redox: O^{2-}/O^-) beyond the conventional reaction mechanism (cationic redox: $M^{n+}/M^{(n+1)+}$, M: transition metals) for sodium-ion batteries (SIBs), which is fundamentally inspired by in-depth understandings of Li_2MnO_3 redox reactions for LIBs. Furthermore, this rationally designed $Na(Li_{1/3}Mn_{2/3})O_2$ is an example of a new class of promising cathode materials, $Na(Li_{1/3}M_{2/3})O_2$ (M: transition metals featuring stabilized M^{4+}), for further advances in SIBs.

To overcome the drawbacks of phase change and separation, and structural collapse related to cyclic performance in the newly discovered $Na(Li_{1/3}Mn_{2/3})O_2$ material, we further design high-energy-density cathode, $Na(Li_{1/3}Mn_{1/2}Cr_{1/6})O_2$, utilizing the Cr 3$d$-electron and labile O 2$p$-electron for electrochemical reactions with reduced phase change, slow phase separation kinetics, and lower chemomechanical strain and stress compared to those of $Na(Li_{1/3}Mn_{2/3})O_2$. Additionally, to provide rational insights into the use of anionic redox reactions for future sodium-ion batteries, $Na(Li_{1/3}Mn_{1/2}Cr_{1/6})O_2$ is regarded as an exciting example of superior $Na(Li_{1/3}M_{2/3(1-y)}M_{cy})O_2$ analogues (M and M_c: transition metals with stabilized M^{4+} species and with cationic redox active M_c^{4+} species) with good cyclic performance.

서울대학교
SEOUL NATIONAL UNIVERSITY

The rationally designed and experimentally validated cathode materials by the multiscale-based design approach open an exciting direction to break the energy density limit of cathode materials for SIBs. Furthermore, the present multiscale-based design approach could be applied to various energy-related systems such as batteries, capacitors, fuel cells, solar cells, and even catalyst in order to improve their performance and rationally design new materials.

서울대학교
SEOUL NATIONAL UNIVERSITY

CONTENTS

Abstract

서울대학교
SEOUL NATIONAL UNIVERSITY

Chapter 4 Methodologies for Multiscale Design 83

서울대학교
SEOUL NATIONAL UNIVERSITY

LIST OF FIGURES

서울대학교
SEOUL NATIONAL UNIVERSITY

xvi

LIST OF TABLES

Chapter 1

Introduction

1.1 Electrodes for Batteries

Rechargeable batteries such as lithium- and sodium-ion batteries (LIBs and SIBs) have been considered as the most promising power sources for several decades; they have been widely used in applications ranging from portable electronics to large-scale energy storages such as electric vehicles (EVs) and energy storage systems (ESSs).[2-4] Especially, SIBs have been highlighted as promising candidates for these applications because of the availability and low-cost of sodium, as well as the similar electrochemistry to the well-established LIB technology.[3, 5-8] As presented in Figure 1.1, LIBs and SIBs are electrochemically working by migration of charge carriers (Li^+ and Na^+) across the electrolyte located between positive electrode (cathode) and negative electrode (anode).[9]

Based on this working mechanism, high capacity indicates the capability of containing large amount of Li^+ or Na^+ in the cathode and anode, and high

1

voltage refers to the high electrochemical potential when Li^+ or Na^+ is inserted (lithiation or sodiation) and extracted (delithiation or desodiation) from the cathode and anode in the theoretical manner; and, high capacity and voltage means high energy. Furthermore, cyclic performance and voltage drop originate from phase and structural stability of cathode and anode during electrochemical reactions.[10-15] Finally, power characteristics is dependent upon the rate of Li^+- or Na-migration, which is mostly determined by ionic and electronic conductivity.[16-19] Therefore, the electrochemical performance of LIBs and SIBs are affected these whole factors synthetically.

1.2 Issues and Challenges for Sodium-Ion Batteries

There are much more critical issues and challenges to improve and design the electrodes for electrochemical energy storages such as the capability for containing Na^+,[20-21] electrochemical potential of insertion and extraction,[22-23] phase stabilities,[24-26] ionic and electronic conductivities,[27] and additionally low cost and environmental friendliness for SIBs than for LIBs,[28-29] because the intrinsically larger size of the sodium ion compared to that of the lithium ion induces the large volume change (> 10%) and the phase instability of the desodiated structures during electrochemical reaction process.[5] Moreover, considering the intrinsically lower voltage window (by ≈0.3 V) of the cathode for SIBs in comparison to the LIBs, realizing high energy density is considered

서울대학교
SEOUL NATIONAL UNIVERSITY

to be one of the major challenges.[3]

In the perspective of theoretical investigation and design, the amount of Na^+ in the electrodes is relevant to the formation energy with respect to the content of Na^+, and electrochemical potential could be determined by thermodynamic phase stability versus the content of Na^+. Cyclic performance is closely related to phase transformations and structural instability of electrodes, which is relevant to thermodynamic and kinetic stability of structures during charge and discharge.[30-35] For the power characteristics, ionic conductivity is determined by migration of Na^+ inside the structure, which means that migration barrier, length, and space are important factors.[36] Finally, electronic conductivity can be predicted and tuned by band gap of electronic structures for electrode systems.[37]

These can be calculated by atomic scale simulations such as first-principles calculations, molecular dynamics, and statistical thermodynamics. For the particle-level phenomena, phase field simulations are necessary to predict phase behaviors by Na-extraction, using the bridged homogeneous bulk free energy based on the atomic scale physics for constituting governing equation of phase field model.

1.3 Multiscale-based Analysis and Design

As an in-depth theoretical approach, multiscale-based analysis and design have

been considered to be significantly essential and important manner for complicated systems including diverse physical, chemical, electrical, and mechanical phenomena in terms of wide range of length and time scales in many industrial applications such as energy materials, biomaterials, composite materials, electronic materials, and so on.[38-47] For the various research fields, a lot of methodologies combined atomic scale to macroscale simulations with scale bridging models have been studied for the development and utilization to improve their performance, since the multiscale problem cannot be solved by a single method in a scale. To calculate material properties in atomic scale, first-principles calculations, molecular dynamics, and Monte Carlo simulations have been used,[48-50] and phase field simulations and diverse statistical approaches have been employed for mesoscale problems;[51-56] then, micromechanics,[57-58] electrochemical models,[59-61] continuum mechanics,[62-64] heat and mass transfer,[65-66] thermal expansion,[67-68] and fluid mechanics[69-70] have been utilized for macroscale simulations.

Recently, among the abovementioned multiscale problems, a growing demand for large-scale energy storage applications (electric vehicle and grid electric energy storage systems) has progressed rapidly to study multiscale-based approaches to energy-related materials for electrochemical energy storages (e.g., cathodes, anodes, electrolyte, and etc.); and this methodology is indispensable, because they indicate that electro-chemo-mechanical coupled reactions

4

(multiphysics) take place in atomic structures, resulting in electrochemical performance in macroscale. For example, Figure 1.2 presents the schematic description of the cathode electrode ($LiFePO_4$) at various scales.[71] In the nanoscale, non-porous $LiFePO_4$ crystals represent the smallest scale observed, whereas the porous agglomerates represent the second size scale. The third size scale is the positive electrode itself, which consists of carbon black, binder and the porous agglomerates of the $LiFePO_4$ particles. In other words, different kinds of methodologies and approaches in diverse scales should be carried out to analyze and design the complex system of battery electrodes.

1.4 Objectives and Contributions

In this dissertation, based on multiscale design utilizing first-principles calculations, electronic structures, crystal field theory, ligand field theory, homogeneous free energies and chemical potentials, chemomechanical strain and stress, and phase field simulations, we introduce a new paradigm (anionic redox: O^{2-}/O^-) beyond the conventional working mechanism (cationic redox: $M^{n+}/M^{(n+1)+}$, M: transition metals) for high-energy-density cathodes in SIBs and enable a new class of promising battery materials for further advances in SIBs.[1]

From first-principles calculations consisting of thermodynamic mixing enthalpies related to phase stability, kinetic characteristics, mechanical constants,

5

chemomechanical strain and stress, and qualitative and quantitative electronic structures, atomistic properties can be predicted. For the multiscale methodology, homogeneous free energy is coupled with the thermodynamic energy value, evaluating homogeneous chemical potentials and mesoscale phase separation behaviors of electrodes for electrochemical reactions; furthermore, homogeneous chemomechanical stress can be obtained by fitted mechanical constants and chemomechanical strain using polynomial functions.

Using these methodologies, we rationally designed and experimentally realized high-energy-density cathode materials operated by the new reaction mechanism for SIBs such as $Na(Li_{1/3}Mn_{2/3})O_2$ and $Na(Li_{1/3}Mn_{1/2}Cr_{1/6})O_2$, which is inspired by detailed understandings of Li-rich manganese oxide (Li_2MnO_3) redox reactions; furthermore, we provided a new class of promising cathode materials, $Na(Li_{1/3}M_{2/3})O_2$ (M: transition metals featuring stabilized M^{4+}), and advanced $Na(Li_{1/3}M_{2/3(1-y)}M_{cy})O_2$ analogues (transition metals featuring cationic redox active M_c^{4+}).

In conclusion, the newly discovered cathode materials by the present multiscale-based design with experimental validations open an exciting direction to break the energy density limit of positive electrodes for SIBs without many experimentally empirical approaches. Finally, the experimentally successful material developments on the basis of theoretical design could be one of the most effective paradigm for the future innovative materials.

6
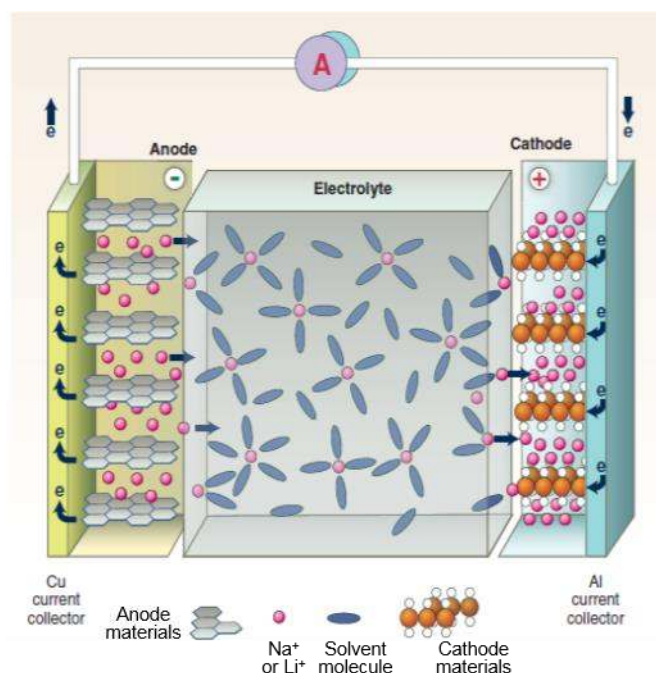
Figure 1.1 The negative electrode is a graphitic carbon that holds Li or Na in its layers, whereas the positive electrode is a Li- or Na-intercalation compound, usually an oxide because of its higher potential, that often is characterized by a layered structure. Both electrodes are able to reversibly insert and remove Li or Na ions from their respective structures. On charging, Li or Na ions are removed or deintercalated from the layered oxide compound and intercalated into the graphite layers. The process is reversed on discharge. The electrodes are separated by a nonaqueous electrolyte that transports Li or Na ions between the electrodes. The schematic figure is slightly modified from the original figure.
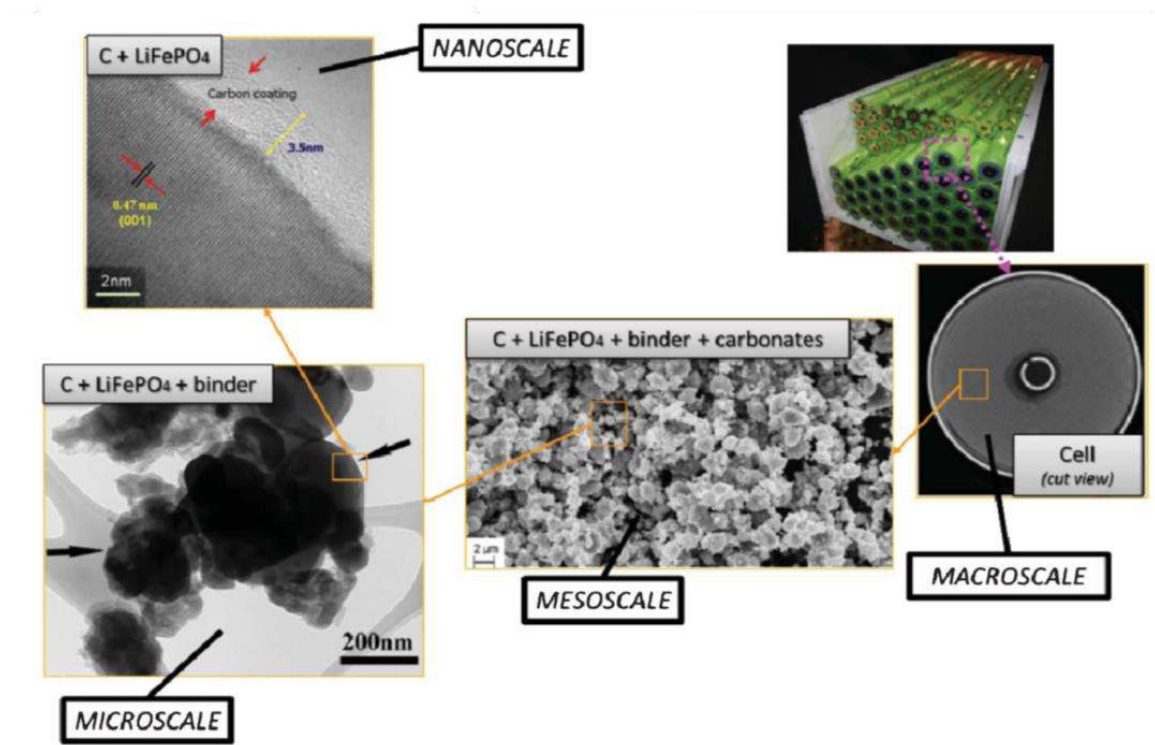
Figure 1.2 Schematics of the multiscale character of a LiFePO$_4$ electrode in a lithium-ion battery and physicochemical mechanisms. Schematics made with transmission electron microscopy and scanning electronic microscopy pictures and from the spiral battery tomography picture.

Chapter 2

Multiscale Design and Realization of Na(Li$_{1/3}$Mn$_{2/3}$)O$_2$[1]

2.1 Theoretical Design of Na(Li$_{1/3}$Mn$_{2/3}$)O$_2$

The crystal structure of pristine Li$_2$MnO$_3$ (denoted as Li(Li$_{1/3}$Mn$_{2/3}$)O$_2$, Figure 2.1a) reveals that the Li corresponding to the 2c and 4h are in the Li layer, whereas those in the 2b site are positioned in the Li$_{1/3}$Mn$_{2/3}$O$_2$ mixed layer and are surrounded by six Mn, forming a periodic honeycomb-like arrangement. The relative site energies for Na at the different Li sites (Figure 2.1b-d) indicate that Na is highly preferred to be in the Li layer rather than in the mixed layer (Figure 2.1e).

In general, Li$_2$MnO$_3$ is considered to be electrochemically inactive because Mn^{4+} at the octahedral site is difficult to further oxidize to Mn^{5+} for the octahedral geometry, on the basis of crystal field theory of stable t_{2g}^{3} e_g^{0} configuration of Mn^{4+}. However, the delithiation reaction above 4.5 V versus

9

Li/Li$^+$ occurs with an anionic redox (i.e., O^{2-}/O$^-$). Considering the intrinsically lower redox window (by $\approx$0.3 V) of the cathode for SIBs in comparison to the LIBs, along with the calculated site energy of Na, we predict that the theoretically optimized compound, Na(Li$_{1/3}$Mn$_{2/3}$)O$_2$, would be an excellent potential cathode with high energy density for SIBs, because the intercalation reactions of Na could occur at a high voltage of 4.2 V versus Na/Na$^+$ delivering a high theoretical capacity of 285 mAh g^{-1} (if all the Na are utilized) accompanied by the anionic redox mechanism.

To confirm the predictions of high voltage and high capacity, detailed first principle calculations of the formation energy of mixing enthalpy were carried out to investigate the phase behavior depending on Na content, and to identify the most stable phase among the mixed structures. Figure 2.2a presents the mixing enthalpy as a function of the normalized Na content calculated by first principle method. This energy diagram predicts that Li$_{1-x}$Na$_x$Mn$_{0.5}$O$_{1.5}$ at x = 0.75 is the most thermodynamically stable phase, and its atomic structure is described in Figure 2.2b. Noticeably, all the Na atoms in the stable structure Li$_{0.25}$Na$_{0.75}$Mn$_{0.5}$O$_{1.5}$ are present in the Na layer, suggesting that it is not favorable for Na to occupy the mixed layer, consistent with the site preference of Na.

We have calculated the unit-cell volumes of all phases so that the thermodynamic energy diagram can be elucidated by the structural variations of

$Li_{1-x}Na_xMn_{0.5}O_{1.5}$ ($0 \leq x \leq 1.0$). The unit-cell volume tends to increase linearly as the Na content increases, which is also described using Vegard's law (Figure 2.3a). To further elucidate the structural changes, the lattice parameters were also calculated. The lattice constants linearly increase from $x = 0.0$ to $x = 0.75$, and for $x > 0.75$ different changes are observed (Figure 2.3b-d). Above the inflection point ($x = 0.75$), the a and b parameters increase sharply, whereas the c parameter increases at a slower rate. This finding implies that the substitution of Na in the LiO_2 layer is preferred to that in $Li_{1/3}Mn_{2/3}O_2$ layer, because the electrostatic interaction between the oxygen layers in layered transition-metal analogues are weak. On the other hand, considering that the transition metals form ionic-covalent bonds with six oxygens, which is much stronger than the electrostatic interactions for most oxides, we could conclude that Na-substitution in the $Li_{1/3}Mn_{2/3}O_2$ layer is thermodynamically unfavorable.

For a direct comparison, two kinds of average octahedral volumes (Figure 2.4) were calculated according to the Na content (Table 2.1). The MnO_6 volume changes only slightly with increasing Na content (octahedral volumetric strain (ε_V^O) = 0.0186), while the changes in the LiO_6/NaO_6 volumes (ε_V^O = 0.2605) are significant. This difference implies that the 2b site cannot accept Na easily due to the strong Mn-O bonds, which do not provide enough space for the larger ionic radius of Na^+; this explanation is also consistent with the behavior of the lattice constants (Figure 2.3).

To examine the thermodynamic stability of the identified $Na(Li_{1/3}Mn_{2/3})O_2$ during desodiation, we have calculated the formation energies of mixing enthalpy at vacancy concentration (x) in $Na_{1-x}(Li_{1/3}Mn_{2/3})O_2$ over the full range ($0 \leq x \leq 1.0$). Using the thermodynamic energy with varying x (Figure 2.2c), we can validate the behavior of the predicted desodiation potentials (≈ 4.2 V versus Na/Na^+). From the obtained mixing enthalpies, the sodium-deficient phases of $Na_{1-x}(Li_{1/3}Mn_{2/3})O_2$ ($0.167 \leq x \leq 0.333$) is predicted to be most stable and would be experimentally synthesized. Theoretical predictions show that these Na deficient phases are more thermodynamically stable than the fully sodiated structure of $Na(Li_{1/3}Mn_{2/3})O_2$ in contrast to the stable fully lithiated $Li(Li_{1/3}Mn_{2/3})O_2$. Figure 2.2d shows the desodation and delithiation potentials as a function of the inverse Na content (x) in $Na_{1-x}(Li_{1/3}Mn_{2/3})O_2$. Even though low redox potentials of Na are observed at the beginning of desodiation (shaded gray regions: below $x = 0.333$), subsequent redox potentials (≈ 4.2 V vs. Na/Na^+: above $x = 0.333$), and the theoretical capacity (≈ 190 mAh g^{-1}) are higher than formerly reported values of other cathodes for sodium-ion batteries.[72] As expected, the redox behavior of Li is similar to that of Na, at higher redox potentials. This shows that the simultaneous extraction of the Na-atoms and the Li-atoms occupying the mixed layer is unfavorable, because their redox windows are different, and only Na ions will participate the redox reactions of $Na_{1-x}(Li_{1/3}Mn_{2/3})O_2$.

2.2 Experimental Validation

In order to validate the theoretical predictions on the redox behavior of $Na(Li_{1/3}Mn_{2/3})O_2$, this oxide was synthesized by a solid-state reaction. Standard characterization of the synthesized powders were carried out by X-ray diffraction (XRD), inductively coupled plasma mass spectroscopy (ICP-MS), field-emission scanning electronic microscopy (FESEM), and transmission electron microscopy (TEM) studies (Figure 2.5). ICP-MS results were summarized and confirmed the amount of inverse Na (x = 0.24) in the as-prepared pristine sample (NLMO, see the details in Table 2.2), which was predicted to be the thermodynamically stable Na-deficient phases in Figure 2.2c. The XRD patterns of NLMO measured over 10°–80° are consistent with the reference data (PDF: 00-054-0839, Figure 2.5a). FESEM studies revealed an average particle size of ≈1 µm with spherical shape (Figure 2.5b). To confirm the elements of NLMO, energy dispersive X-ray spectroscopy (EDS) mapping was carried out, coupled with FESEM (Figure 2.5c), revealing that Mn (purple), O (red), and Na (green) were uniformly distributed in the sample. Furthermore, we have conducted EDS mapping coupled with scanning TEM (STEM) to examine the elemental distribution in a small region within NLMO (Figure 2.5d). To reduce the statistical error with respect to EDS mappings in STEM, several particles in the sample were observed (Figure 2.6), and EDS results were

13

summarized with elemental ratio (Figure 2.7).

Figure 2.8 shows the galvanostatic charge curve of NLMO without any technical treatment (e.g., carbon or oxide coating), combined with the theoretically calculated voltage profile for $Na_{1-x}(Li_{1/3}Mn_{2/3})O_2$ ($0 \leq x \leq 1.0$). An initial charge capacity of $\approx$150 mAh g^{-1} was observed with a large plateau at 4.2 V, which is in good agreement with the theoretically calculated predictions. To examine the lower redox potentials predicted by first principle calculations, we have conducted an electrochemical evaluation of charge cycle after the initial discharge to 1.5 V versus Na/Na$^+$ to further sodiate the synthesized Na-deficient NLMO (Figure 2.9). The observed lower redox potentials of $\approx$2.0 V versus Na/Na$^+$ at the initial charge profile agree quantitatively with the desodiation potentials predicted by theoretical calculations. Further electrochemical properties of NLMO have been investigated to examine consistent oxidation behaviors at various current densities (Figure 2.11).

2.3 Reaction Mechanism

To investigate the origin of the redox mechanism in $Na(Li_{1/3}Mn_{2/3})O_2$ during desodiation, detailed electronic structures of the oxide were examined. On the basis of the crystal field theory, the partial density of states (PDOS) of Mn in $Na(Li_{1/3}Mn_{2/3})O_2$ and $Li(Li_{1/3}Mn_{2/3})O_2$ present a typical charge order of Mn^{4+} at

14

high-spin states (Figure 2.12a,c). The $3d$ orbitals of Mn reveal the localized characteristic overlap with the dispersive $2p$ orbitals of O, leading to hybridized states with nondirectional bonding characteristics (π-bonding). For the direct visualization of π-bonding, calculations of spatial electron distribution (SED) from the wavefunctions were carried out for both $Na(Li_{1/3}Mn_{2/3})O_2$ and $Li(Li_{1/3}Mn_{2/3})O_2$. The SEDs around Mn and O were observed to form π-bonding (Figure 2.12b,d).

Figure 2.12a,c predicts that the redox activity of $Na(Li_{1/3}Mn_{2/3})O_2$ would originate from an anionic redox O^{2-}/O^- when Na is extracted, because some O $2p$-electron occupy higher energy states compared to Mn $3d$-electron in lower energy states, leading to unhybridized states (lone-pair O). Toward obtaining further information, we have calculated the SED from -2 to 0 eV in both $Na(Li_{1/3}Mn_{2/3})O_2$ and $Li(Li_{1/3}Mn_{2/3})O_2$. The isolated O $2p$-electron densities present features of lone-pair O with a linear shape along the direction of Na-O-Li (Figure 2.12e,f). Likewise, an isolated linear shape (Li-O-Li configuration) was observed in the same energy range for $Li(Li_{1/3}Mn_{2/3})O_2$ (Figure 2.12g,h). This finding indicates that the lone-pair O $2p$-electron of the Na-O-Li ($Na(Li_{1/3}Mn_{2/3})O_2$) and Li-O-Li ($Li(Li_{1/3}Mn_{2/3})O_2$) configurations will play a major role in the redox activity.

The Na-O-Li electronic distribution is closely related to the increase in the c-parameter with increasing Na content (Figure 2.3d). There are two types of

octahedrally coordinated oxygen atoms significant in this context: $O(Na_3Mn_2Li)_{L1}$ and $O(Na_3Mn_2Li)_{L2}$ (Figure 2.13a,b). The octahedral structure parameters are calculated and summarized in Table 2.3, along with the corresponding values for Li_2MnO_3 ($O(Li_4Mn_2)_{L1}$ and $O(Li_4Mn_2)_{L2}$ in Figure 2.13c,d). To gain a better understanding, the bond lengths of Li-O and Na-O in Na-O-Li configurations were investigated. When the Na content is increased, there is almost no change in the Li-O bond lengths, whereas the Na-O bond lengths increase significantly. These results could be explained by the linear shape of electronic distribution (Na-O-Li) and overlaps between the $2p$ orbitals of O and Na, which are mainly responsible for the increase in the c lattice parameter.

Considering that a further oxidation of Mn^{4+} $3d$-electron to Mn^{5+} is not favorable at the octahedral site, and that $Na(Li_{1/3}Mn_{2/3})O_2$ contains all Mn ions in Mn^{4+} oxidation state, we calculated the PDOS to investigate the fundamental redox mechanism during desodiation. Figure 2.14 covers the variations of the Mn $3d$- and O $2p$-electron during the Na-extraction, and all Mn (Figure 2.14a-g) show the Mn^{4+} charge order through Na-removal, while the O $2p$-electron is oxidized to compensate the charge imbalance induced by the Na-extraction (anionic redox O^{2-}/O^{-}). The SED in the range 0-1 eV above Fermi level from the $Na_{4/6}(Li_{1/3}Mn_{2/3})O_2$ structure shows that the oxidized O $2p$-electron around the vacancy was observed with the charge density of Na-O-Li (Figure 2.14h). This

implies that the labile Na-O-Li in $Na(Li_{1/3}Mn_{2/3})O_2$ is oxidized to compensate electronic charge during desodiation. For a quantitative investigation, the net charges of Mn and O were calculated (Figure 2.14i,j) in $Na_{1-x}(Li_{1/3}Mn_{2/3})O_2$ ($0 \leq x \leq 1.0$). Almost no change was observed for Mn, whereas a linear increase was observed for O. This finding is consistent with the calculated PDOS of Mn and O during the Na-extraction, which confirms the anionic redox of O^{2-}/O^-.

To experimentally confirm the valence state of Mn predicted by theoretical calculations, we conducted X-ray photoelectron spectroscopy (XPS) analysis, and all Mn $2p$ spectra were carefully fitted based on the C $1s$ spectra at 284.8 eV. The XPS results of NLMO and Li_2MnO_3 powders (Figure 2.15) reveal dominant peaks at 642.6 eV (purple) in the Mn $2p_{3/2}$ spectra, which correspond to the valence state of Mn^{4+}. To investigate the Mn valence state during desodiation, we carried out *ex-situ* XPS in NLMO at various stages: i) pristine, ii) charged to 4.15 V, iii) charged to 4.3 V, and iv) discharged to 1.5 V (Figure 2.14k). During desodiation to 4.3V, the major peaks at $\approx$642.6 eV (Mn $2p_{3/2}$ spectra) and 654.1 eV (Mn $2p_{1/2}$ spectra) were practically unchanged. These fixed valence states of Mn at the different states suggest that there is no redox reaction originating from Mn^{4+}/Mn^{5+}, which is in good agreement with the predicted electronic structures.

2.4 Establishing New Material Analogues

In-depth understanding of Li_2MnO_3 during delithiation for LIB cathodes is critical for the rational design of $Na(Li_{1/3}Mn_{2/3})O_2$ for high-energy-density SIB cathodes. Considering the site preference of Na in the Li_2MnO_3 structure, the thermodynamically stable structure of was $Na(Li_{1/3}Mn_{2/3})O_2$ obtained. As the intrinsically lower redox potentials for SIB cathodes compared to LIBs, $Na(Li_{1/3}Mn_{2/3})O_2$ showed a redox potential of ≈ 4.2 V versus Na/Na^+ without the creation of free volume in the mixed layer, because Li-extraction requires a higher voltage than Na-extraction. Interestingly, the anionic redox (O^{2-}/O^{n-}) beyond the conventional cationic redox ($M^{n+}/M^{(n+1)+}$, M: transition metals) was used to gain electrochemical capacity. Thus, our findings will not only enable new $Na(Li_{1/3}M_{2/3})O_2$ analogues (transition metals featuring stabilized M^{4+}) to break the energy density limit of positive electrodes for SIBs, but also provide an exciting direction for future electrochemical storage materials.

2.5 Challenges of $Na(Li_{1/3}Mn_{2/3})O_2$

In spite of a rigorously designed $Na(Li_{1/3}Mn_{2/3})O_2$ utilizing the anionic redox of O $2p$-electron of Na-O-Li configuration, two major challenges remain to enhance the electrochemical performance. First, in the perspective of maintaining a high-voltage region, it is expected that a two-phase reaction occurs mainly in the range from $x = 0.667$ to $x = 0.0$, generating both an inactive phase $Na_0(Li_{1/3}Mn_{2/3})O_2$ and an active phase $Na_x(Li_{1/3}Mn_{2/3})O_2$. The inactive

phase formation is derived from a phase separation (Figure 2.2c), which is shown in the charge-discharge profiles after the initial charge (Figure 2.16). Second, from the viewpoint of increasing the low-voltage region, a phase change from O3 to P2 from the region of initial desodiation could result in the electrochemical low-voltage because the deficient phases are much more stable than the fully sodiated phase (Figure 2.2c).

2.6 Multiscale Phase Field Simulation: Phase Separation

From the perspective of phase behaviors at meso-scale beyond atomic-scale, we carried out phase field simulations considering the two-phase reaction region for $Na_{1-x}(Li_{1/3}Mn_{2/3})O_2$ ($4/6 \leq x \leq 1.0$). The mesoscale phase separation behavior of the oxide was simulated based on the multiscale modeling on the phase transformation (see Chapter 4). This multiscale simulation bridged from first-principles calculations to the multiscale phase separation kinetics was adopted to predict and explain cyclic properties, closely related to phase behaviors depending on Na content, for $Na(Li_{1/3}Mn_{2/3})O_2$.

The phenomenological descriptions of the phase separation behaviors presented in Figure 2.17 could be understood considering the thermodynamic phase stabilities of $Na(Li_{1/3}Mn_{2/3})O_2$. The phase field simulations were performed with 50×50 computational cell at various initial compositions within the same

서울대학교
SEOUL NATIONAL UNIVERSITY

dimensionless time, and the phase separation was triggered by random noise. For the characteristic length, the nearest-neighbor distance of Na^+ (0.2811 nm) was obtained from the atomic structure of $Na_{1-x}(Li_{1/3}Mn_{2/3})O_2$ at $x = 5/6$; and we utilized the square-shaped nanodomains with the side of 14.06 nm.

During the first charge process, the phase of $Na(Li_{1/3}Mn_{2/3})O_2$ was separated to $Na_{2/6}(Li_{1/3}Mn_{2/3})O_2$ (active phase) and $Na_0(Li_{1/3}Mn_{2/3})O_2$ (inactive phase), as predicted by the thermodynamic mixing enthalpy values. The phase field simulation results depending on the normalized initial compositions can elucidate more specific the phase separation behaviors. Nucleation reaction considered to be formation of the inactive phase is generated, and then the phase separation reaction takes place because of spinodal instability during the desodiation process. Moreover, as the initial composition increases, the phase separation reaction rapidly occurs due to stiffer slope of chemical potential in the spinodal region. This phase separation is expected to generate the inactive phase, leading to cyclic degradation for $Na(Li_{1/3}Mn_{2/3})O_2$.
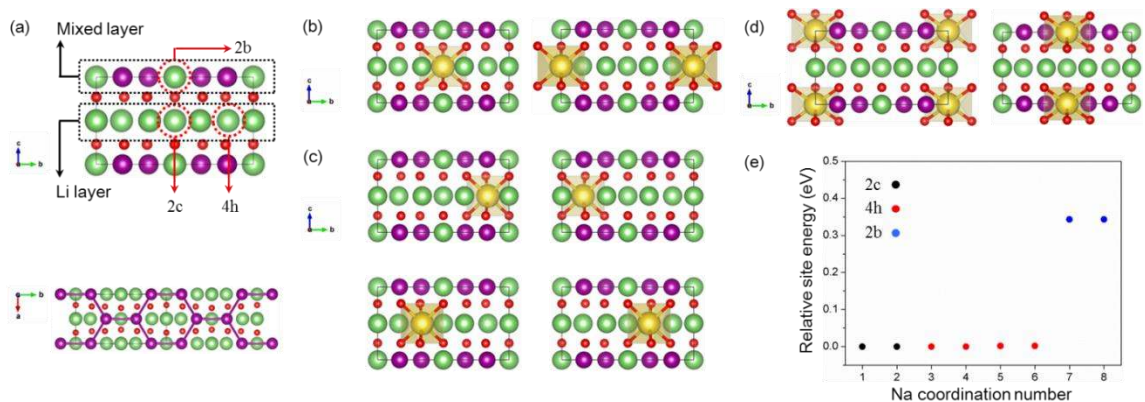
Figure 2.1 (a) The atomic model of Li_2MnO_3 consisting of Li layers and mixed layers shown in the [100] projection (top image) and [001] projection (bottom image). The atomic structures of Na substituted in (b) 2c, (c) 4h, and (d) 2b sites of Li_2MnO_3. (e) Relative energies according to the Na site dependence.
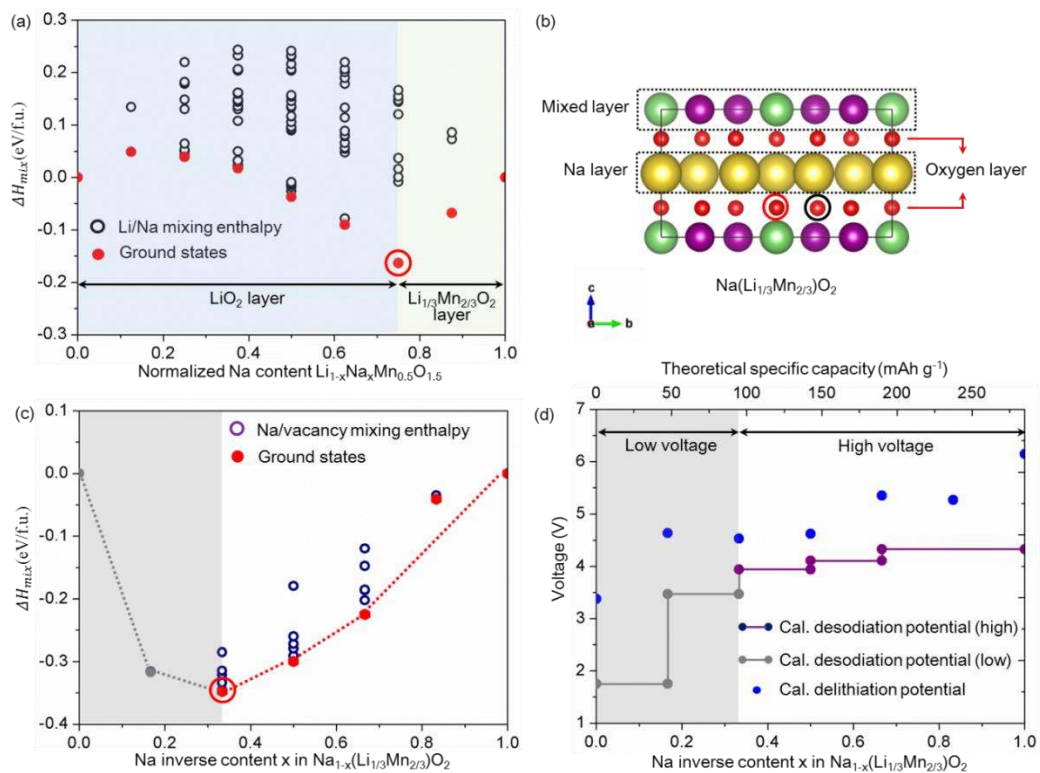
Figure 2.2 (a) Formation energies of mixing enthalpy for $Li_{1-x}Na_xMn_{0.5}O_{1.5}$ ($0 \leq x \leq 1.0$), considering all possible Li/Na atomic sites (i.e., 2b, 2c, and 4h sites). The ground states at each Na ratio are shown as red filled circles, and the red open circle indicates the most stable phase. (b) The atomic model at $x = 0.75$ in $Li_{1-x}Na_xMn_{0.5}O_{1.5}$ consisting of the Na layer and mixed layer (Li: green, Na: yellow, Mn: purple, and O: red). (c) Formation energies of mixing enthalpy considering all possible Na/vacancy atomic configurations for $0 \leq x \leq 1.0$ in $Na_{1-x}(Li_{1/3}Mn_{2/3})O_2$ (ground states at each ratio are shown as red filled circles). (d) Calculated desodiation potentials (purple and gray filled circle connected by lines) and delithiation potentials (blue filled circle) with the removal of Na or Li in $Na_{1-x}(Li_{1/3}Mn_{2/3})O_2$.
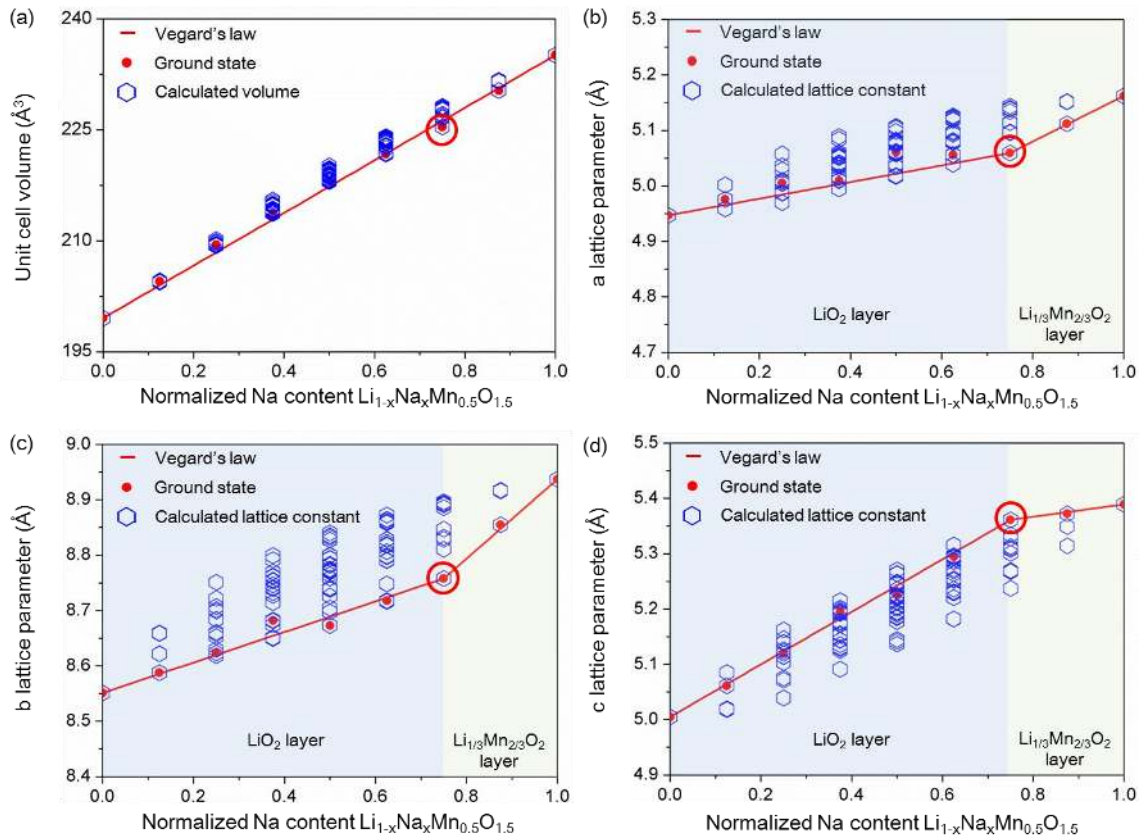
Figure 2.3 (a) Unit cell volumes, and the lattice parameters (b) *a*, (c) *b*, and (d) *c* as a function of normalized Na content in $Li_{1-x}Na_xMn_{0.5}O_{1.5}$. The parameters at the ground states are shown as red filled circles.
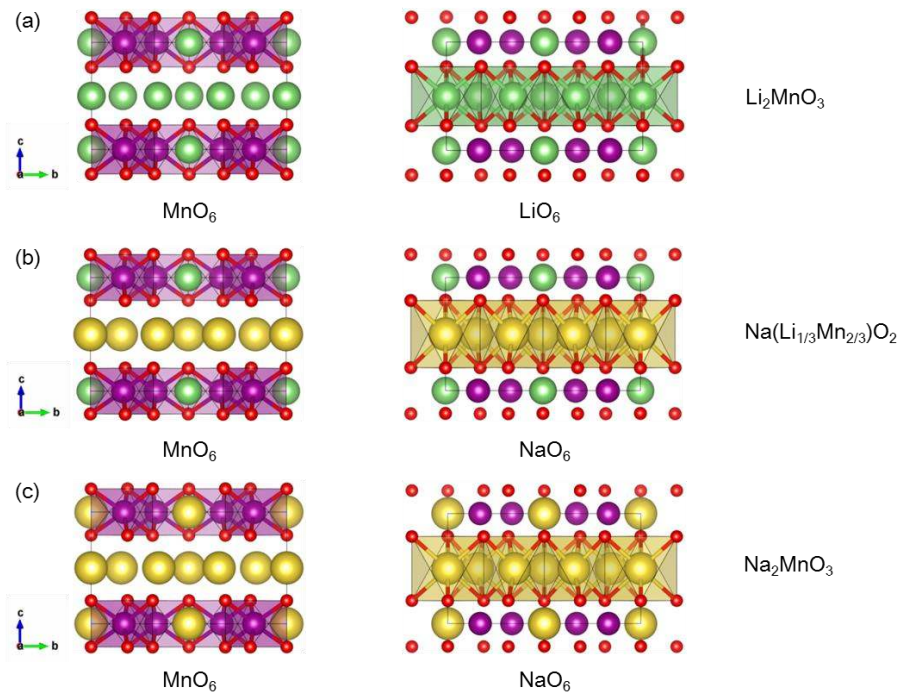
Figure 2.4 (a) MnO_6 octahedra in the mixed layer (left image, $Li_{1/3}Mn_{2/3}O_2$ layer) and LiO_6 octahedra in the Li layer of $Li(Li_{1/3}Mn_{2/3})O_3$. (b) MnO_6 octahedra in the mixed layer (left image, $Li_{1/3}Mn_{2/3}O_2$ layer) and NaO_6 octahedra in the Na layer of $Na(Li_{1/3}Mn_{2/3})O_2$. (c) MnO_6 octahedra in the mixed layer (left image, $Na_{1/3}Mn_{2/3}O_2$ layer) and NaO_6 octahedra in the Na layer of $Na(Na_{1/3}Mn_{2/3})O_3$.
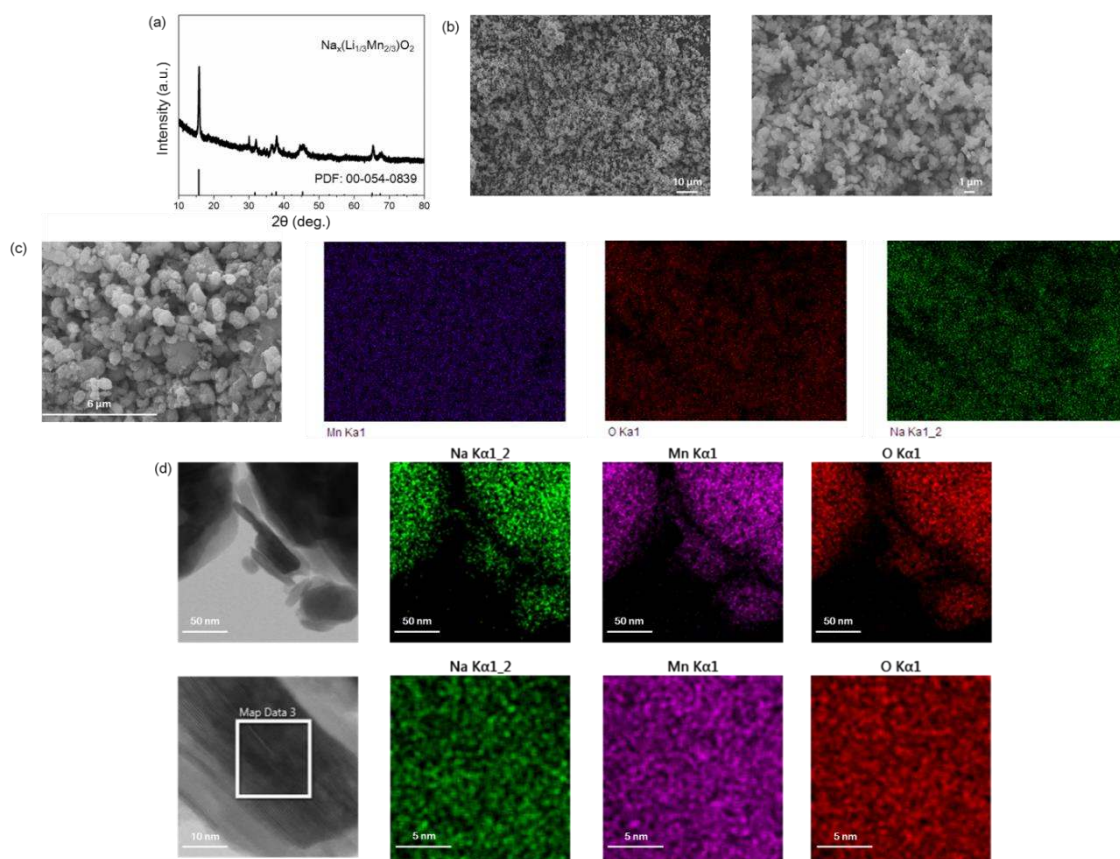
Figure 2.5 (a) XRD patterns of the pristine sample (x = 0.76 in Na$_x$(Li$_{1/3}$Mn$_{2/3}$)O$_2$ (NLMO)). (b) Low and high magnification FESEM images of NLMO. (c) FESEM image of NLMO and the corresponding EDS elemental mapping of Mn (purple), O (red), and Na (green). (d) STEM image of NLMO, and the corresponding EDS elemental mapping of Na (green), Mn (purple), and O (red), along with the magnified image of the sample (with EDS mapping).
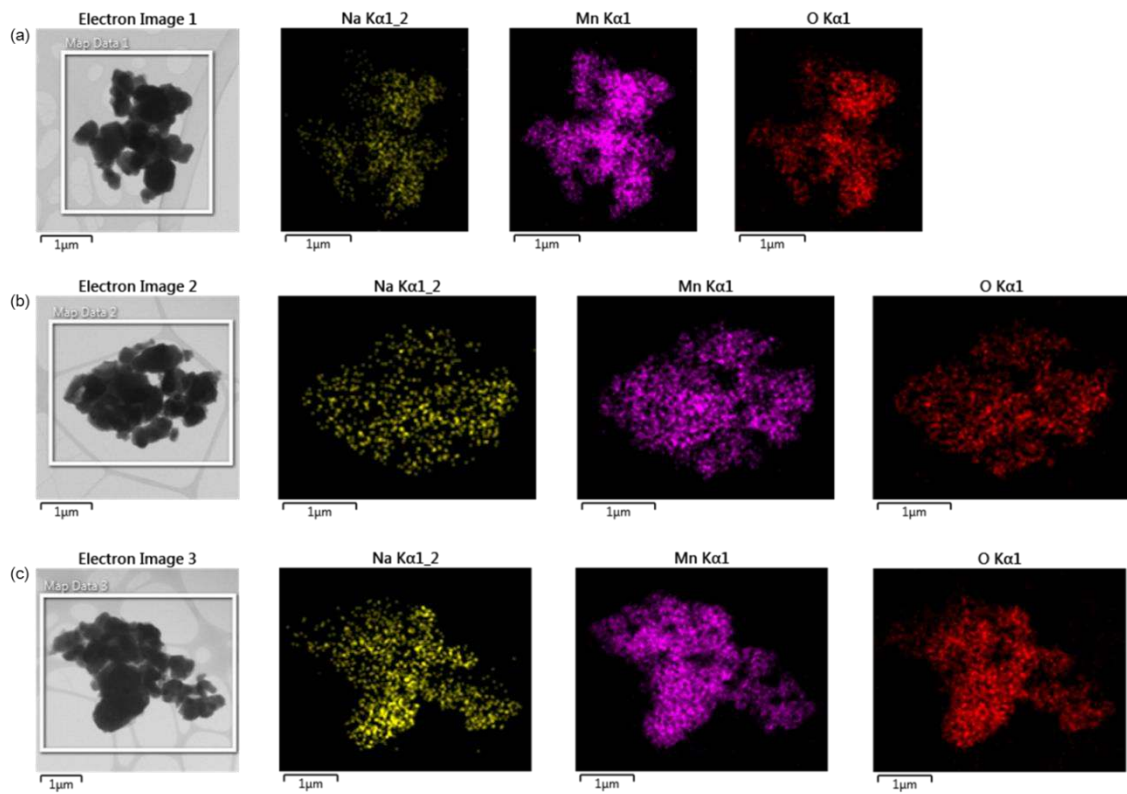
Figure 2.6 Various regions ((a), (b), and (c)) in the NLMO sample were examined to confirm the homogeneous distribution of elements (Na: yellow, Mn: purple, and O: red).

Element	Wt%	At%
O K	33.23	55.80
Na K	17.00	19.86
Mn K	49.77	24.34

Element	Wt%	At%
O K	36.23	57.31
Na K	20.80	22.90
Mn K	42.97	19.80
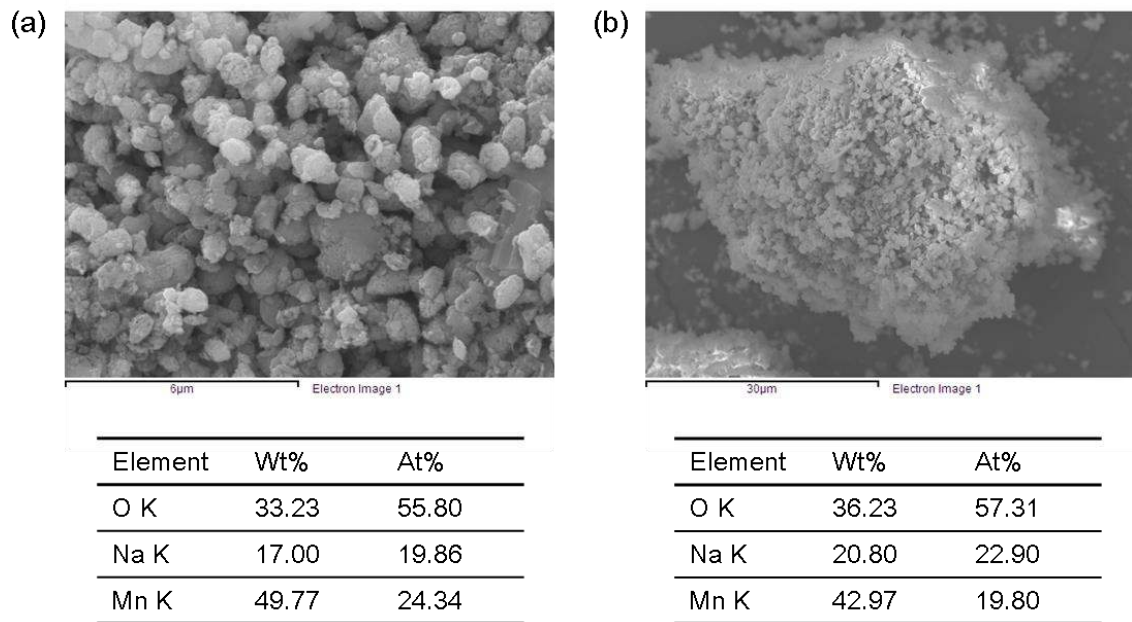
Figure 2.7 (a, b) FESEM images of NLMO samples with the corresponding EDS results.
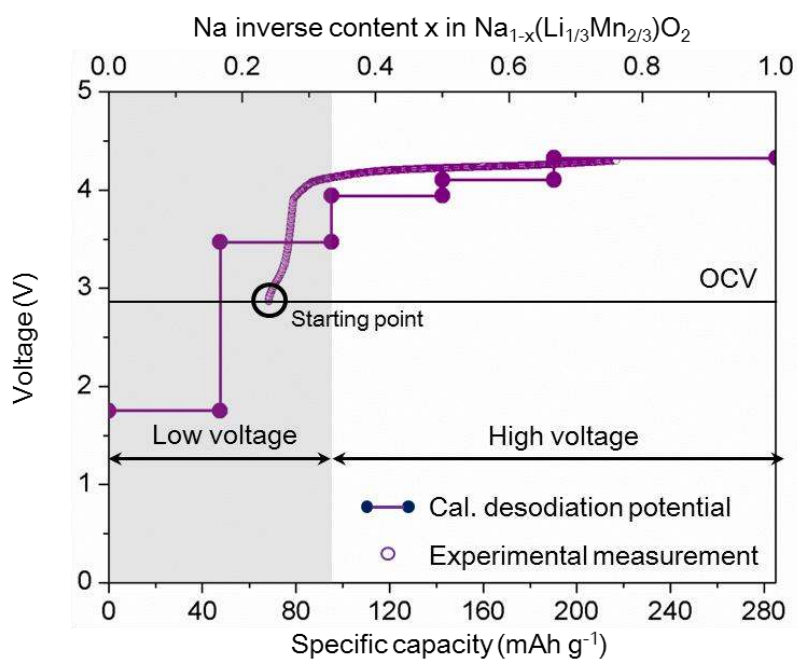
Figure 2.8 Electrochemical behaviors of NLMO. A combined graph of the galvanostatic charge profile of NLMO to 4.3 V *vs.* Na/Na$^+$ with a current density of 10 mA g^{-1} at room temperature, with theoretically calculated desodiation potentials for Na$_{1-x}$(Li$_{1/3}$Mn$_{2/3}$)O$_2$ ($0.0 \leq x \leq 1.0$).
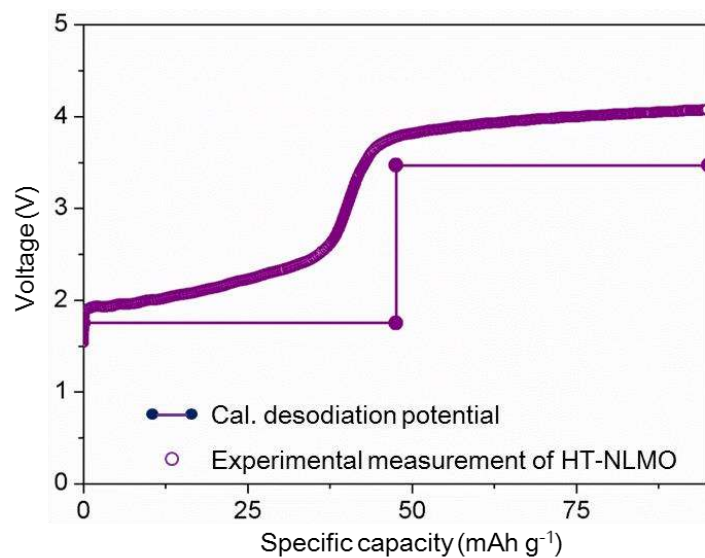
Figure 2.9 After the discharge to 1.5 V *vs*. Na/Na$^+$, the measured charge profile of NLMO synthesized at 850 ℃ (denoted as HT-NLMO, see the details in Figure 2.10) with the calculated potentials for the low voltage region as indicated in Figure 2.2.

서울대학교
SEOUL NATIONAL UNIVERSITY
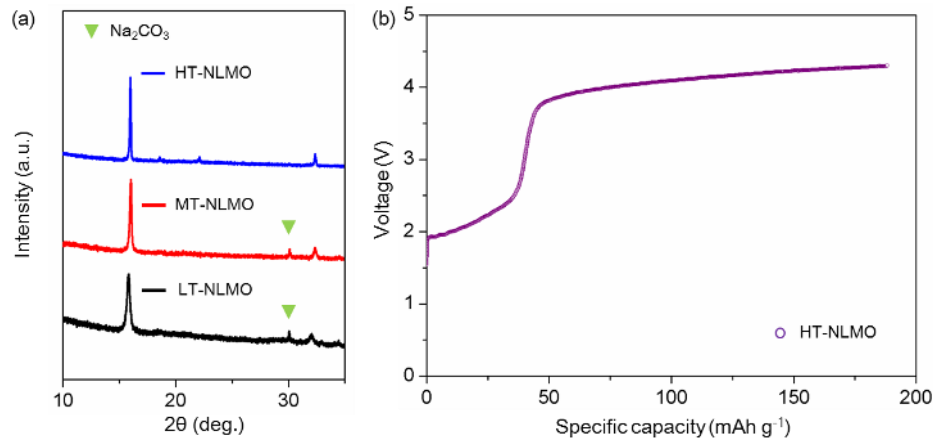
Figure 2.10 (a) XRD patterns of the NLMO samples synthesized at 450 (LT-NLMO), 650 (MT-NLMO), 850 ℃ (HT-NLMO). The observed Na_2CO_3 peak at around 30 degree in LT- and MT-NLMO is not present in HT-NLMO sample. The clearly observed two peaks between 18 and 24° are expected to be the presence of $LiMn_6$ in the mixed layers, positioning lower angles compared to those in HT-Li_2MnO_3 due to the enlarged interlayer d-spacing by Na^+. (b) After the discharge to 1.5 V vs. Na/Na^+, the measured charge profile of HT-NLMO to 4.3 V vs. Na/Na^+.
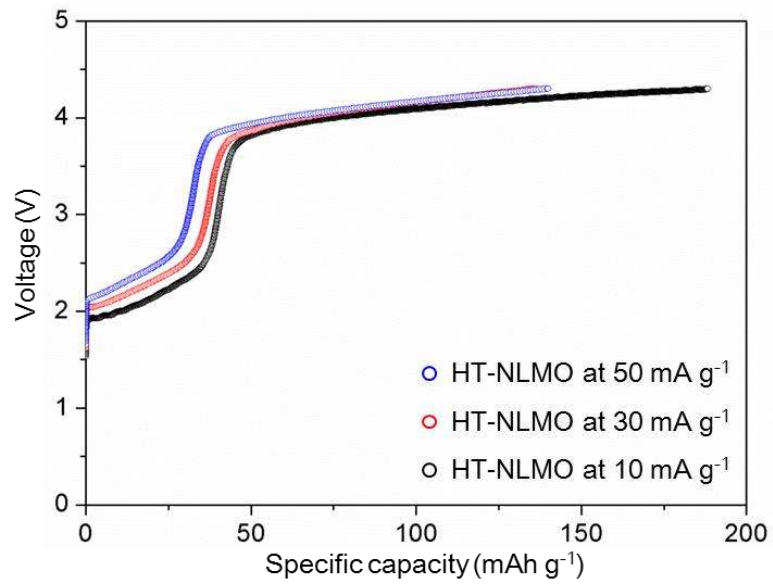
Figure 2.11 After the discharge to 1.5 V *vs*. Na/Na$^+$, the measured charge profiles of HT-NLMO with the various current densities of 10, 30, and 50 mA g^{-1}.
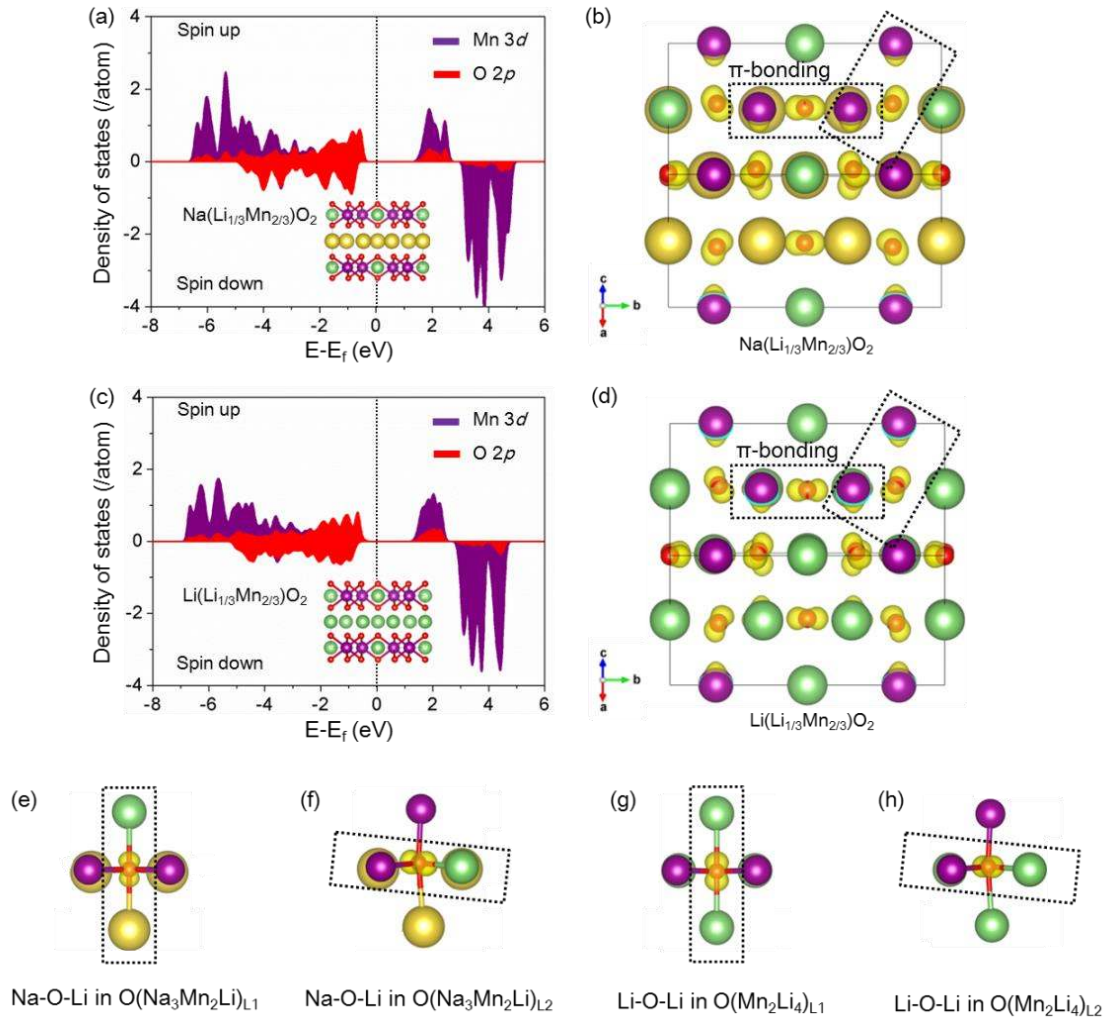
Figure 2.12 Electronic structures in $Na(Li_{1/3}Mn_{2/3})O_2$ and $Li(Li_{1/3}Mn_{2/3})O_2$. Combined graphs of partial density of states (PDOSs) of Mn $3d$ orbital electrons (purple) and O $2p$ orbital electrons (red) in (a) the fully sodiated $Na(Li_{1/3}Mn_{2/3})O_2$ and, (c) the fully lithiated $Li(Li_{1/3}Mn_{2/3})O_2$. The PDOS of Mn in both the oxides present d_{xy}, d_{yz}, and d_{xz} orbitals in the t_{2g} band (spin-up electrons, t_{2g}^3). Spatial electron distribution in the occupied band from -8 to -2 eV of, (b) $Na(Li_{1/3}Mn_{2/3})O_2$ and (d) $Li(Li_{1/3}Mn_{2/3})O_2$. Local spatial electron

32

distribution in the occupied band from -2 to 0 eV (Fermi level) for the two kinds ((e) O in black circle and (f) O in red circle from Figure 2.2b) of O coordinated by three Na, two Mn, and one Li in the structure of $Na(Li_{1/3}Mn_{2/3})O_2$, and the distribution in the same range for the two O ((g) O in black circle and (h) O in red circle from Figure 2.2b) surrounded by four Li and two Mn in the structure of $Li(Li_{1/3}Mn_{2/3})O_2$.
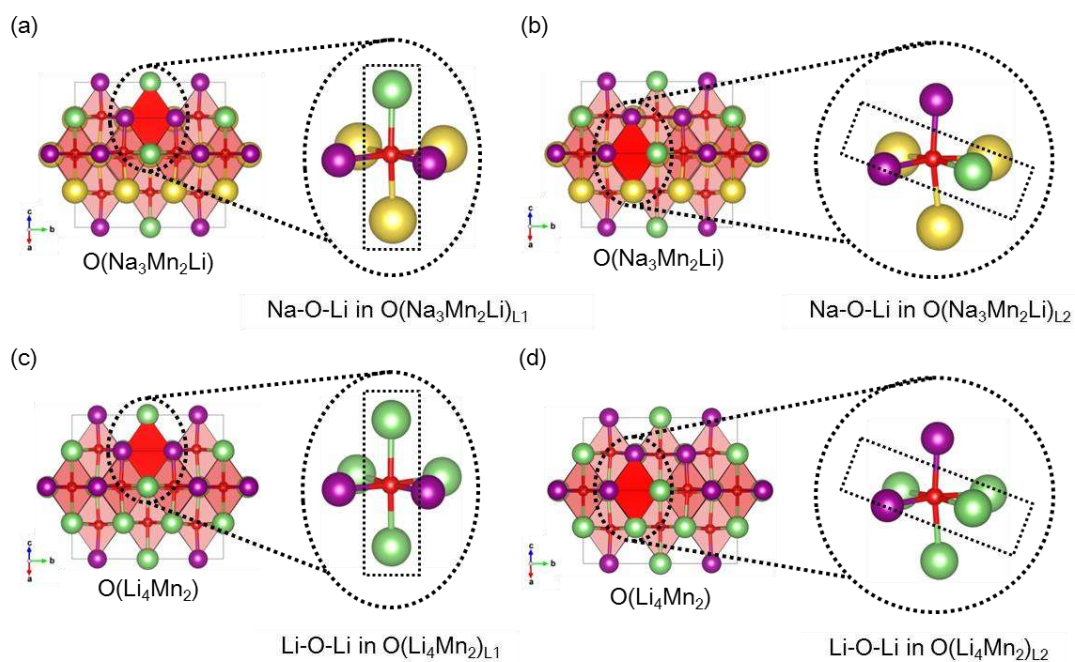
Figure 2.13 Octahedra of O (O in black circle (**a**) and O in red circle (**b**) from Figure 2.2b) coordinated by three Na, two Mn, and one Li in $Na(Li_{1/3}Mn_{2/3})O_2$. The corresponding local structures of $O(Na_3Mn_2Li)$ are presented as magnified images in dotted circles. These octahedral viewpoints are also described for $Li(Li_{1/3}Mn_{2/3})O_2$. Octahedra of O (O in black circle (**c**) and O in red circle (**d**) from Figure 2.2b) coordinated by four Li and two Mn in $Li(Li_{1/3}Mn_{2/3})O_2$.
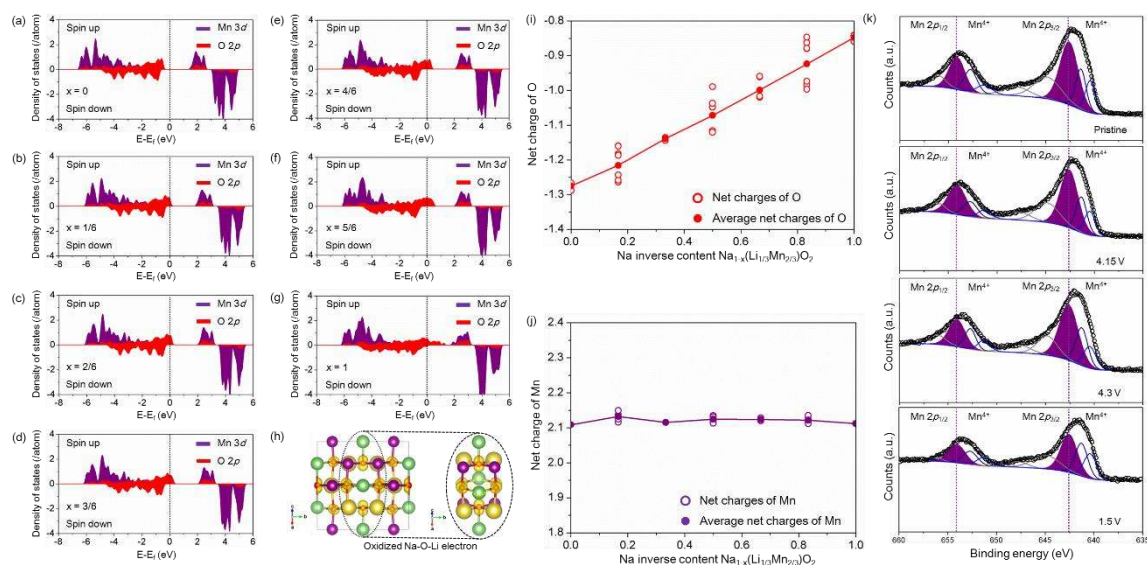
Figure 2.14 Mn 3*d*- and O 2*p*-electron variations during desodiation. Combined graphs of partial density of states (PDOSs) of Mn 3*d* orbital electrons (purple) and O 2*p* orbital electrons (red) from (a) $x = 0.0$ to (g) $x = 1.0$ in Na$_{1-x}$(Li$_{1/3}$Mn$_{2/3}$)O$_2$. h) Spatial electron distribution in the unoccupied band from 0–1 eV in Na$_{4/6}$(Li$_{1/3}$Mn$_{2/3}$)O$_2$, and the yellow dotted circle indicates a vacancy by the Na-extraction. Calculated net charges, based on Bader charge analysis, of (i) O and (j) Mn as a function of Na inverse content (x) in Na$_{1-x}$(Li$_{1/3}$Mn$_{2/3}$)O$_2$. (k) Mn valence state investigations. XPS spectra of Mn 2*p* in pristine NLMO, charged to 4.15 V, charged to 4.3 V, and discharged to 1.5 V vs. Na/Na$^+$.
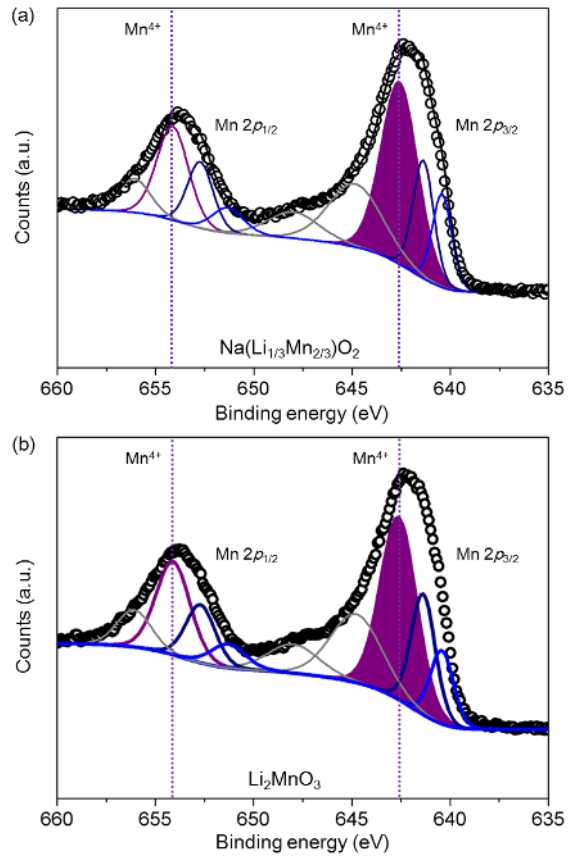
Figure 2.15 XPS spectra of Mn $2p$ in Na(Li$_{1/3}$Mn$_{2/3}$)O$_2$ and Li$_2$MnO$_3$ powders.
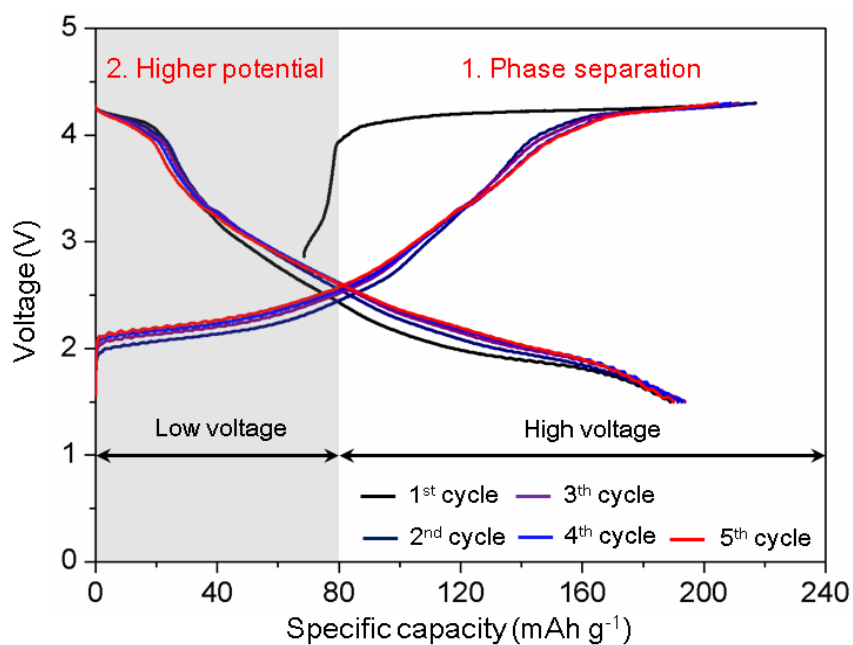
Figure 2.16 Charge-discharge profiles of NLMO from 1.5 V to 4.3 V *vs.* Na/Na$^+$ with a current density of 10 mA g^{-1} at room temperature during 5 cycles.
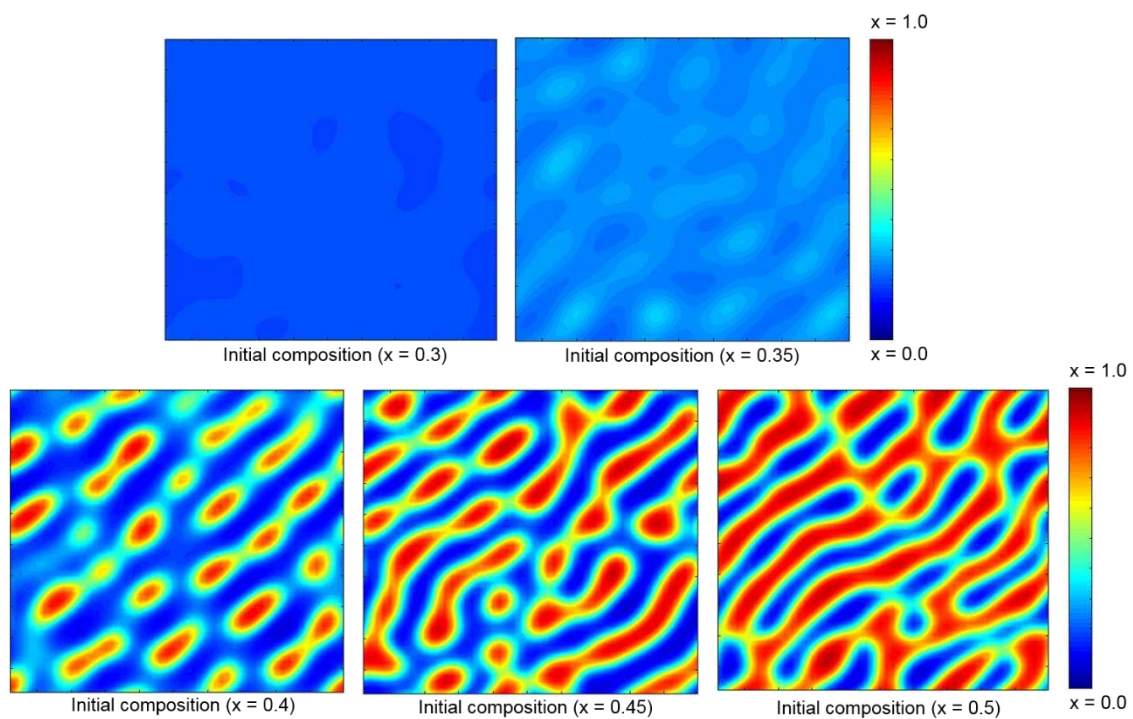
Figure 2.17 Results of phase separation kinetic simulations depending on the normalized initial compositions in $Na(Li_{1/3}Mn_{2/3})O_2$ during relaxation from a solid solution. The color bar indicates the normalized inverse Na content between $x = 4/6$ and $x = 1.0$ in $Na_{1-x}(Li_{1/3}Mn_{2/3})O_2$.

Table 2.1 Calculated average octahedral volume: i) MnO_6 in the mixed layer, ii) LiO_6 and NaO_6 in the Li layer according to Na content in $Li_{1-x}Na_xMn_{0.5}O_{1.5}$ (see Figure 2.3).

Compound	Na content	Average octahedral volume (Å^3)	
		MnO_6 in the mixed layer	LiO_6 and NaO_6 in the Li layer
$Li_{1-x}Na_xMn_{0.5}O_{1.5}$	0.0	9.4864	12.0218
	0.125	9.4818	12.5518
	0.25	9.4897	13.0774
	0.375	9.5193	13.5317
	0.5	9.4989	14.0064
	0.625	9.5075	14.4287
	0.75	9.4956	14.8630
	0.875	9.5743	15.0235
	1.0	9.6633	15.1530

Table 2.2 Elemental mapping data from inductively coupled plasma mass spectroscopy (ICP-MS) analysis.

Compound	Elements	Content (ppm)	Weight (g)	Wt (%)	Mol (%)	Fraction
	Li	17323.22	1.75	1.73	25.17	0.25
NLMO	Na	176553.3	17.81	17.66	77.46	0.76
	Mn	419761.4	42.34	41.98	77.07	0.75

Table 2.3 Calculated octahedral structure parameters (i.e., octahedral volume, bond lengths) of $O(Na_3Mn_2Li)$ and $O(Mn_2Li_4)$ based on Figure 2.13. $O(Na_3Mn_2Li)_{L1}$ and $O(Na_3Mn_2Li)_{L2}$ are from the octahedra in Figures 2.13a and b, and $O(Mn_2Li_4)_{L1}$ and $O(Mn_2Li_4)_{L2}$ refer to the octahedra in Figures 2.13c and d.

Compound	Octahedron	Structural parameters		Linear bond type (Li-O-Na or Li-O-Li)	
		Volume	Bond length	Li-O	O-Na or O-Li
$Na(Li_{1/3}Mn_{2/3})O_2$	$O(Na_3Mn_2Li)_{L1}$	12.1698	2.1063	2.0634	2.19959
	$O(Na_3Mn_2Li)_{L2}$	12.6987	2.1319	2.0751	2.2342
$Li(Li_{1/3}Mn_{2/3})O_2$	$O(Mn_2Li_4)_{L1}$	10.8919	2.0181	2.0662	2.0070
	$O(Mn_2Li_4)_{L2}$	11.1821	2.0357	2.0530	2.0340

서울대학교
SEOUL NATIONAL UNIVERSITY

Chapter 3

Multiscale Design and Realization of Na(Li$_{1/3}$Mn$_{1/2}$Cr$_{1/6}$)O$_2$

3.1 Theoretical Design of Na(Li$_{1/3}$Mn$_{1/2}$Cr$_{1/6}$)O$_2$

The rationally designed Na(Li$_{1/3}$Mn$_{2/3}$)O$_2$ exhibiting anionic redox reactions (O^{2-}/O^{-} originating from the Na–O–Li electronic configuration) is an excellent cathode material with high energy density ($\approx$4.2 V vs. Na/Na$^+$ with 190 mAh g^{-1}). However, Na$_{1-x}$(Li$_{1/3}$Mn$_{2/3}$)O$_2$ suffers from phase separation at x = 4/6 in the high-voltage region and a phase change from O3 to P2 in the low-voltage region (Figure 3.1a). This thermodynamic energy behavior indicates large structural changes in those two regions, originating from the anionic redox reactions in the absence of cationic redox activity (Mn^{4+}/Mn^{5+}) (Figure 3.1b–d). The pure oxygen-based redox reactions destabilize the crystal framework of Na(Li$_{1/3}$Mn$_{2/3}$)O$_2$ during desodiation. Considering the active cation species available for redox reactions, we rationally designed Na(Li$_{1/3}$Mn$_{2/3(1-y)}$M$_{cy}$)O$_2$ (M$_c$: 3d_1 (V: t_{2g}^1 e_g^0), 3d_2 (Cr: t_{2g}^2 e_g^0), and 3d_4 (Fe: t_{2g}^3 e_g^1) transition metals in the form M$_c^{4+}$), in which the phase change and separation issues are mitigated,

as the presence of M_c reduces the oxygen destabilization upon Na-extraction.

3.2 Electrochemical Enhancement

Figure 3.2a-c shows the desodiation potentials with the varying M_c content (y) as a function of the inverse Na content (x) for $Na_{1-x}(Li_{1/3}Mn_{2/3(1-y)}V_y)O_2$, $Na_{1-x}(Li_{1/3}Mn_{2/3(1-y)}Cr_y)O_2$, and $Na_{1-x}(Li_{1/3}Mn_{2/3(1-y)}Fe_y)O_2$, based on the mixing enthalpy values considering all possible Na/vacancy configurations (Figure 3.3-5). The voltage profiles are divided in three sections: low ($1 < V < {\sim}2.5$), middle ($\sim2.5 < V < \sim3.0$), and high ($V > 3.0$) voltages. The $Na_{1-x}(Li_{1/3}Mn_{2/3(1-y)}Cr_y)O_2$ species with varying x and y values present high-voltage behavior in comparison with all the other oxides. In particular, the low voltage for the initial desodiation of NLMO is remarkably improved for $Na_{1-x}(Li_{1/3}Mn_{2/3(1-y)}Cr_y)O_2$ compared to the other cases. All desodiation potentials in $Na_{1-x}(Li_{1/3}Mn_{2/3(1-y)}Cr_y)O_2$ according to the Cr content are expected to be found in the middle and high voltage regions; however, most of the desodiation potentials of $Na_{1-x}(Li_{1/3}Mn_{2/3(1-y)}Fe_y)O_2$ and $Na_{1-x}(Li_{1/3}Mn_{2/3(1-y)}V_y)O_2$ are found in the low and middle voltage ranges. Based on the calculated voltages for $Na_{1-x}(Li_{1/3}Mn_{2/3(1-y)}Cr_y)O_2$, the Cr content $y = {\approx}1/6$ was determined to be a suitable loading for NLMO advanced cathodes, and the formation energy predicts that a thermodynamically stable phase of $Na(Li_{1/3}Mn_{2/3(1-y)}Cr_{2/3y})O_2$ is at $y = 1/4$ (Figure 3.6).

3.3 Thermodynamic Enhancement

To compare the thermodynamic phase stability of $Na(Li_{1/3}Mn_{1/2}Cr_{1/6})O_2$ (NLMCO) with that of $Na(Li_{1/3}Mn_{1/2}V_{1/6})O_2$ (NLMVO), $Na(Li_{1/3}Mn_{1/2}Fe_{1/6})O_2$ (NLMFO), and NLMO, we examined in detail the mixing enthalpies considering all the possible Na/vacancy configurations. Figure 3.7a shows the atomic structures of NLMO, NLMCO, NLMFO, and NLMVO consisting of Na atoms in the 2c and 4h sites, Li in the 2b sites, and the transition metals in the 4g sites. The large difference in the mixing enthalpy (ΔH_1) generated by the phase change from O3 to P2 is ca. -0.317 eV for NLMO, while it is ca. -0.221 eV for NLMCO (ca. -0.335 eV for NLMVO and -0.275 eV for NLMFO) (Figure 3.7b– e). The reduced formation energy for NLMCO leads to a higher redox potential (~2.445 V $vs.$ Na/Na$^+$) in the low voltage region than that of the other oxides, reflecting smaller structure variations. In the high voltage region, all layered compounds were expected to undergo a phase separation between x = 4/6 and x = 1.0. Such phase separation is closely related to a phase-transition activation barrier (also called a spinodal decomposition barrier, S_b) critically affected by the intermediate phases between the two minima. The intermediate phase at x = 5/6 for NLMCO is expected to be more stable than the other phases of the three oxides. For clarity, the minimum mixing enthalpy values of all compounds calculated by the first-principles method were carefully fitted using a double-well function in the two-phase reaction region (see Figure 3.8 and Chapter 4). A much lower S_b value was obtained for NLMCO (~0.0169 eV) than for the other materials (NLMO: ~0.0714 eV, NLMFO: 0.0357 eV, and NLMVO: 0.0333 eV). Considering the theoretically well-developed model including the homogeneous entropy of configurational mixing with the absolute temperature, we calculated

44

the homogeneous bulk free energies ($\Delta G_{\text{hom}}^{\text{C}}$) for NLMO, NLMCO, NLMVO, and

NLMFO at 300 K (Figure 3.7f). The $\Delta G_{\text{hom}}^{\text{C}}$ of NLMCO indicates a slower phase

separation induced by a much lower S_b between $Na_{2/6}(Li_{1/3}Mn_{1/2}Cr_{1/6})O_2$ and

$(Li_{1/3}Mn_{1/2}Cr_{1/6})O_2$ than for NLMO and the other oxides. Such a slow phase

separation may result in the conservation of the high voltage with better cyclic

stability than that of NLMO. Figure 3.7g shows the homogeneous chemical

potentials at 300 K as a function of the inverse Na content in the four oxides,

suggesting a thermodynamic hysteresis gap between the charge and discharge

cycles in the high-voltage region. From the calculated chemical potentials, a

much smaller hysteresis gap (≈ 0.5 V) is expected for NLMCO than for NLMO,

leading to high energy density properties.

3.4 Multiscale Phase Field Simulation: Phase Separation

Based on the calculated homogeneous bulk free energies derived from the

thermodynamic mixing enthalpy values by first-principles calculations, we

performed the multiscale phase field simulations to compare the phase

separation kinetics for NLMO and NLMCO (see Chapter 4). Figure 3.9 presents

the phenomenological descriptions of the phase field simulation results

depending on various dimensionless time $\hat{t}$ with 40 × 40 computational cell

for NLMO and NLMCO. The characteristic lengths of the two oxides (NLMO:

0.2811nm; NLMCO: 0.2790 nm) were gained from the atomic structures of $Na_{1-x}(Li_{1/3}Mn_{2/3})O_2$ and $Na_{1-x}(Li_{1/3}Mn_{1/2}Cr_{1/6})O_2$ at $x = 5/6$; and the square-shaped

nanodomains were utilized with the side of 11.24 nm for NLMO and that of

11.16 nm for NLMCO. As the examined phase separation results in Section 2.6, the phase of NLMO was separated to $Na_{2/6}(Li_{1/3}Mn_{2/3})O_2$ and $Na_0(Li_{1/3}Mn_{2/3})O_2$ after the first charge process. The phase separation was predicted by the homogenous bulk free energy of NLMO. By contrast, the phase separation kinetic behavior of NLMCO was observed to be different from that of NLMO within the same dimensionless time. Even though the phase separation reaction occurred in NLMCO after the first charge process, the phase separation kinetics is much slower for NLMCO than for NLMO, because the slope of the homogeneous chemical potential of NLMO is much stiffer than that of NLMCO, related to the degree of phase separation. Taking into account the simulated phase separation kinetic behaviors of both oxides, better cyclic performance of NLMCO is predicted in comparison with NLMO.

3.5 Chemomechanical Strain Enhancement

From the structural perspective, the thermodynamic energy investigations on NLMCO, NLMO, NLMVO, and NLMFO can be explained by variations in the structural parameters during desodiation. Figure 3.10 presents the calculated structural parameters (unit cell volume and a, b, and c lattice parameters) as a function of the inverse Na content in NLMO, NLMCO, NLMVO, and NLMFO. For easy comparison, the structural constants of the thermodynamic ground states are shown in Figure 3.11. Smaller changes in the unit cell volume after the phase change are observed for NLMCO, NLMVO, and NLMFO than for NLMO, while the smallest variation during phase separation was obtained for NLMCO.

46

For better comparison, the structural parameters of all oxides were recalculated from the chemomechanical strain point of view (Figure 3.12a–d). On the basis of the volumetric and lattice strains, the results were fitted using a fourth order polynomial to obtain the continuous behavior of the strain considering nonlinearity. The c lattice strain was found to affect the behavior of the volumetric strain with respect to the inverse Na content.

3.6 Chemomechanical Stress Enhancement: Volumetric Stress

From the perspective of nanomechanics, we investigated the chemomechanical stress by carrying out in-depth structural analyses during desodiation (see Chapter 4). To evaluate the stress behavior, we calculated the bulk modulus using the Birch–Murnaghan equation of states as a function of the inverse Na content for NLMO and NLMCO (Figure 3.13). For nonlinearity, the obtained bulk moduli for the two oxides were fitted using a fourth order polynomial (Figure 3.12e). The bulk moduli of NLMCO are relatively higher than those of NLMO during desodiation, implying higher structure stability for NLMCO than for NLMO due to the reduced destabilization of the oxygen framework. Figure 3.12f presents the chemomechanical stress calculated from the volumetric strains and bulk moduli as a function of the inverse Na content in NLMO and NLMCO, indicating that the chemomechanical stress induced by the chemomechanical strain is much lower for NLMCO than for NLMO. In particular, tensile stress would be generated in NLMO upon the initial

47

desodiation; the compressive stress would then occur at a faster rate at the beginning of the phase separation region and into the fully desodiated phase region. Unlike NLMO, the tensile stress behavior in the initial desodiation region is not only almost suppressed in the case of NLMCO, but also the compressive stress in the phase separation region takes place at a much slower rate for NLMCO.

3.7 Multiscale Phase Field Simulation: Phase Separation Coupled Volumetric Stress

Unlike cathodes for LIBs, those for SIBs generally suffer from large volumetric strain during charge because of the intrinsically larger ionic radius of Na^+ than that of Li^+, as investigated in Figure 3.12; that is, strain energy would be critical for phase separation behaviors. Phase separation simulations considering volumetric strain energy were carried out for NLMO and NLMCO with 50×50 computational cell under the same characteristic lengths (see Figure 3.14 and Chapter 4). The simulated results indicate that there are much more inactive phases for NLMO with the strain energy than those for NLMO without the strain energy, which is attributed to the generation of large chemomechanical stress. As compared with NLMO results, there is no formation of fully desodiated phases for NLMCO from the phase separation simulation results because of the reduced chemomechanical stress. As a result, the distribution of the elastic stress of NLMO is more severe than that of NLMCO (Figure 3.15). The maximum compressive stress of NLMO is $\approx$-21.9 GPa, while that of NLMCO is $\approx$-18.5

48

GPa. These results predict that the stress generation of NLMO can be effectively mitigated by the Cr doping during charge/discharge.

3.8 Chemomechanical Stress Enhancement: Normal Stresses

For a more specific investigation on the volumetric stress behaviors, chemomechanical normal stresses of σ_{11}^n, σ_{22}^n, and σ_{33}^n, were calculated for NLMO and NLMCO. Figure 3.16a-c shows elastic constants of C_{11}, C_{22}, and C_{33} for NLMO and NLMCO as a function of inverse Na content. These elastic constants reveal similar behaviors as compared with the calculated bulk moduli, suggesting higher structure stability for NLMCO than for NLMO. Figure 3.16d-e presents the normal stresses of σ_{11}^n, σ_{22}^n, and σ_{33}^n for NLMO and NLMCO over the full range ($0.0 \leq x \leq 1.0$). In NLMCO material, the compressive stresses of σ_{11}^n and σ_{22}^n during the initial desodiation originate from Na-extraction accompanied by CrO_6 octahedron variations for oxidation reactions; and, the reduced tensile and compressive stresses of σ_{33}^n are observed. These results predict that the stress of σ_{33}^n largely contributes to the total chemomechanical stress by Na-extraction. For more exact understandings of chemomechanical stress behaviors, the 13 independent elastic constants in the elastic stiffness tensor (C_{ij}, where i,j = 1, 2, 3, 4 ,5 , and 6 with respect to the Voigt notation) for monoclinic structure were calculated using the internal energy change as a

49

function of strain (δ).[73] Figure 3.17a-j presents the remaining 10 independent elastic constants except the previously obtained components (C_{11}, C_{22}, and C_{33}) as a function of inverse Na content for NLMO and NLMCO. Based on Hooke's law ($\sigma_i = C_{ij}\varepsilon_j$), all chemomechanical stress components were obtained as shown in Figure 3.18a-f, which were fitted using a fourth order polynomial for the comparisons of stress behaviors at vacancy concentration (x) in $Na_{1-x}(Li_{1/3}Mn_{2/3})O_2$ and $Na_{1-x}(Li_{1/3}Mn_{1/2}Cr_{1/6})O_2$ over the full range ($0.0 \leq x \leq 1.0$). The two shear stresses (τ_{23} and τ_{13}) associated with the normal stress of σ_{33}^n were mitigated for NLMCO compared with those for NLMO. Furthermore, considering the two-phase regions of $Na_{1-x}(Li_{1/3}Mn_{2/3})O_2$ and $Na_{1-x}(Li_{1/3}Mn_{1/2}Cr_{1/6})O_2$ ($4/6 \leq x \leq 1.0$), the mismatch strain depending on the lattices and area of NLMCO is remarkably smaller than for NLMO (Table 3.1), which may result in a reduced coherent strain energy for NLMCO.

3.9 Multiscale Phase Field Simulation: Phase Separation Coupled Normal Stresses

In the viewpoint of phase behavior at meso-scale, phase separation behaviors depending on directions of normal stresses are expected to be different for NLMO and NLMCO. Figure 3.19a and b show the phenomenological descriptions of the phase filed simulation results considering the elastic strain energies generated by the normal stresses of σ_{11}^n, σ_{22}^n, and σ_{33}^n for NLMO and NLMCO, respectively. The phase field simulations were carried out under the

same computational conditions in Section 3.7. The phase separation behaviors considering the strain energies of σ_{11}^n and σ_{22}^n for NLMO and NLMCO reveal similar tendencies as compared with the phase field simulation results without elastic strain energies in Section 3.4. These simulated results indicate that the strain energies of σ_{11}^n and σ_{22}^n are not critical for the generation of inactive phase for NLMO and the formation of fully desodiated phase for NLMCO. By contrast, similar behaviors of the phase transformations induced by thermodynamic and volumetric strain energies for the both oxides were found in the phase field simulations with the strain energy of σ_{33}^n, suggesting that the generation of chemomechanical stress by σ_{33}^n totally contribute to the phase separation behaviors in Figure 3.14.

3.10 Atomic Structure Enhancement

Taking into account the phase separation for NLMO and NLMCO in the high-voltage region, we investigated the O−O distances (d_O) and their atomic configurations at x = 4/6 and 1.0 in $Na_{1-x}(Li_{1/3}Mn_{2/3})O_2$ and $Na_{1-x}(Li_{1/3}Mn_{1/2}Cr_{1/6})O_2$ (Figure 3.20a and b). Distances in the range ~2.45 Å < d_O < 2.55 Å were obtained for the mixed layer of $Na_{2/6}(Li_{1/3}Mn_{2/3})O_2$, whereas shorter O−O distances (longest O−O: ~2.53 Å and shortest O−O: 2.35 Å) were obtained between the $Li_{1/3}Mn_{2/3}O_2$ layers in $Na_0(Li_{1/3}Mn_{2/3})O_2$. The reduced interlayer d-spacing owing to shorter O−O distances may lead to $Na_0(Li_{1/3}Mn_{2/3})O_2$, which is an inactive phase, in the two-phase region. Likewise, O−O distances of 2.35−

2.50 Å were obtained for the mixed layer of $Na_{2/6}(Li_{1/3}Mn_{1/2}Cr_{1/6})O_2$, while no O–O long and short distances were observed for $Na_0(Li_{1/3}Mn_{1/2}Cr_{1/6})O_2$, even though the O–O distances in the mixed layer were slightly reduced. The highly oxidized O framework in $Na_0(Li_{1/3}Mn_{2/3})O_2$ may lead to reduced interlayer distances accompanied by short O–O bond formation to achieve thermodynamic stability, which results in a larger structural formation energy for NLMO than for NLMCO (Table 3.2). However, the O–O species in NLMO are not expected to promote sodiation and desodiation reactions, resulting in large structural changes. These changes in the atomic structures can be understood directly by a much stiffer elastic constant (C_{33}) for the fully desodiated NLMO than for NLMCO (Table 3.3).

3.11 Cation-Anion-Coupled Redox Mechanism

In order to investigate the origin of the redox mechanism in NLMCO during desodiation, the electronic structure of NLMCO was examined in detail. Based on the crystal field theory (CFT), the partial density of states (PDOS) in the fully sodiated ($x = 0.0$) $Na_{1-x}(Li_{1/3}Mn_{1/2}Cr_{1/6})O_2$ afforded a charge value of Cr^{4+} (half-filled $t_{2g}^2\ e_g^0$) and the Mn atoms in the compound show the typical electronic configuration of Mn^{4+} (half-filled $t_{2g}^3\ e_g^0$) (Figure 3.21a). Considering that further oxidation of Mn^{4+} to Mn^{5+} in an octahedral site is difficult, the 3d-electrons of Cr in the valence band are oxidized into the conduction band for charge compensation during the initial desodiation (see Figure 3.22). Subsequently, the O atoms coordinated to Mn^{4+} are expected to be oxidized to

compensate the charge imbalance induced by the Na-extraction after the cationic redox reaction of Cr. Figure 3.21a–g describes the variations on the PDOS of Mn and the Cr $3d$ and O $2p$ electrons as a function of the inverse Na content in $Na_{1-x}(Li_{1/3}Mn_{1/2}Cr_{1/6})O_2$. All Mn PDOS indicate a fixed Mn^{4+} $3d$-electron configuration from $x = 0.0$ to $x = 1.0$ in $Na_{1-x}(Li_{1/3}Mn_{1/2}Cr_{1/6})O_2$, while the Cr PDOS up to $x = \sim 2/6$ exhibits oxidizing behavior. Interestingly, the PDOS at values above $x = 2/6$ shows that the O $2p$ electrons participate on the oxidation reaction mainly through the fully oxidized $3d$ electrons of Mn and Cr. To quantitatively analyze the redox mechanism, we calculated the net charges of Mn, Cr, and O as a function of the inverse Na content (x) in $Na_{1-x}(Li_{1/3}Mn_{1/2}Cr_{1/6})O_2$ (Figure 3.21h–j). The net charges of Mn do not change with respect to the inverse Na content, whereas those of Cr vary linearly up to $x = \sim 2/6$. A linear increase of the O net charges was observed during the desodiation process. These quantitative analyses are consistent with the calculated PDOS of Mn, Cr, and O during Na-extraction. The redox mechanism was also elucidated through the octahedral structure variations with respect to the Na content (Table 3.4). To gain further information on the redox mechanism, we calculated the spatial electron distribution (SED) from -2 to 0 eV in $Na(Li_{1/3}Mn_{1/2}Cr_{1/6})O_2$ and $Na_{4/6}(Li_{1/3}Mn_{1/2}Cr_{1/6})O_2$. Figure 3.21k shows that the Cr 3d-electron density is hybridized with the O 2p-electron density, playing a role in the charge compensation upon initial Na-extraction. After the cationic redox reaction involving Cr, only the electron density corresponding to the O lone-pair is observed in $Na_{4/6}(Li_{1/3}Mn_{1/2}Cr_{1/6})O_2$ (Figure 3.21l). Such a pure O electron density indicates the linearity of the Na−O−Li structure at various atomic positions (Na−O−Li_1−4). These results suggest that the calculated low and high

voltages of NLMCO are predominantly responsible for the cationic redox reactions of the Cr $3d$ electrons hybridized with O $2p$ electrons and the anionic redox reactions originating from the Na–O–Li electronic configuration.

3.12 Developing the Material Analogues

Based on the advantages of cation (cyclic-stability) and anion (high-voltage) redox reactions considering the detailed analysis of the thermodynamic energy landscape of NLMO, we rationally designed cation-anion-coupled NLMCO. The combined redox paradigm was utilized to resolve the two existing requirements for high energy density cathode materials for SIB applications: i) increasing the low voltage and ii) maintaining the high voltage in NLMO during desodiation. Based on the desodiation potentials calculated by the first-principles method, NLMCO was found to exhibit a higher low voltage ($\approx$2.8 V versus Na/Na$^+$ in $0 \leq x \leq 2/6$) and similar high-voltage behavior ($\approx$4.2 V versus Na/Na$^+$ in $2/6 \leq x \leq 1.0$) than NLMO, NLMVO, and NLMFO. From the thermodynamics viewpoint, the reduced formation energy (ΔH_1 ca. -0.221 eV) for NLMCO results in higher redox potentials in the low-voltage region. The homogeneous bulk free energy of NLMCO at $4/6 \leq x \leq 1.0$ indicated a much lower S_b value and a slower phase separation in NLMO with a smaller gap of thermodynamic hysteresis than for the other oxides. Moreover, the chemomechanical strain and stress for NLMCO in the phase change (reduced tensile stress) and separation (reduced compressive stress) regions were distinctively smaller than in the other cases. The formation of short O–O bonds in NLMO lead to the electrochemically inactive phase $Na_0(Li_{1/3}Mn_{1/2}Cr_{1/6})O_2$, whereas O–O formation between the mixed layers was

not observed in NLMCO. Regarding the redox mechanism, the cationic redox reactions involving the Cr $3d$ electrons reduce the destabilization of the oxygen framework induced by the anionic redox reaction of the O lone-pair during desodiation. We believe that such an anionic redox reaction (O^{2-}/O^{-}) coupled with a cationic redox reaction ($M^{n+}/M^{(n+1)+}$) is an enhanced paradigm of the anionic redox reaction for the realization of high energy density cathode materials for SIBs. In this sense, from the electrochemical, thermodynamic, atomic, chemomechanical, and redox mechanism points of view, the rationally designed cation-anion-coupled NLMCO is a promising material for SIBs, enabling the development of a new class of $Na(Li_{1/3}M_{2/3(1-y)}M_{cy})O_2$ materials (M and M_c: transition metals with stabilized M^{4+} species and cationic redox active M_c^{4+} species), leading to the design of next-generation cathodes for future electrochemical storage materials.
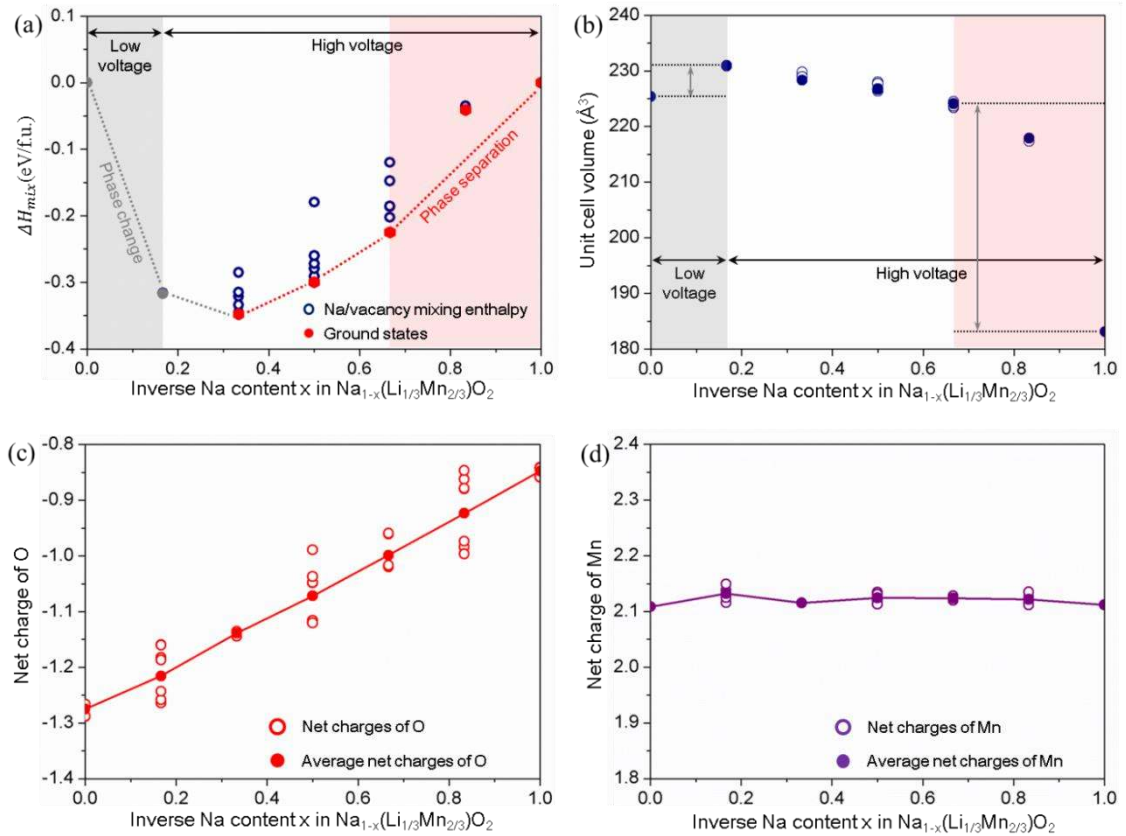
Figure 3.1 (a) Mixing enthalpy values considering all possible Na/vacancy configurations for $0 \leq x \leq 1.0$ in $Na_{1-x}(Li_{1/3}Mn_{2/3})O_2$. (b) Calculated unit cell volume and net charges for (c) O and (d) Mn as a function of the inverse Na content (x) in $Na_{1-x}(Li_{1/3}Mn_{2/3})O_2$. The mixing enthalpies and net charges are reproduced from a previous report by us.[1]
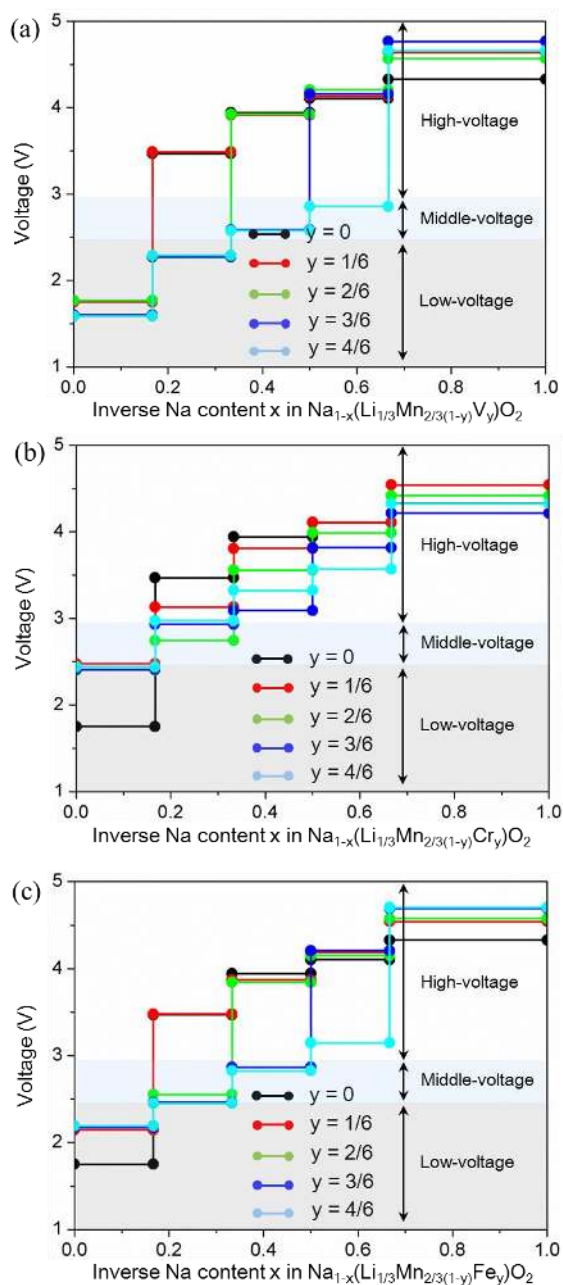
Figure 3.2 Calculated desodiation potentials as a function of the inverse Na content (x) in $Na_{1-x}(Li_{1/3}Mn_{2/3(1-y)}M_y)O_2$ (M: (a) V, (b) Cr, and (c) Fe) at varying y values. The voltage range is divided in three sections: low (1 < V < 2.5), middle (2.5 < V < 3.0), and high (3.0 < V < 5.0) voltage ranges.
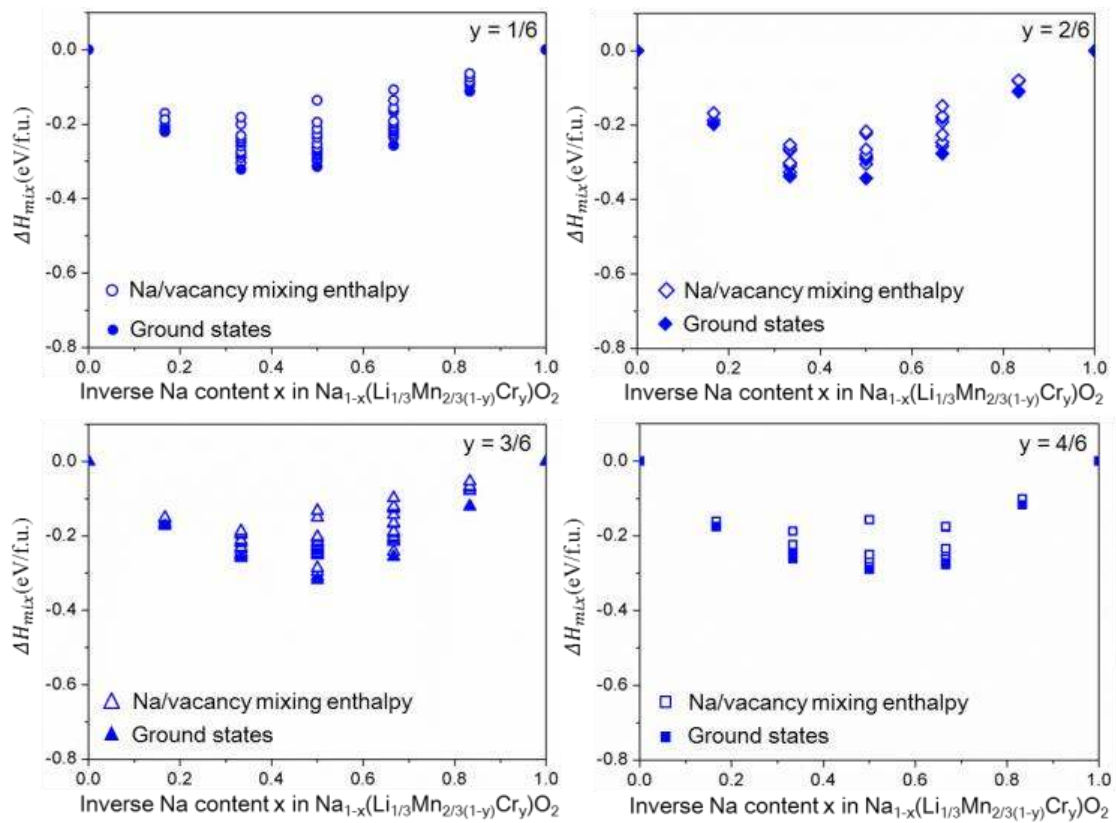
Figure 3.3 Mixing enthalpy values considering all possible Na/vacancy configurations as a function of the inverse Na content (*x*) in $Na_{1-x}(Li_{1/3}Mn_{2/3(1-y)}Cr_y)O_2$ at varying *y* values (*y* = 1/6, 2/6, 3/6, and 4/6).
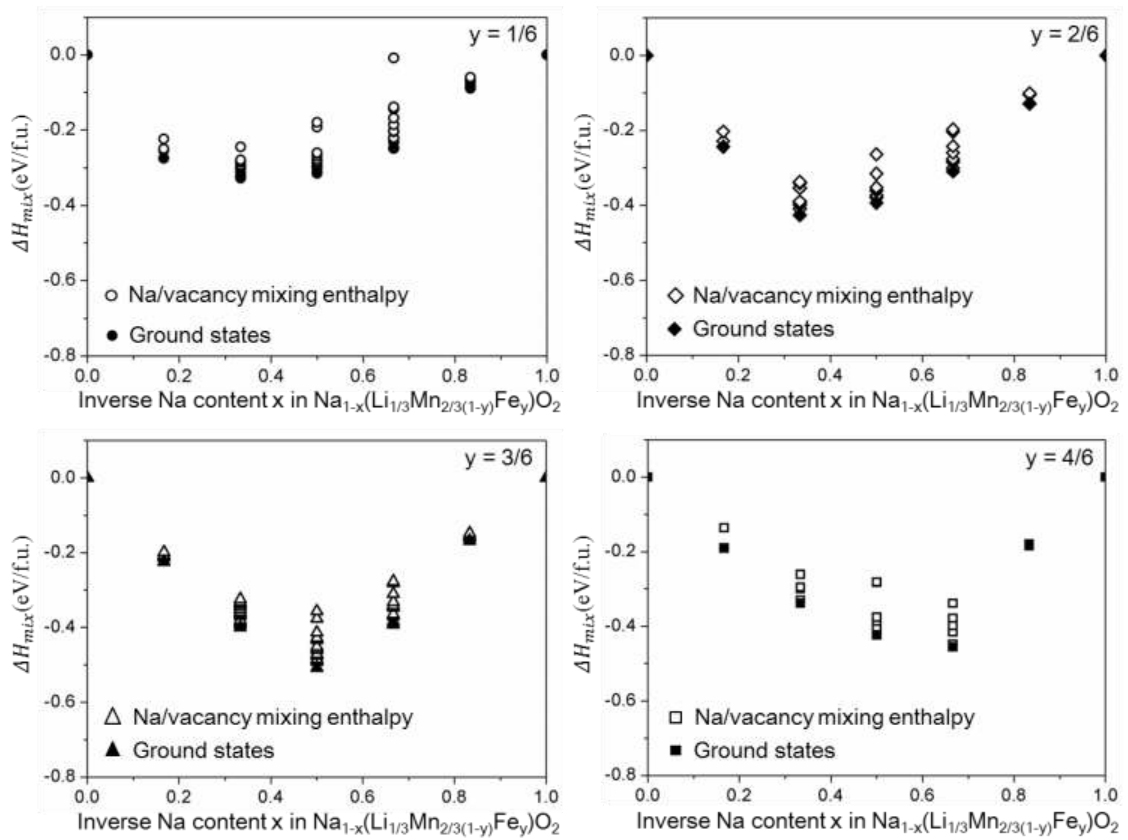
Figure 3.4 Mixing enthalpy values considering all possible Na/vacancy configurations as a function of the inverse Na content (x) in $Na_{1-x}(Li_{1/3}Mn_{2/3(1-y)}Fe_y)O_2$ at varying y values (y = 1/6, 2/6, 3/6, and 4/6).
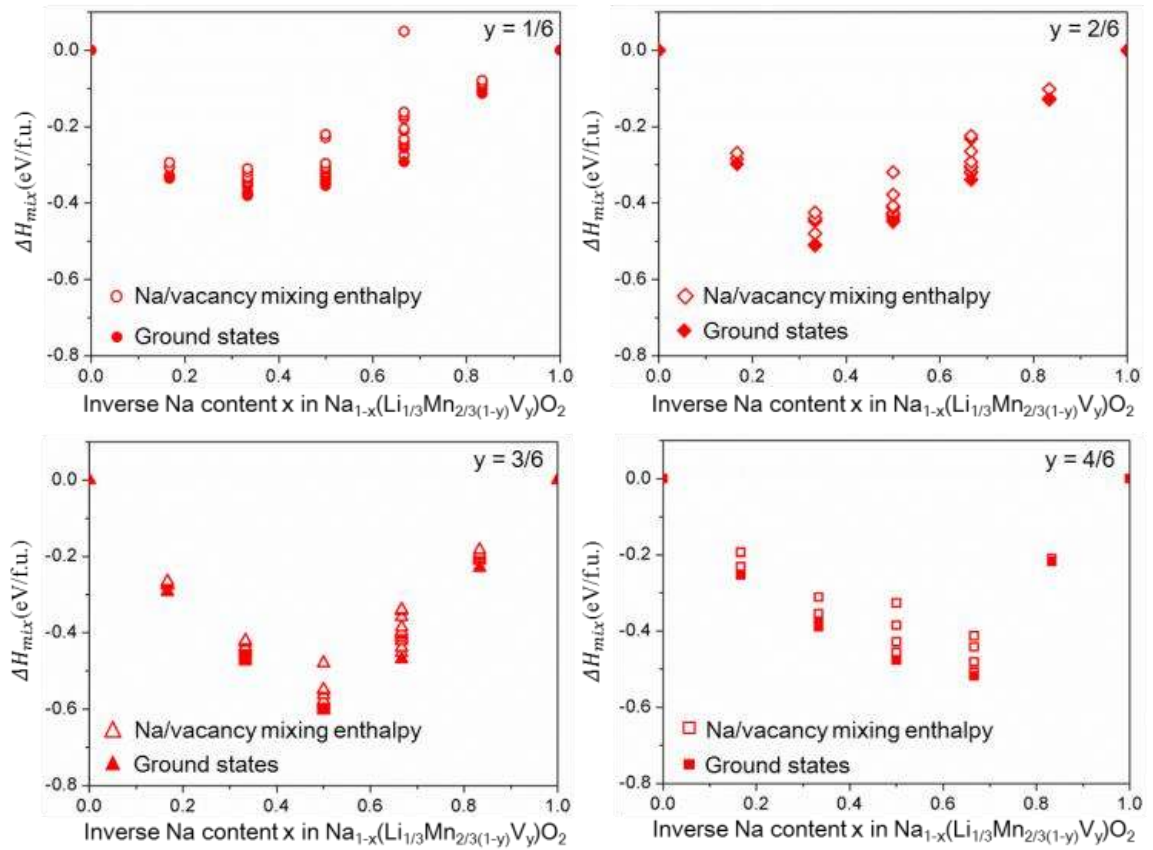
Figure 3.5 Mixing enthalpy values considering all possible Na/vacancy configurations as a function of the inverse Na content (x) in $Na_{1-x}(Li_{1/3}Mn_{2/3(1-y)}V_y)O_2$ at varying y values (y = 1/6, 2/6, 3/6, and 4/6).
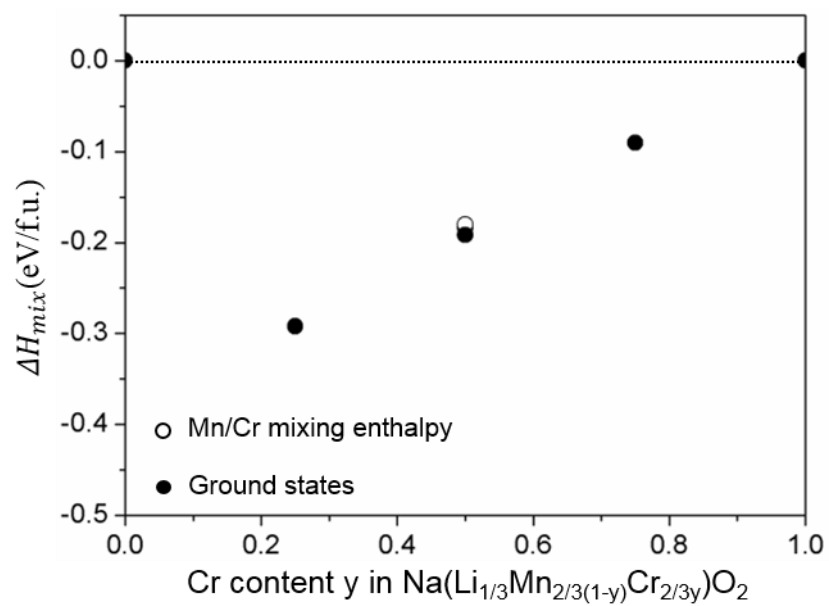
Figure 3.6 Mixing enthalpy values considering all possible Mn/Cr configurations as a function of the Cr content (y) in $Na(Li_{1/3}Mn_{2/3(1-y)}Cr_{2/3y})O_2$.
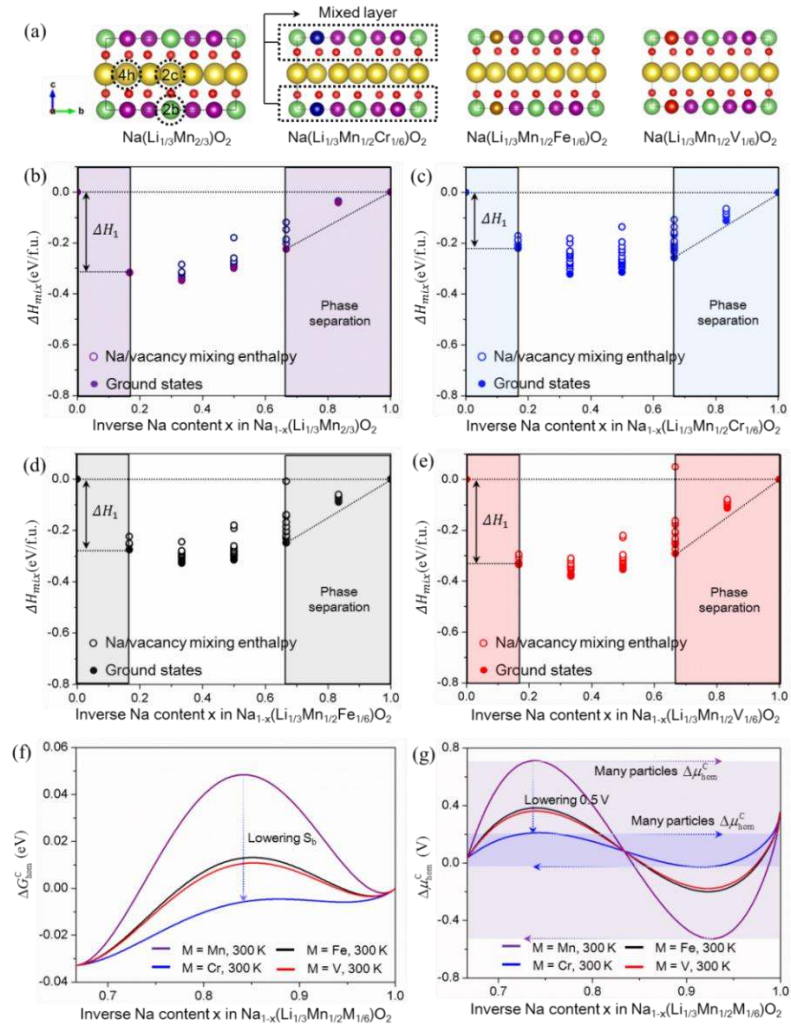
Figure 3.7 (a) Atomic structures of Na(Li$_{1/3}$Mn$_{2/3}$)O$_2$, Na(Li$_{1/3}$Mn$_{1/2}$Cr$_{1/6}$)O$_2$, Na(Li$_{1/3}$Mn$_{1/2}$Fe$_{1/6}$)O$_2$, and Na(Li$_{1/3}$Mn$_{1/2}$V$_{1/6}$)O$_2$. Mixing enthalpy values considering all possible Na/vacancy configurations as a function of the inverse Na content (x) for (b) Na$_{1-x}$(Li$_{1/3}$Mn$_{2/3}$)O$_2$, (c) Na$_{1-x}$(Li$_{1/3}$Mn$_{1/2}$Cr$_{1/6}$)O$_2$, (d) Na$_{1-x}$(Li$_{1/3}$Mn$_{1/2}$Fe$_{1/6}$)O$_2$, and (e) Na$_{1-x}$(Li$_{1/3}$Mn$_{1/2}$V$_{1/6}$)O$_2$. (f) Configurational homogeneous bulk free energies and (g) chemical potentials at 300 K of Na$_{1-x}$(Li$_{1/3}$Mn$_{1/2}$ M$_{1/6}$)O$_2$ (~4/6 ≤ x ≤ 1.0) (M: Mn, Cr, Fe, and V).

62
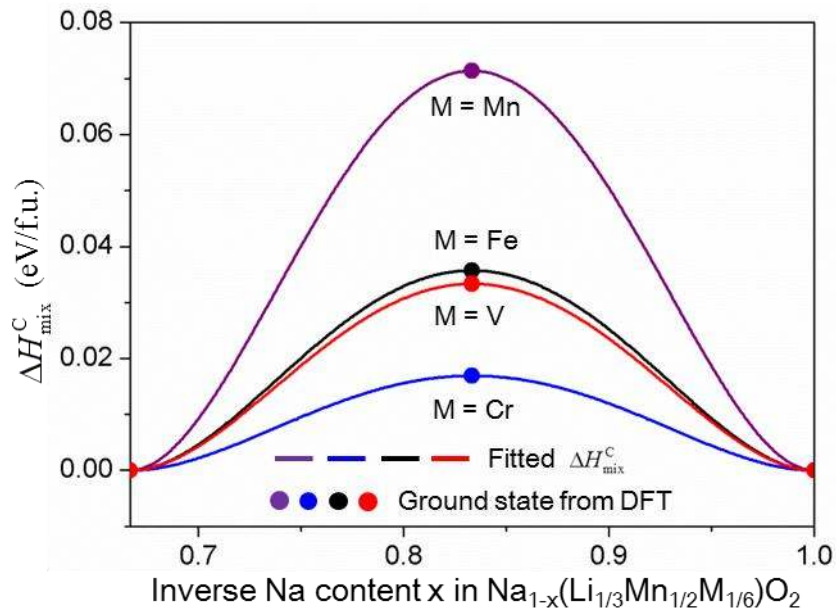
Figure 3.8 Configurational homogeneous mixing enthalpies fitted from the mixing enthalpies at x = 4/6, 5/6, and 1.0 in $Na_{1-x}(Li_{1/3}Mn_{1/2}M_{1/6})O_2$ (M: Mn, Cr, Fe, and V) from Figure 3.7b–e using a double-well function.
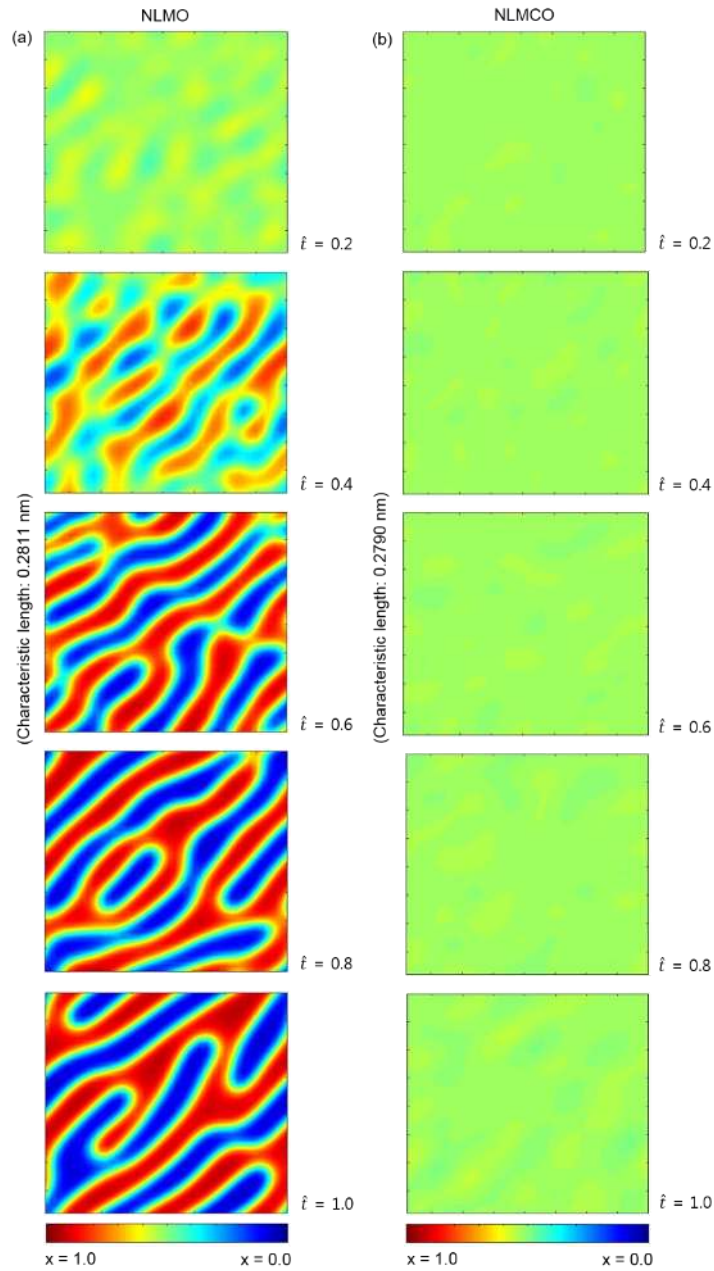
Figure 3.9 Phase separation kinetic simulation results in (a) $Na_{1-x}(Li_{1/3}Mn_{2/3})O_2$ and (b) $Na_{1-x}(Li_{1/3}Mn_{1/2}Cr_{1/6})O_2$ at $x = 5/6$ during relaxation from a solid solution at various dimensionless time. The color bar indicates the normalized inverse Na content between x = 4/6 and x = 1.0.
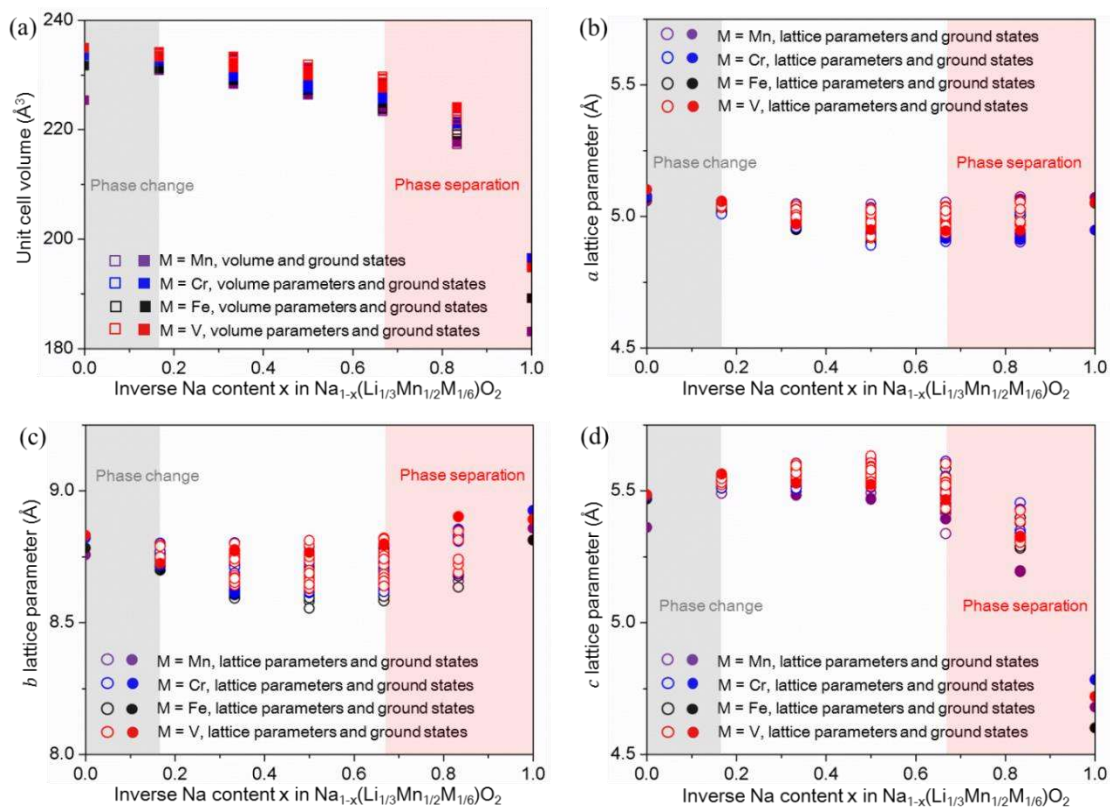
Figure 3.10 Calculated structural parameters (unit cell volume, and a, b, and c lattice parameters) as a function of the inverse Na content (x) in $Na_{1-x}(Li_{1/3}Mn_{1/2}M_{1/6})O_2$ (M: Mn, Cr, Fe, and V).
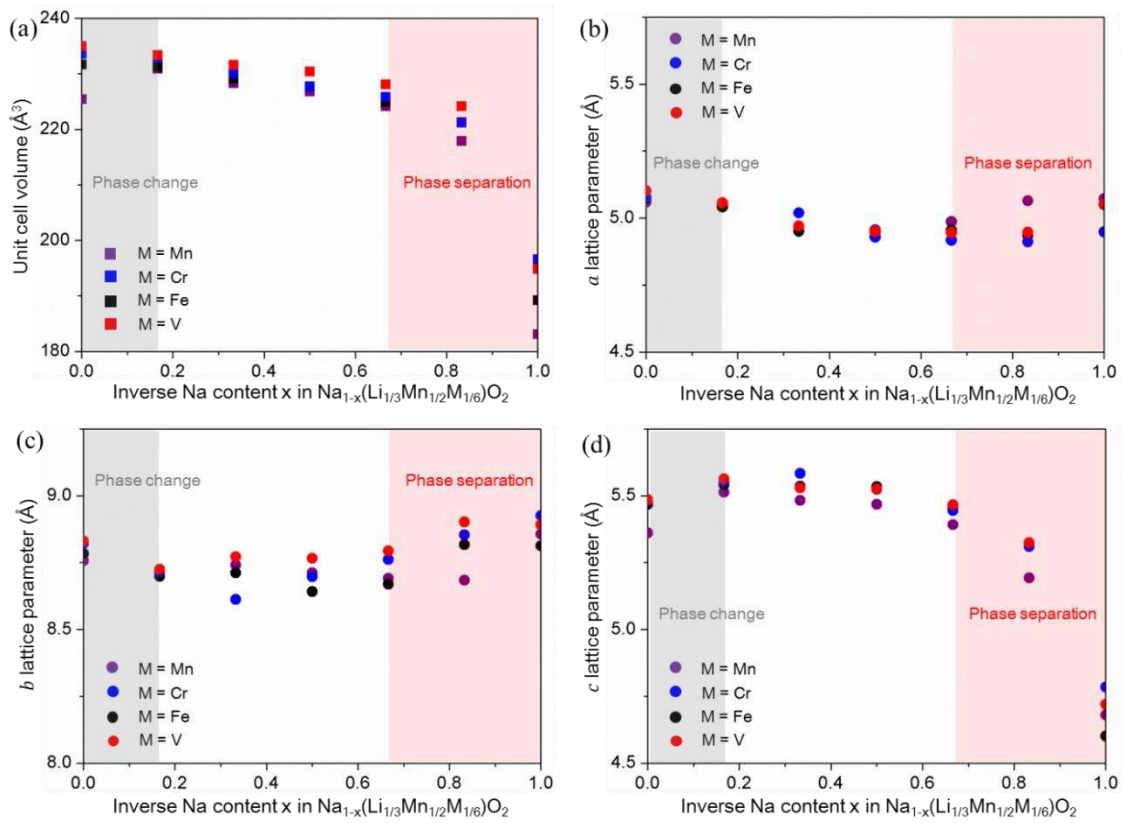
Figure 3.11 Structural parameters for the ground states from Figure 3.10 as a function of the inverse Na content (x) in $Na_{1-x}(Li_{1/3} Mn_{1/2}M_{1/6})O_2$ (M: Mn, Cr, Fe, and V).
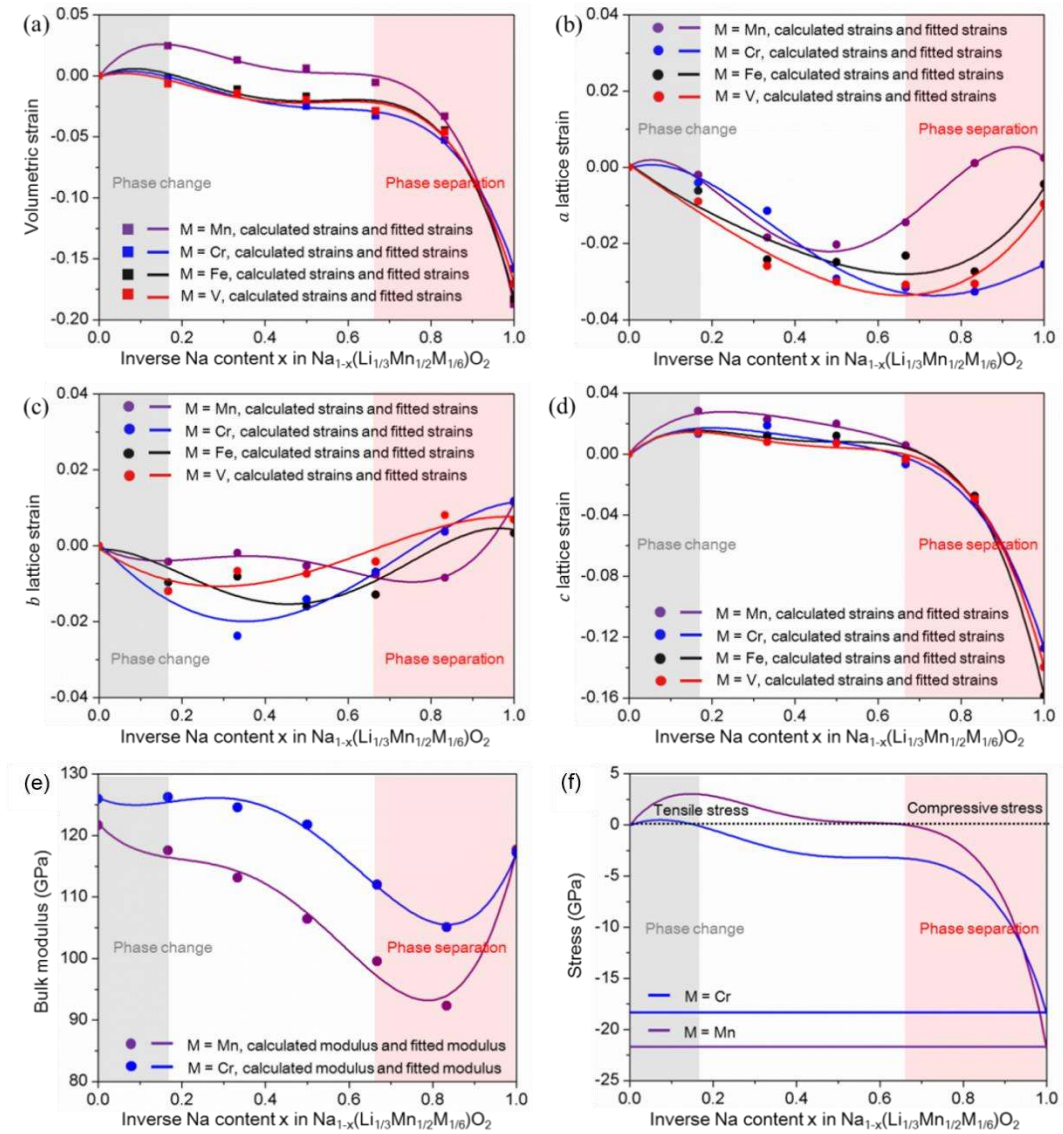
Figure 3.12 (a) Calculated volumetric strain, (b) *a*, (c) *b*, and (d) *c* lattice strains as a function of the inverse Na content (*x*) in $Na_{1-x}(Li_{1/3}Mn_{1/2}M_{1/6})O_2$ (M: Mn, Cr, Fe, and V). All chemomechanical strains were fitted using a fourth order polynomial. (e) Bulk moduli calculated by first-principles and fitted bulk moduli using a fourth order polynomial. (f) Chemomechanical volumetric stress in $Na_{1-x}(Li_{1/3}Mn_{2/3})O_2$ and $Na_{1-x}(Li_{1/3}Mn_{1/2}Cr_{1/6})O_2$ ($0 \leq x \leq 1.0$).
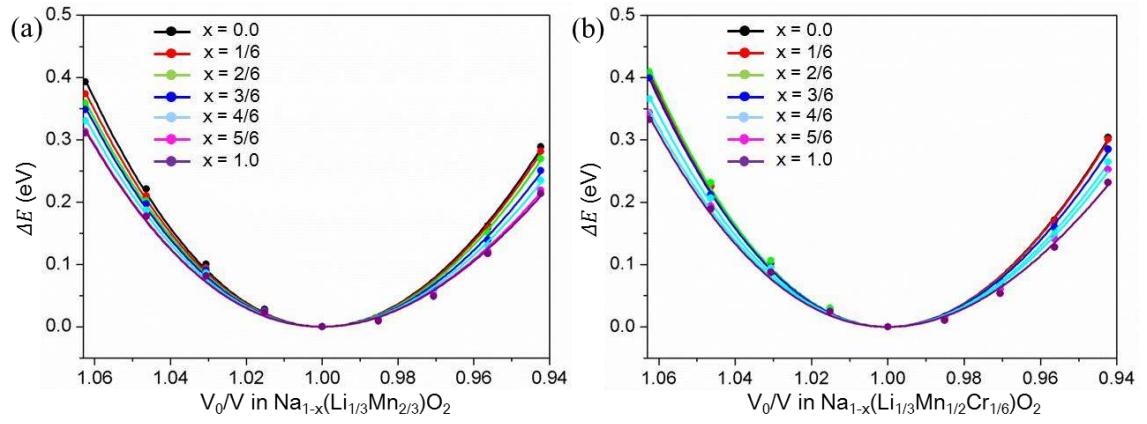
Figure 3.13 Changes in the strain energy (ΔE) as a function of the volume ratio (V_0/V) in $Na_{1-x}(Li_{1/3}Mn_{2/3})O_2$ and $Na_{1-x}(Li_{1/3}Mn_{1/2}Cr_{1/6})O_2$. The solid lines represent the fitted results using the Birch–Murnaghan equation of states, based on the total energies calculated by the first-principles method.
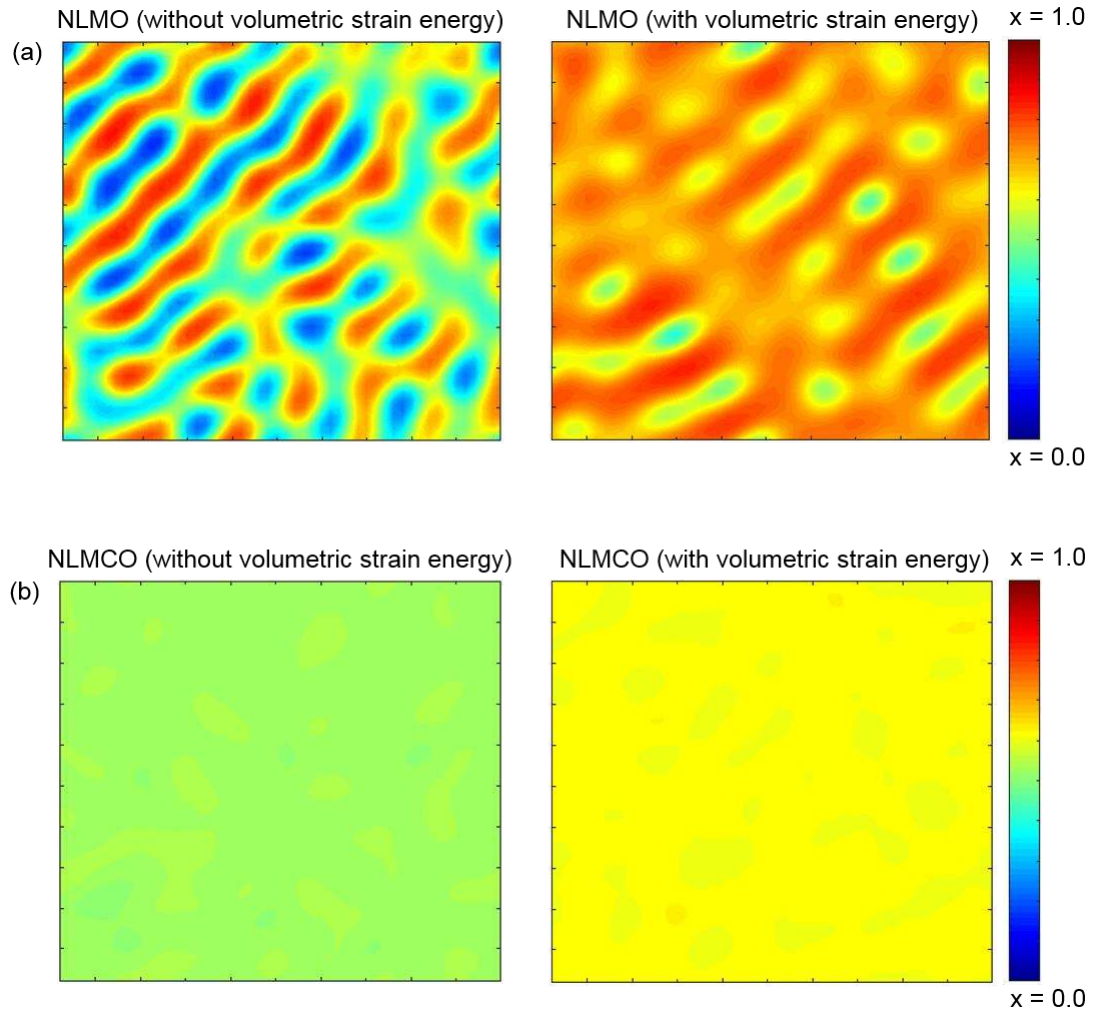
Figure 3.14 Phase separation kinetic simulation results without or with the chemomechanical volumetric strain energy derived from Figure 3.12 in (a) $Na_{1-x}(Li_{1/3}Mn_{2/3})O_2$ and (b) $Na_{1-x}(Li_{1/3}Mn_{1/2}Cr_{1/6})O_2$ at $x = 5/6$ during relaxation from a solid solution at the fixed dimensionless time. The color bar indicates the normalized inverse Na content between x = 4/6 and x = 1.0.
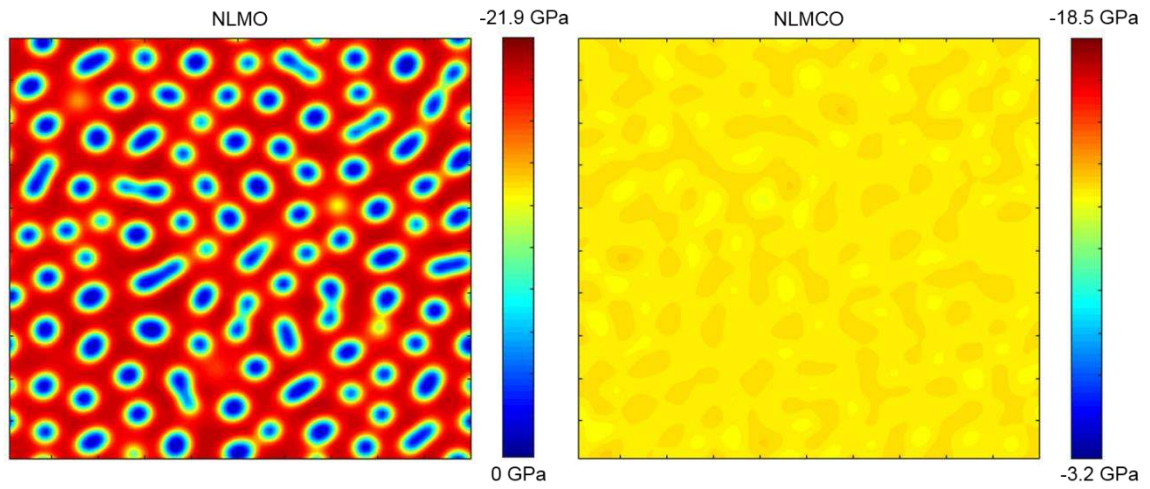
Figure 3.15 Distribution of elastic stress with 100 × 100 computational cell under the same characteristic lengths induced by the phase transformation from a solid solution of x = 5/6 in $Na_{1-x}(Li_{1/3}Mn_{2/3})O_2$ and $Na_{1-x}(Li_{1/3}Mn_{1/2}Cr_{1/6})O_2$ at the dimensionless time of $\hat{t} = 1.0$.
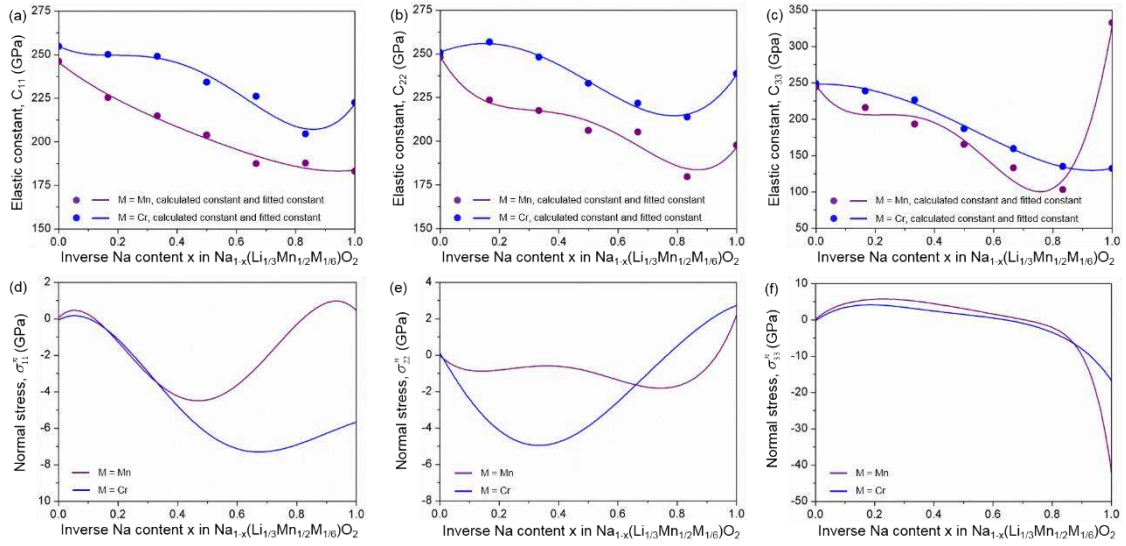
Figure 3.16 Elastic constants, (a) C_{11}, (b) C_{22}, and (c) C_{33}, calculated by first-principles method and fitted elastic constants using a fourth order polynomial; and chemomechanical normal stresses, (d) σ_{11}^n, (e) σ_{22}^n, and (f) σ_{33}^n in $Na_{1-x}(Li_{1/3}Mn_{2/3})O_2$ and $Na_{1-x}(Li_{1/3}Mn_{1/2}Cr_{1/6})O_2$ ($0 \leq x \leq 1.0$).
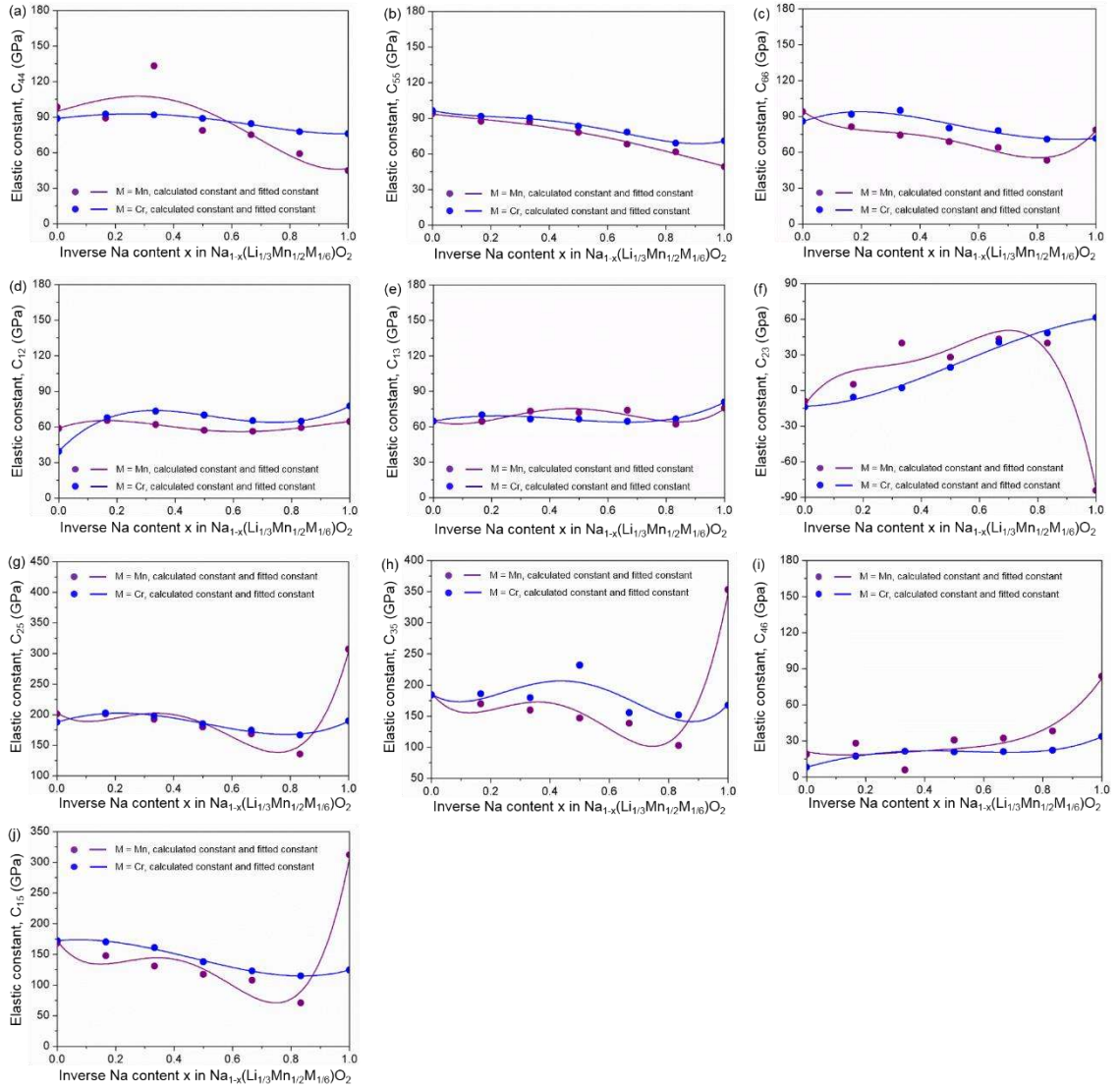
Figure 3.17 Elastic constants, (a) C_{44}, (b) C_{55}, (c) C_{33}, (d) C_{12}, (e) C_{13}, (f) C_{23}, (g) C_{25}, (h) C_{35}, (i) C_{46}, and (j) C_{15}, calculated by first-principles method with varying x in $Na_{1-x}(Li_{1/3}Mn_{2/3})O_2$ and $Na_{1-x}(Li_{1/3}Mn_{1/2}Cr_{1/6})O_2$ and fitted elastic constants using a fourth order polynomial.
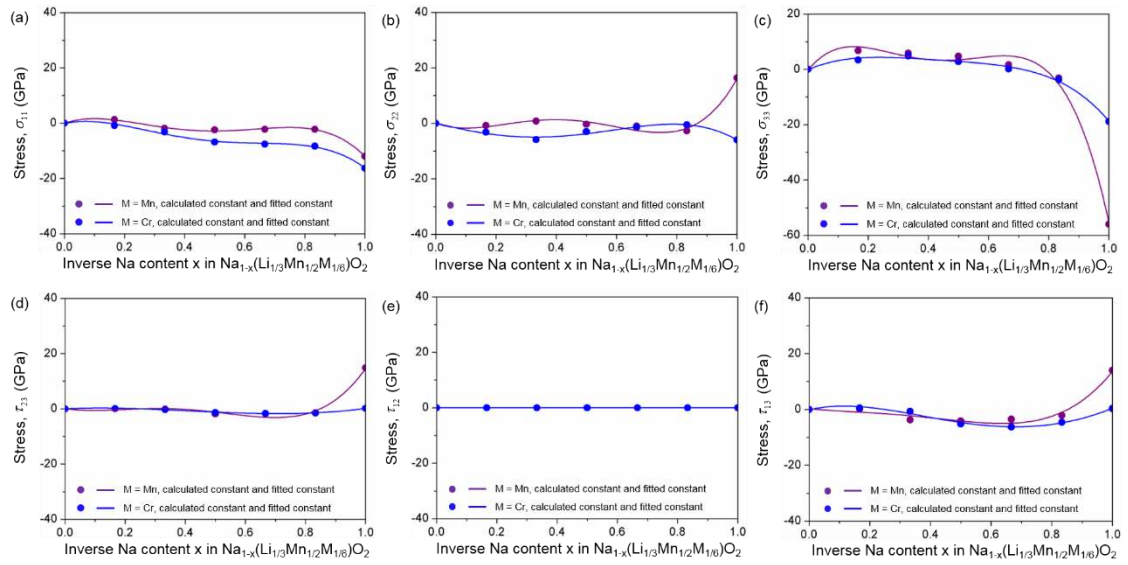
Figure 3.18 Chemomechanical stresses, (a) σ_{11}, (b) σ_{22}, (c) σ_{33}, (d) τ_{23}, (e) τ_{12}, and (f) τ_{13} in $Na_{1-x}(Li_{1/3}Mn_{2/3})O_2$ and $Na_{1-x}(Li_{1/3}Mn_{1/2}Cr_{1/6})O_2$ ($0 \leq x \leq 1.0$).
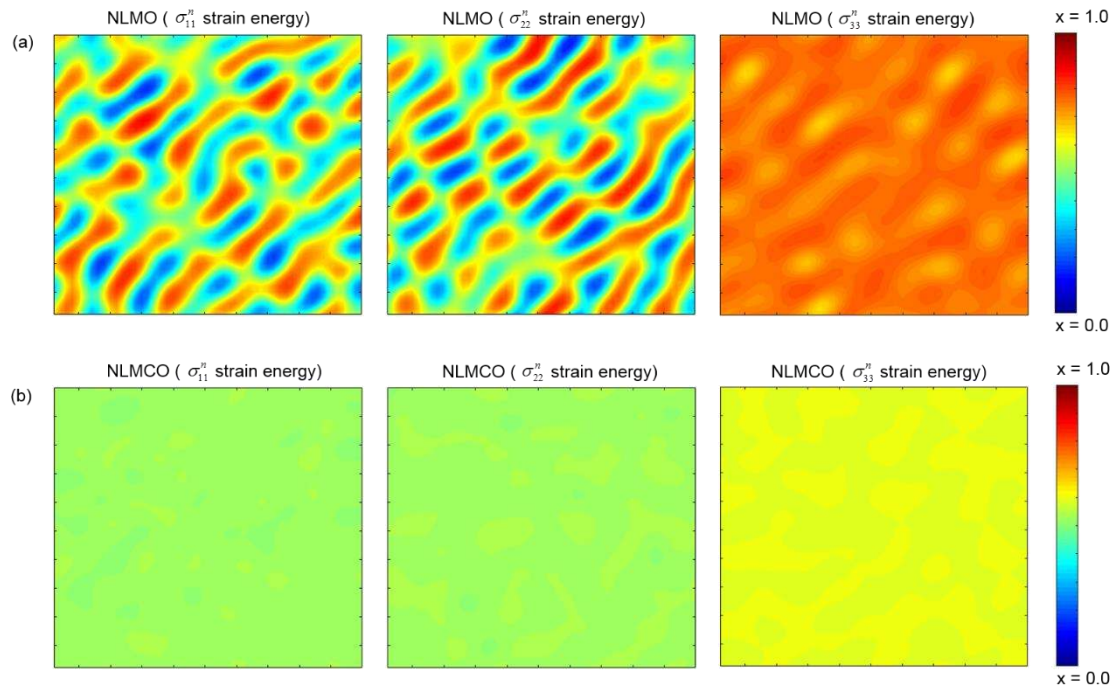
Figure 3.19 Phase separation kinetic simulation results considering the chemomechanical normal strain energies induced by σ_{11}^{n}, σ_{22}^{n}, and σ_{33}^{n} for (a) NLMO and (b) NLMCO. The color bar indicates the normalized inverse Na content between x = 4/6 and x = 1.0.
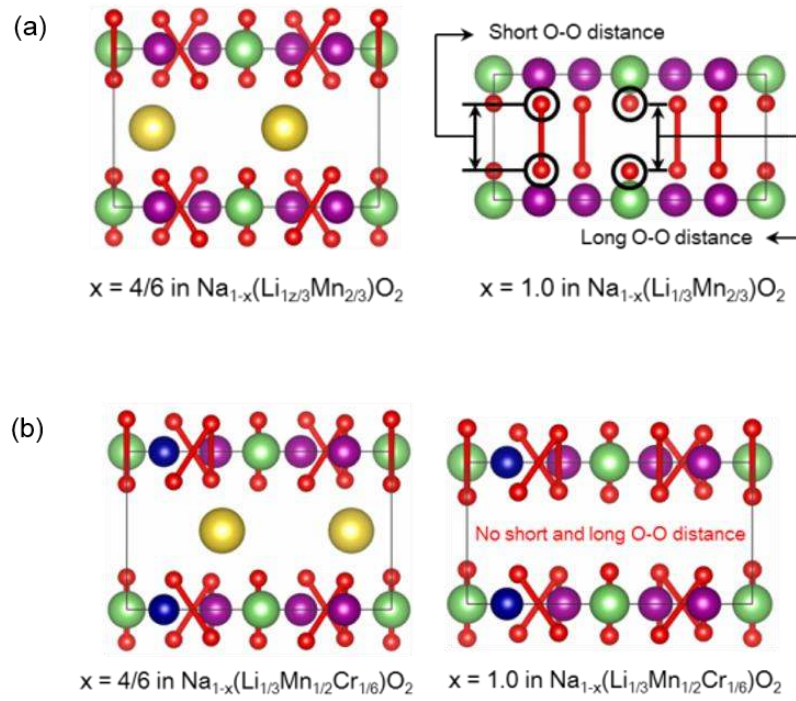
Figure 3.20 Atomic structures of $Na_{1-x}(Li_{1/3}Mn_{2/3})O_2$ at (a) $x = 4/6$ and $x = 1.0$, and those of $Na_{1-x}(Li_{1/3}Mn_{1/2}Cr_{1/6})O_2$ at (b) $x = 4/6$ and $x = 1.0$.
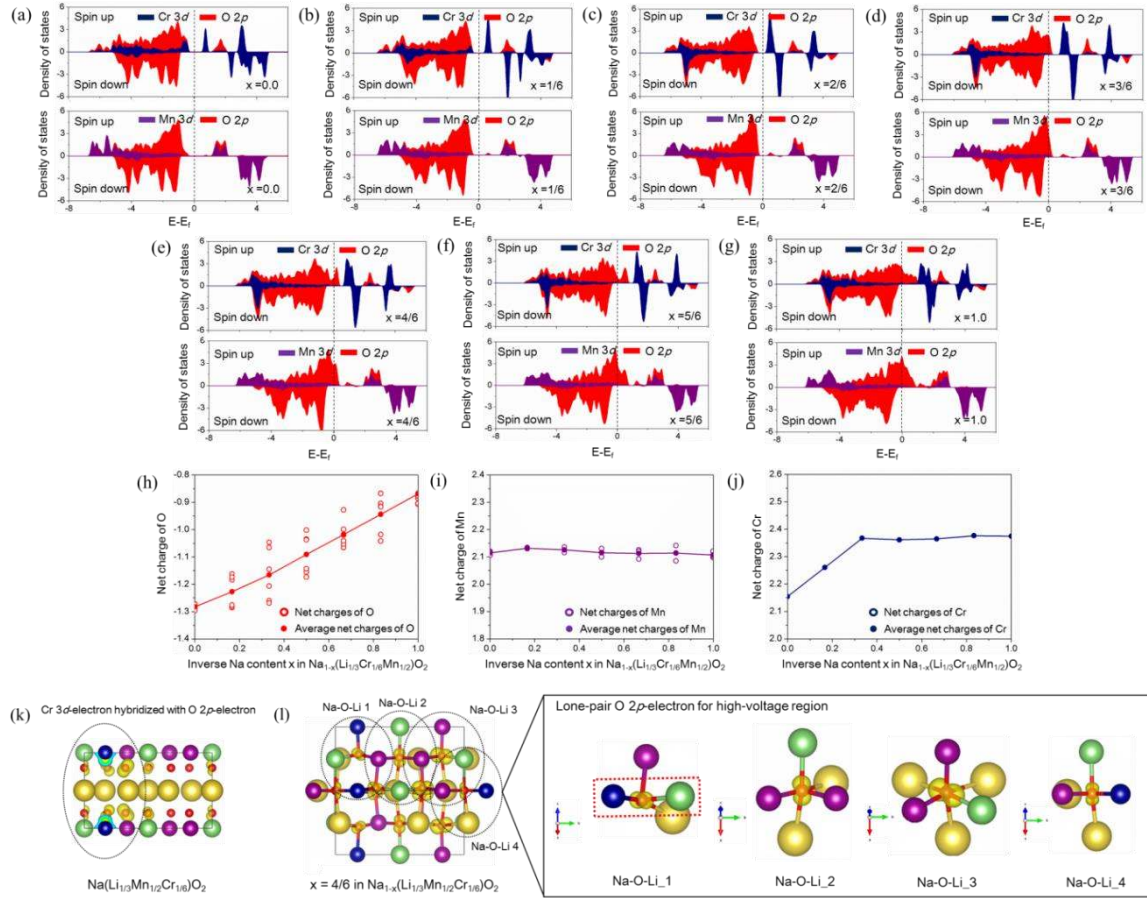
Figure 3.21 Combined profiles of the partial density of states (PDOS) of Cr (blue) and Mn $3d$ orbital electrons (purple) and O $2p$ orbital electrons (red) from (a) $x = 0.0$ to (g) $x = 1.0$ in $Na_{1-x}(Li_{1/3}Mn_{1/2}Cr_{1/6})O_2$. Net charges calculated by the Bader charge method for (h) O, (i) Mn, and (j) Cr as a function of the inverse Na content (x) in $Na_{1-x}(Li_{1/3}Mn_{1/2}Cr_{1/6})O_2$. Spatial electron distribution in the occupied band from -2 to 0 eV (Fermi level) in (k) $Na(Li_{1/3}Mn_{1/2}Cr_{1/6})O_2$ and (l) $Na_{4/6}(Li_{1/3}Mn_{1/2}Cr_{1/6})O_2$.

Mn⁴⁺ 3d-electron configuration

Cr⁴⁺ 3d-electron configuration
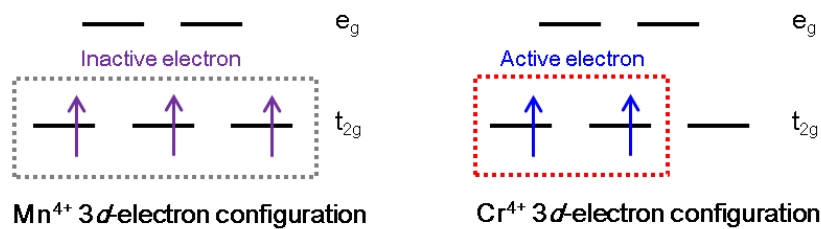
Figure 3.22 Schematic electronic configuration of Mn^{4+} (t_{2g}^3 e_g^0) and Cr^{4+} (t_{2g}^2 e_g^0) at the octahedral sites of the oxide based on crystal field theory. Compared to the stabilized Mn^{4+} electronic structure, the electronic configuration of Cr^{4+} is expected to be active toward oxidation, indicating a double redox behavior (Cr^{4+}/Cr^{6+}) upon Na extraction.
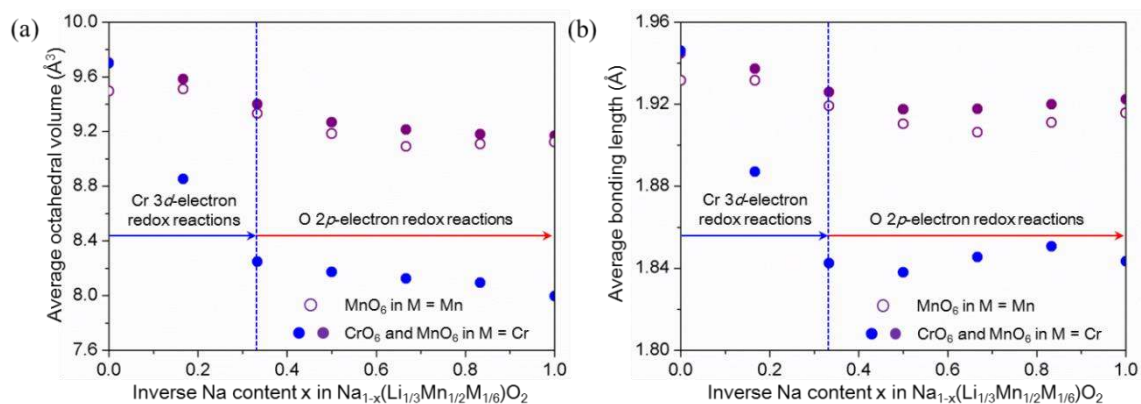
Figure 3.23 (a) Average octahedral volume of MnO_6 in $Na_{1-x}(Li_{1/3}Mn_{2/3})O_2$ and those of MnO_6 and CrO_6 in $Na_{1-x}(Li_{1/3}Mn_{2/3}Cr_{1/6})O_2$ at varying x values ($0 \leq x \leq 1.0$). (b) Average Mn–O bond length in $Na_{1-x}(Li_{1/3}Mn_{2/3})O_2$, and those of Mn–O and Cr–O in $Na_{1-x}(Li_{1/3}Mn_{2/3}Cr_{1/6})O_2$ at varying x values ($0 \leq x \leq 1.0$).

Table 3.1 Mismatch strains (lattice and area) generated between $x = 4/6$ and 1.0 in $Na_{1-x}(Li_{1/3}Mn_{2/3})O_2$ and $Na_{1-x}(Li_{1/3}Mn_{1/2}Cr_{1/6})O_2$.

Compound	Lattice mismatch strain			Area mismatch strain		
	a	b	c	ab	ac	bc
NLMO	0.1279	0.0725	-0.0869	0.1757	-0.2717	-0.1481
NLMCO	0.0068	0.0275	-0.1397	0.0347	-0.1689	-0.1417

Table 3.2 Structural formation energy of $Na(Li_{1/3}Mn_{2/3})O_2$ and $Na(Li_{1/3}Mn_{2/3}Cr_{1/6})O_2$, illustrating the difference between the rigid body mode of the $Na_0(Li_{1/3}Mn_{2/3})O_2$ and $Na_0(Li_{1/3}Mn_{1/2}Cr_{1/6})O_2$ structures and the fully relaxed $Na_0(Li_{1/3}Mn_{2/3})O_2$ and $Na_0(Li_{1/3}Mn_{1/2}Cr_{1/6})O_2$ structures.

Compound	Structural formation energy (eV)
$Na(Li_{1/3}Mn_{2/3})O_2$	-0.8715
$Na(Li_{1/3}Mn_{2/3}Cr_{1/6})O_2$	-0.6126

Table 3.3 C_{33} elastic constant as a function of the inverse Na content in $Na_{1-x}(Li_{1/3}Mn_{2/3})O_2$ and $Na_{1-x}(Li_{1/3}Mn_{1/2}Cr_{1/6})O_2$. For better understanding, the elastic constants are plotted in Figure 3.15c.

Inverse Na content (x)	Elastic constant C_{33}	
	$Na_{1-x}(Li_{1/3}Mn_{2/3})O_2$	$Na_{1-x}(Li_{1/3}Mn_{1/2}Cr_{1/6})O_2$
0.0	244.5072	248.7740
0.1667	215.9338	238.7789
0.3333	193.2726	226.6244
0.5	165.4752	186.9789
0.6667	133.1598	159.4715
0.8333	103.3250	135.0344
1.0	332.7202	132.3336

Table 3.4 Average octahedral volume (MnO_6 and CrO_6) and bond lengths (Mn–O and Cr–O) with respect to the inverse Na content (x) in $Na_{1-x}(Li_{1/3}Mn_{2/3})O_2$ and $Na_{1-x}(Li_{1/3}Mn_{2/3}Cr_{1/6})O_2$ ($0 \leq x \leq 1.0$). The octahedral volumes and bond lengths of MnO_6 and CrO_6 in $Na(Li_{1/3}Mn_{2/3}Cr_{1/6})O_2$ are larger than those in MnO_6 for $Na(Li_{1/3}Mn_{2/3})O_2$, which originate from the larger ionic radius of Cr^{4+} versus Mn^{4+}. The octahedral volume and bond lengths of CrO_6 drastically decrease up to $x = 0.3333$ in $Na_{1-x}(Li_{1/3}Mn_{2/3}Cr_{1/6})O_2$ compared to those of MnO_6 in $Na_{1-x}(Li_{1/3}Mn_{2/3})O_2$, reflecting the cationic redox reaction of the Cr $3d$ electrons (PDOS and net charges are shown in Figure 3.21) in octahedral configuration. All the calculated results are plotted in Figure 3.23.

Compounds: $Na_{1-x}(Li_{1/3}Mn_{2/3})O_2$ ($Na_{1-x}(Li_{1/3}Mn_{1/2}Cr_{1/6})O_2$)				
Inverse Na content	Average octahedral volume		Average bonding length (M-O)	
	MnO_6	CrO_6	MnO_6	CrO_6
0.0	9.4956 (9.7040)	(9.6975)	1.9316 (1.9448)	(1.946)
0.1667	9.5115 (9.5846)	(8.8533)	1.9316 (1.9373)	(1.8870)
0.3333	9.3319 (9.4005)	(8.2497)	1.9192 (1.9259)	(1.8425)
0.5	9.1857 (9.2685)	(8.1715)	1.9104 (1.9175)	(1.8380)
0.6667	9.0907 (9.2136)	(8.1259)	1.9063 (1.9177)	(1.8455)
0.8333	9.1088 (9.1804)	(8.0953)	1.9111 (1.9199)	(1.8507)
1.0	9.1230 (9.1701)	(7.9971)	1.9157 (1.9224)	(1.8434)

Chapter 4

Methodologies for Multiscale Design

4.1 Atomistic Approaches

4.1.1 Density Functional Theory

We have employed first-principles calculations (or *ab initio* calculations) requiring underlying information (e.g., nuclear charge, the number of electrons, and so on) for the first step of multiscale investigation, which is distinguished from empirical calculations using fitting parameters. Based on solving the time-independent Schrodinger equation with exchange-correlation potential $\hat{V}_{XC}$, the entire information of the given system is calculated in the form of wave function Ψ using density functional theory (DFT) as follows:[74-75]

$$\hat{H}\Psi = [\hat{T} + \hat{V} + \hat{U} + \hat{V}_{XC}]\Psi = E\Psi \tag{4.1},$$

where $\hat{H}$ represents the Hamiltonian operator, $\hat{T}$ is the kinetic energy operator, $\hat{V}$ is the potential energy operator from the external field, $\hat{U}$ is the

electron-electron interaction energy operator, and E indicates the total energy.

In this dissertation, the DFT method as implemented in the Vienna ab initio simulation package based on a plane-wave set with pseudopotentials of the projector augmented wave (PAW) was used throughout.[76] For the exchange-correlation functional according to Perdew-Wang 91,[77] the generalized gradient approximation (GGA) was applied to all the calculations. A Hubbard-type U correction into GGA (GGA+U) with spin-polarized calculations was used to take into account the strong correlation of the transition metals $3d$ band (i.e., t_{2g} band and e_g band, divided by crystal field splitting),[78] and the corresponding value for Mn, Cr, Fe, and V were obtained from previous reports.[10-11, 79] For more accurate Li$^+$ and Na$^+$ descriptions, the Na pseudopotential was covered with one $3s$-electron and six $2p$-electron, and the Li was dealt with one $2s$-electron and two $1s$-electron as the valence states. To sample the k-point in the reciprocal space, the Monkhorst-Pack method was used with $4 \times 4 \times 4$ meshes, and the cut-off energy was set to 400 eV for the standard computational parameters. By contrast, this parameter had an increased cut-off energy of 600 eV for mechanical modulus calculations. In all calculations, the lattice parameters and atomic coordinates were fully relaxed to gain the optimized thermodynamic quantities and electronic structures.

4.1.2 Thermodynamics and Kinetics

It is important to compare thermodynamic stabilities and kinetic possibilities of various atomic structures for various modifications of electrodes such as Li/Na mixing, Na or Li ions extraction, oxygen defect and evolution, elemental doping, and so on.

For the phase stability considering all possible Li/Na atomic configurations, the formation energy of mixing enthalpy (ΔH_{mix}) is determined as follows:

$$\Delta H_{mix}^{Li/Na} = E_{Li_{1-x_{Li}}Na_{x_{Li}}M_{0.5}O_{1.5}} - x_{Li}E_{NaM_{0.5}O_{1.5}} - (1-x_{Li})E_{LiM_{0.5}O_{1.5}} \qquad (4.2),$$

where x_{Li} indicates the normalized content of Li ($0.0 \leq x_{Li} \leq 1.0$), and E represents the system total energy calculated from DFT calculations. Based on the calculated result of the above Li/Na mixing value, the formation energy of mixing enthalpy considering all possible Na/vacancy atomic sites, $\Delta H_{mix}^{Na/vacancy}$, is used to investigate the thermodynamic phase stability as follows:

$$\Delta H_{mix}^{Na/vacancy} = E_{Na_{1-x}(Li_{1/3}M_{2/3})O_2} - xE_{(Li_{1/3}M_{2/3})O_2} - (1-x)E_{Na(Li_{1/3}M_{2/3})O_2} \qquad (4.3),$$

where x refers to the normalized content of inverse Na content (or vacancy, $0.0 \leq x \leq 1.0$). For the kinetic investigations, elemental migrations were simulated with various pathways using the climbing-image nudged elastic band (ciNEB) method.

4.1.3 Electrochemisty

The equilibrium desodiation potential is directly related to the different chemical potential between the cathode and the anode.[80] Like LIBs, even though it is difficult to calculate the chemical potential of Na in cathode materials as a function of Na content, the average desodiation potential, $\bar{V}$, can be easily obtained comparatively from total system energy values calculated using DFT as follows:

$$\bar{V} = -\frac{\Delta G_r}{(Na_{x2} - Na_{x1})F} \qquad (4.4),$$

where $(Na_{x2} - Na_{x1})$ is the two Na ions intercalation limits, F is the Faraday constant, and ΔG_r is the change of the Gibbs free energy along with the sodiation and desodiation reactions. The change of the Gibbs free energy, $\Delta G_r = \Delta E_r + P\Delta V_r - T\Delta S_r$, can be approximated by the variation of the internal energy (ΔE_r), because a very small change in volume (ΔV_r) critically does not affect the free energy (P is the pressure). Also, the thermal energy term ($T\Delta S_r$) mainly does not have an influence on the free energy owing to the small amount of entropy variation (ΔS_r) with the absolute temperature (T) at 0 K of DFT calculations. Therefore, the average desodiation potential obtained by DFT calculations can be easily expressed as:

$$\bar{V} = -\frac{E_{Na_{Na_{x2}}(Li_{1/3}M_{2/3})O_2} - E_{Na_{Na_{a1}}(Li_{1/3}M_{2/3})O_2} - (x_2 - x_1)E_{Na}}{(Na_{x2} - Na_{x1})} \qquad (4.5),$$

where E_{Na} represents the chemical potential of sodium metal.

4.1.4 Crystal and Ligand Field Approaches

For investigations on transition metal coordination complexes of cathode materials, we introduced the crystal field theory (CFT), which is developed by H. Bethe and subsequently modified toward ligand field theory (LFT) by J.H. Van Vleck.[81] On the basis of CFT, the interactions between transition metal ions and corresponding ligands are assumed to be electrostatic, and the ligands are considered to be point charges.

In this dissertation, we have mainly discussed the CFT in terms of the octahedral field, since almost cathode materials for LIBs and SIBs compose of M ions surrounded by six oxygen ions in octahedral sites (octahedron).[30, 82] Figure 4.1 illustrates the schematic energy state divided into two distinct sets of orbitals, which are denoted conventionally as the e_g and t_{2g} bands by crystal filed splitting (CFS). The redox mechanism of transition metals and oxygen is entirely determined by the stabilization of the crystal field of coordination geometries. From projected partial density of states (PDOSs) profiles calculated by DFT, occupied and unoccupied electrons are determined by electronic structure analysis.

4.2 Multiscale Approaches

4.2.1 Homogeneous Chemomechanical Stress

The larger size of sodium ion compared to the size of lithium ion results in the large volume change of the desodiated structures, leading to large chemomechanical stress. The chemomechanical stress behaviors can be predicted phenomenologically using mechanical constants and chemomechanical strain calculated by the atomistic simulations. As one of the mechanical constants, the bulk modulus is gained using the Birch-Murnaghan equation of states based on DFT static calculations as follows:[83]

$$E(V) = E_0 + \frac{9V_0 B_0}{16} \left\{ \left[\left(\frac{V_0}{V} \right)^{\frac{2}{3}} - 1 \right]^3 B_0' + \left[\left(\frac{V_0}{V} \right)^{\frac{2}{3}} - 1 \right]^2 \left[6 - 4 \left(\frac{V_0}{V} \right)^{\frac{2}{3}} \right] \right\} \tag{4.6},$$

where $E(V)$ is the internal energy as a function of volume (V). V_0 and E_0 represent the volume and internal energy at equilibrium state; and, bulk modulus parameters of B_0 and B_0' can be obtained from the fitting equation. The calculated bulk moduli at each Na content are fitted using a fourth order polynomial function to reflect nonlinearity of material properties by Na-extraction as follows:

$$B(x) = B_1 x^4 + B_2 x^3 + B_3 x^2 + B_4 x + B_5 \tag{4.7},$$

where B_1, B_2, B_3, B_4, and B_5 are phenomenological coefficient for the polynomial function of bulk modulus. Considering the Na/vacancy mixing enthalpy values at ground states, the structural parameters (unit cell volume and a, b, and c lattice parameters) are calculated at each Na content based on DFT calculations; and then, the obtained structural parameters are recalculated considering the fully sodiated structures from the chemomechanical strain point of view ($\varepsilon_V = \dfrac{V_{Na_x(Li_{1/3}Mn_{2/3})O_2} - V_{Na(Li_{1/3}Mn_{2/3})O_2}}{V_{Na(Li_{1/3}Mn_{2/3})O_2}}$). For example, the chemomechanical volumetric strains are fitted using a fourth order polynomial function to be consistent with the order of function of mechanical constants as follows:

$$\varepsilon_V(x) = \varepsilon_{V_1} x^4 + \varepsilon_{V_2} x^3 + \varepsilon_{V_3} x^2 + \varepsilon_{V_4} x + \varepsilon_{V_5} \tag{4.8}$$

where ε_{V_1}, ε_{V_2}, ε_{V_3}, ε_{V_4}, and ε_{V_5} are phenomenological coefficient for the polynomial function. Using the fitted bulk modulus and chemomechanical strain, the chemomechanical volumetric stress ($\sigma_V(x)$) can be predicted as follows:

$$\sigma_V(x) = B(x)\varepsilon_V(x) \tag{4.9}$$

4.2.2 Homogeneous Bulk Free Energy and Chemical Potential[30]

On the basis of the formation energy of Li/Na mixing enthalpy in Equation (4.2), thermodynamic ground states as a function of Li content are determined.

Among the ground states, the most thermodynamically stable phase with a proper Li content is found. To evaluate the phase stability during charge, further calculations of the formation energy of Na/vacancy mixing enthalpy in Equation (4.3) are carried out. Considering the thermodynamic mixing energy values with the convex hull analysis, one-phase and two-phase reaction regions can be predicted from x_i (initial concentration) to x_f (final concentration). From the predicted reaction regions, the modified formation energy of mixing enthalpy can be calculated as follows:

$$\Delta H_{mix}^{i,f} = E_{Na_x(Li_{1/3}M_{2/3})O_2} - \frac{x-x_i}{x_f-x_i} E_{Na_{x_f}(Li_{1/3}M_{2/3})O_2} - \frac{x_f-x}{x_f-x_i} E_{Na_{x_i}(Li_{1/3}M_{2/3})O_2} \qquad (4.10).$$

Not only to calculate spinodal decomposition barrier S_b but also to gain homogeneous mixing enthalpy ΔH_{mix}^{hom}, the minimum mixing enthalpies at each Na content were carefully fitted using the double-well function with the enthalpy coefficient Ω as follows:

$$\Delta H_{mix}^{hom} \approx \Omega(x-x_i)^2(x_f-x)^2 \approx \Delta H_{mix}^{i,f} \qquad (4.11)$$

The theoretical background of the double-well function is taken from the Landau-type free energy models. The spinodal decomposition barrier (S_b) can be obtained using the condition of $\dfrac{\partial \Delta H_{mix}^{hom}}{\partial x} = 0$ in the range of $\dfrac{\partial^2 \Delta H_{mix}^{hom}}{\partial x^2} < 0$. The phase separation in the two-phase reaction region is generated between the two

90

stable phases (the two potential wells) connected by common tangent lines. To develop the homogeneous mixing enthalpy to the homogeneous thermodynamic free energy, we employ the entropy of configurational mixing (ΔS_c^{hom}) based on Fermi distribution as follows:

$$\Delta S_c^{hom} = -k_B[x \ln x + (1-x)\ln(1-x)] \tag{4.12},$$

where k_B presents the Boltzmann constant. Therefore, we can construct the homogeneous bulk free energy as follows:

$$f_h = \Delta G_{mix}^{hom} = \Delta H_{mix}^{hom} - T\Delta S_c^{hom} = \Omega(x-x_i)^2(x_f-x)^2 + k_BT[x \ln x + (1-x)\ln(1-x)] \tag{4.13}.$$

4.2.3 Phase Separation Kinetic Simulations

To describe the mesoscale phase separation phenomena, the Cahn-Hilliard equation[84] is solved by adopting the Cahn-Hilliard free energy functional, G_{CH}, as follows:

$$G_{CH} = \int_V \rho_n \left\{ f_h + \frac{\kappa_i^f}{2}|\nabla x|^2 \right\} dV \tag{4.14},$$

where ρ_n presents the number of Li sites per volume, κ_i^f is the gradient energy coefficient, and f_h is determined in equation (4.13). The energy coefficient is highly affected by the shape of double-well potential and the

91

interfacial width as the nearest-neighbor distance of the charge carrier in the electrode (characteristic length: λ), defined as follows:[85]

$$\kappa_i^f = \frac{n_d}{3}\lambda^2\Omega \tag{4.15}$$

where n_d indicates the number of possible diffusion directions of the charge carrier.

4.3 Experimental Details

4.3.1 Material Synthesis

Based on a conventional solid state reaction, stoichiometric amounts of precursors (e.g., Na_2CO_3, Li_2CO_3, and $MnCO_3$) were mixed thoroughly in a mortar, or dissolved in deionized water under continuous stirring for several hours at room temperature. The solution was then dried at approximately 80 ℃ while stirring overnight. The dried solid product was ground and heated in alumina crucibles at certain temperature.

4.3.2 Material Characterizations

Using an X-ray diffractometer (XRD, Empyrean PANalytical) equipped with Cu-Kα radiation (λ = 1.5418 Å) in the 2θ range of 10°−80°, the as-synthesized powder was characterized, and then based on the collected XRD patterns,

Rietveld refinements were carried out using HighScore Plus software (PANalytical). In order to observe the morphology, particle size, and elemental distribution, a field-emission scanning electron microscopy (FESEM, JEOL JSM-7000F) coupled with energy-dispersive X-ray spectroscopy (EDS) were used. To identify the microstructure and atomic configuration, a scanning transmission electron microscopy (STEM, JEOL ARM-200F) was employed. Moreover, to examine the homogeneous distribution of elements and the corresponding elemental ratios of the prepared powders, high-resolution transmission electron microscopy (HRTEM, JEOL ARM-200F) coupled with EDS were used. The oxidation states of transition metals were characterized by X-ray photoelectron spectroscopy (XPS) using a sigma probe spectrometer (Thermo Scientific). The chemical composition of the elements was confirmed by inductively coupled plasma mass spectroscopy (ICP-MS, Bruker Aurora M90).

4.3.3 Electrochemical Measurements

In order to examine electrochemical properties, the electrode was prepared from a cathode slurry including the active material, carbon black (Super-P), and a polyvinylidene fluoride (PVDF) binder dissolved in an N-methyl pyrrolidinone (NMP) solution. After the slurry was coated on an Al foil as a current collector, the electrode was dried at 80 ℃ for 3 h to evaporate NMP. The as-prepared

electrode was pressed uniformly and punched and then dried again at 120 ℃ overnight in a vacuum oven. CR2032 coin-type half cells were assembled in a glove box, using Na metal as the counter and reference electrode. A glass fiber was used as a separator and 1.0 M $NaClO_4$ in ethylene carbonate/propylene carbonate in a 1:1 volume ratio containing 2 wt% fluoroethylene carbonate was used as the electrolyte (PANAX ETEC Co. Ltd.). The loading amount of active materials and electrode density were maintained. The test cells were galvanostatically charged and discharged using a MACCOR 4300K galvanostat.
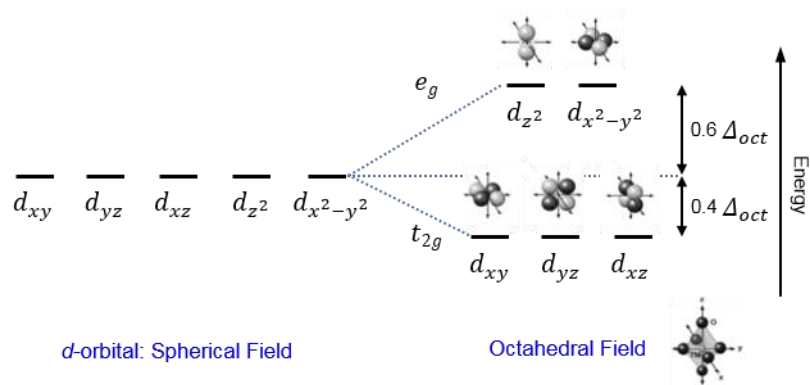
Figure 4.1 Schematic energy levels of d-orbitals in the spherical field and those in the octahedral field. In general, the five degenerated d-orbitals are divided into two distinct sets of orbitals that are denoted conventionally as the e_g and t_{2g} bands by crystal field splitting; and the e_g orbitals are destabilized by 0.6 Δ_{oct} and the t_{2g} orbitals are stabilized by 0.4 Δ_{oct}.

Chapter 5

Conclusions

This dissertation based on multiscale design and experimental validations provides a new paradigm (anionic redox: O^{2-}/O^-) beyond the conventional reaction mechanism (cationic redox: $M^{n+}/M^{(n+1)+}$, M: transition metals) to overcome the energy density limitation of the cathode materials for electrochemical energy storages such as SIBs, also enabling new $Na(Li_{1/3}M_{2/3})O_2$ and advanced $Na(Li_{1/3}M_{2/3(1-y)}M_{cy})O_2$ analogues (transition metals featuring stabilized M^{4+} and with cationic redox active M_c^{4+} species) for further advances in SIBs. Utilizing multiscale approach from first-principles calculations, mixing enthalpies, electronic structures, crystal field theory, ligand field theory, homogeneous free energies, homogeneous chemical potentials, chemomechanics to phase field simulations, this combined methodology was used to not only rationally design high-energy-density cathodes to but also understand the atomic physics and chemistry including atomic-scale

thermodynamics and kinetics, chemomechanical strain and stress behaviors, particle-level phase separation during intercalation process.

Using this multiscale-based framework, as the first step to develop high-energy-density cathodes for SIBs, we discovered low-cost, high-voltage and -capacity $Na(Li_{1/3}Mn_{2/3})O_2$ for the first time. In-depth understandings of Li_2MnO_3 during delithiation for LIB cathodes are critical for the rational design of $Na(Li_{1/3}Mn_{2/3})O_2$. Considering the site preference of Na in the Li_2MnO_3 structure, the thermodynamically stable structure of $Na(Li_{1/3}Mn_{2/3})O_2$ was obtained. As the intrinsically lower redox potentials for SIB cathodes compared to LIB cathodes, $Na(Li_{1/3}Mn_{2/3})O_2$ showed a redox potential of ≈ 4.2 V versus Na/Na^+ without the creation of free volume in the mixed layer, because Li-extraction requires a higher voltage than Na-extraction. Interestingly, the anionic redox (O^{2-}/O^{n-}) beyond the conventional cationic redox $(M^{n+}/M^{(n+1)+}$, M: transition metals) was used to gain electrochemical capacity. However, further studies were required to not only retain the redox reactions at the high voltage range $(\approx 4.2$ V versus $Na/Na^+)$ during charge/discharge, because phase separation accompanied by large structural changes are expected to occur above $x = 0.6667$ in $Na_{1-x}(Li_{1/3}Mn_{2/3})O_2$, but also increase the low voltage in the initial desodiation region owing to the phase change from O3 to P2.

To resolve the two existing requirements for high energy density cathode materials for SIBs in $Na(Li_{1/3}Mn_{2/3})O_2$ during desodiation, as the second step,

97

we rationally designed $Na(Li_{1/3}Mn_{1/2}Cr_{1/6})O_2$ based on the detailed analysis of the thermodynamic energy landscape of $Na(Li_{1/3}Mn_{2/3})O_2$. Considering the desodiaton potentials calculated by the first-principles method, $Na(Li_{1/3}Mn_{1/2}Cr_{1/6})O_2$ was found to exhibit a higher low-voltage (≈ 2.445 V versus Na/Na^+) and similar high-voltage behavior (≈ 4.2 V versus Na/Na^+) than $Na(Li_{1/3}Mn_{2/3})O_2$, $Na(Li_{1/3}Mn_{1/2}V_{1/6})O_2$, and $Na(Li_{1/3}Mn_{1/2}Fe_{1/6})O_2$. From the thermodynamics viewpoint, the reduced formation energy (ΔH_1 ca. -0.221 eV) for $Na(Li_{1/3}Mn_{1/2}Cr_{1/6})O_2$ results in higher redox potentials in the low-voltage region. The homogeneous bulk free energy of $Na(Li_{1/3}Mn_{1/2}Cr_{1/6})O_2$ for $4/6 \leq x \leq 1.0$ indicated a much lower S_b value and a slower phase separation in $Na(Li_{1/3}Mn_{2/3})O_2$ with a smaller gap of thermodynamic hysteresis than for the other oxides. Moreover, the chemomechanical strain and stress for $Na(Li_{1/3}Mn_{1/2}Cr_{1/6})O_2$ in the phase change (reduced tensile stress) and separation (reduced compressive stress) regions were distinctively smaller than in the other cases. The formation of short O–O bonds in $Na_0(Li_{1/3}Mn_{2/3})O_2$ lead to the electrochemically inactive phase $Na_0(Li_{1/3}Mn_{2/3})O_2$, whereas the O–O formation between the mixed layers was not observed in $Na_0(Li_{1/3}Mn_{1/2}Cr_{1/6})O_2$. Finally, the mesoscale phase separation kinetics was much slower for $Na(Li_{1/3}Mn_{1/2}Cr_{1/6})O_2$ than for $Na(Li_{1/3}Mn_{2/3})O_2$, which was predicted to result in better cyclic performance. Regarding the redox mechanism, the cationic redox reactions involving the Cr $3d$ electrons reduced the destabilization of the oxygen

framework induced by the anionic redox reaction of the O lone-pair during desodiation.

Our discovered cathode materials designed and realized by the multiscale framework and experimental validation are significantly meaningful for the rational design of battery electrodes without a lot of empirical approaches based on experiments, providing breakthroughs to overcome the energy density limitation of the cathode materials for SIBs; also, enabling new class of promising cathode materials for further advances in SIBs. On the basis of first-principles calculations, this multiscale-based design approach including electrochemisty, thermodynamics, phase separation kinetics, electronic structures, atomic deformations, chemomechanical stress opens up an exciting direction for the development of rechargeable batteries. Regarding this multiscale design and analysis with experiments, we also investigated various cathode materials for advances of LIBs and SIBs. The corresponding results are provided in Appendix. Furthermore, the present methodology consisting of fundamental physics and chemistry is considered to be applied to assorted electrode systems such as batteries, capacitors, fuel cells, and even catalyst for enhancing their performance and designing new materials.

Appendix

APPENDIX A: Design of Nickel-rich Layered Oxides Using *d* Electronic

Donor for Redox Reactions

A growing demand for large-scale energy storage applications (e.g., electric vehicles and electric energy storage systems) has expedited the need for cathode materials with high Li^+ storage capability; such materials will aid in the fabrication of advanced LIBs with high energy and high power.[2, 9] So far, among commercialized cathode materials, $LiCoO_2$ has widely been used in LIBs because of its superior charge-discharge rate capability and its high working voltage (i.e., ≈4.0 V).[86-89] However, the use of $LiCoO_2$ is gradually decreasing because of its small practical capacity, high production cost, and the toxicity of the Co it contains. Such shortcomings have encouraged many researchers to develop other layered cathode materials consisting of lower Co ratios.[90-92]

More recently, Ni-rich layered oxides have been extensively studied as an alternative cathode material because of their relatively higher reversible capacity (~180 mAh g^{-1}) and lower cost as compared with commercialized $LiCoO_2$.[93-94] In this regard, multi-component layered $LiNi_{1-x-y}Co_xMn_yO_2$ (NCM) cathodes have

demonstrated significant success in commercial use. Because it is essential to increase the Ni content in order to further increase the reversible capacity, significant attention has been continuously devoted to increasing the Ni content in the layered cathodes.[95-96] In fact, even small increases in the Ni content can allow for a higher reversible capacity, although significant performance fading (as regards cyclability and rate capability) of the cathode results in structural instability that arises from the high Ni^{2+} content.[97-98]

To resolve the abovementioned problems, many research groups have focused on i) adjusting the composition of transition metals (TMs) and ii)[99-100] substituting different TMs or non-TMs into the layered cathode structure in order to ensure high reversible capacity, stable cyclic performance, and the structural stability of the cathode.[101-105] Recently, Sun et al. reported on a concentration-gradient layered cathode, which was designed to improve electrochemical performance and meet rigorous safety requirements for commercial use.[106] In another study by Cho and co-workers, a pillar layer was introduced on the surface of the layered cathode in order to suppress inter-slab collapse and prevent particle pulverization.[107] Nevertheless, even if such efforts represent significant improvements upon the performance of layered cathodes with high Ni content through the modification of the physicochemical properties (i.e., extrinsic characteristics) of materials, further improvement is still required in order to secure successful implementation on a commercial scale. Although studies of developing battery performance from the practical perspective have been

intensively conducted, theoretically in-depth understanding of the multi-component layered oxides has not yet been clearly understood. Considering those underlying viewpoints, it is strongly important to control the intrinsic properties of materials, which directly affect the electrochemical redox behavior of TMs in the layered cathodes. In this regard, we introduce a material design concept of multi-component layered cathodes using an electronic donor based on a crystal field splitting with the electronegativity (i.e., the tendency of an atom to attract electrons towards itself) of the TMs they contain. We then demonstrate its correlation with electrochemically redox behaviors. In other words, oxidation states of TMs in the multi-component system could be changed into different chemical states, because the redox electrons of TMs are affected by the difference in their electronegativities considered with a crystal field splitting.[108] Thus, it is expected that the electrochemical performance of the multi-component layered cathode could be directly affected by considering a crystal field splitting and adjusting the electronegativity of TMs in the structure.

We firstly investigated the correlation between the Mn ratio and the electrochemical behavior of the layered NCM cathode based on the theoretical calculations and experimental observations. Through GITT measurements, we found that the equilibrium potential of the NCM cathode was highly dependent on the Mn ratio in the structure; this can be explained by the fact that electrons can be transferred from Mn to Ni owing to their electronic structures based on a crystal field splitting and their different electronegativities (Figure A.1-8 and

Table A.1-3). Taking into account a crystal field splitting of TMs with electronegativities, we finally suggest that V would be a promising candidate for a doping element, functioning as an electronic donor with more transferable electrons as compared with Mn (Figure A.9). Our findings from the theoretical calculations and experimental observations are not only helpful to understanding the underlying relationship between a crystal field splitting with electronegativity and TMs interactions, but may also provide a conceptual design method based on the perspective of electronic structures. Considering our theoretical calculations in the NCV layered structure, elements possessing more transferable electrons with functioning as an electronic donor to redox TMs (e.g., Ni) would be a promising candidate to realize electrochemically better performance in the layered cathodes (i.e., high Ni-content layered oxides). We also believe that the design concept will be further applied to many other associated with materials in various fields, and our group will report designed cathode materials.
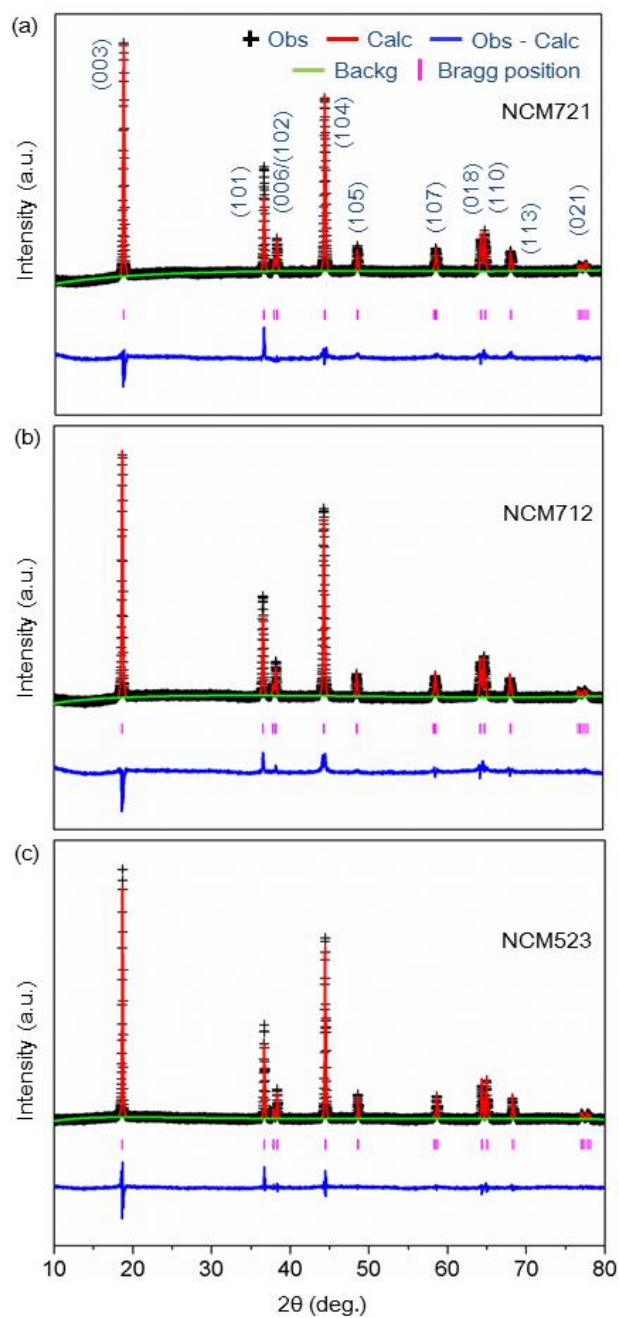
Figure A.1 Rietveld refinement of X-ray diffraction (XRD) patterns of (a) NCM523, (b) NCM712, and (c) NCM721.
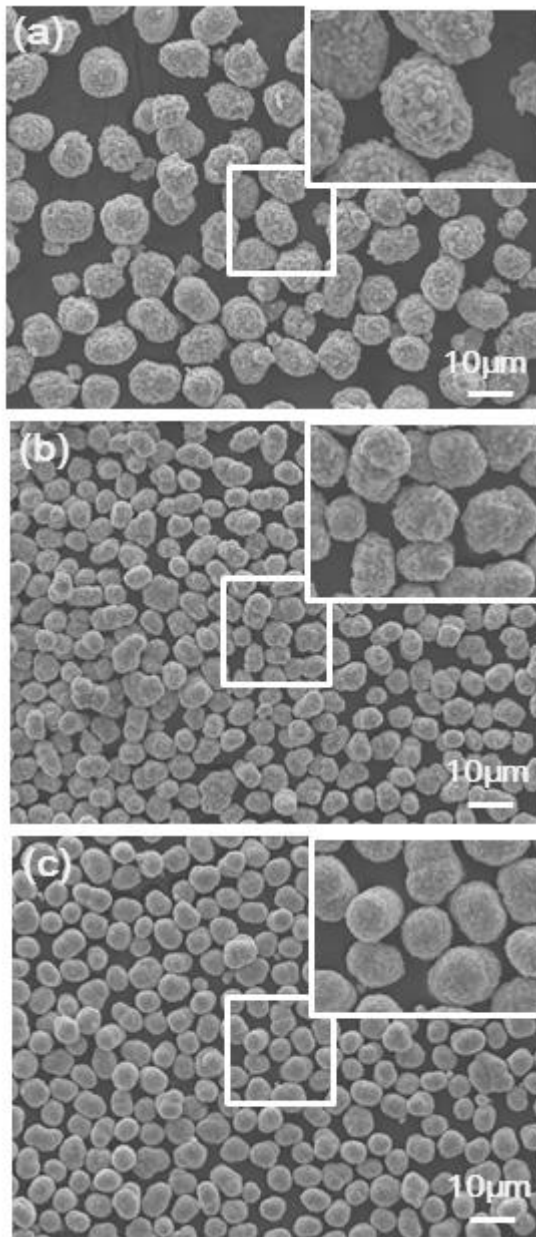
Figure A.2 Field emission scanning electron microscope (FESEM) images of (a) NCM523, (b) NCM712, and (c) NCM721.

서울대학교
SEOUL NATIONAL UNIVERSITY
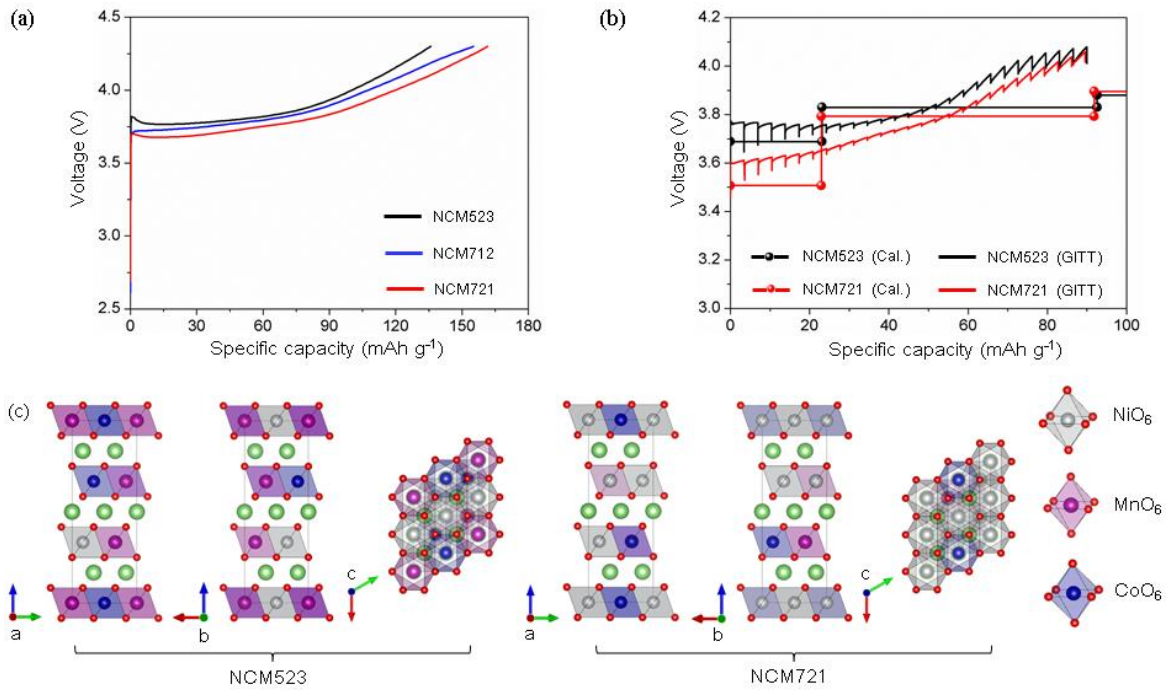
Figure A.3 (a) Galvanostatic first charge curves of NCM523 (black line), NCM712 (blue line), and NCM721 (red line) recorded with a constant specific current of 0.5 C rate in a voltage range between 2.5 and 4.3 V *vs.* Li/Li$^+$. (b) A combined graph of galvanostatic intermittent titration technique (GITT) profiles during the initial charge to 4.0 V *vs.* Li/Li$^+$ and calculated delithiation potentials for NCM523 and NCM721. (c) Atomic models of NCM523 and NCM721 with octahedra of NiO$_6$, MnO$_6$, and CoO$_6$.
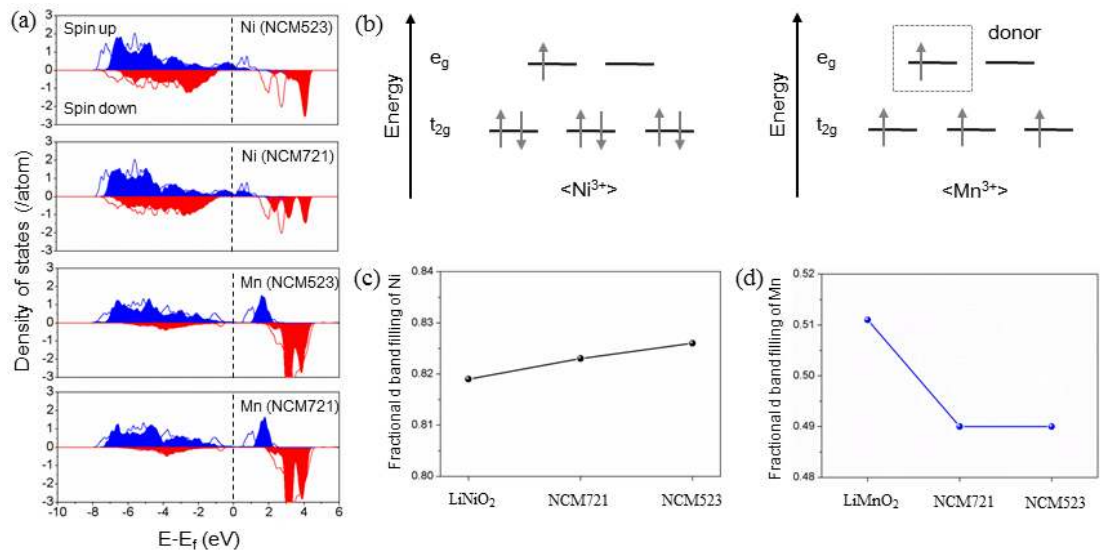
Figure A.4 (a) $3d$-electron partial density of states (PDOS) of Ni and Mn ions in both NCM523, NCM721, and each pristine layered oxide: $LiNiO_2$ and $LiMnO_2$. (b) Occupied electrons in $3d$ orbitals of Ni^{3+} and Mn^{3+} positioned in an octahedral site and the corresponding schematic energy levels known as e_g and t_{2g} band. Fractional band fillings of (c) Ni ions and (d) Mn ions calculated from the above structures, respectively.
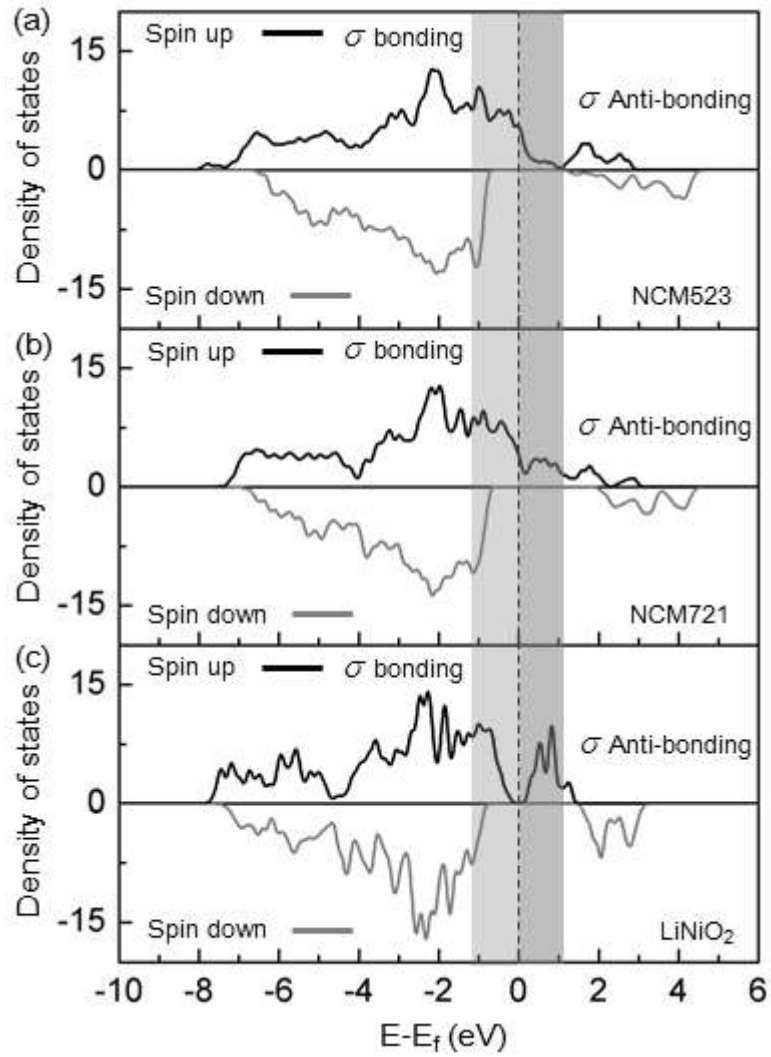
Figure A.5 2*p*-electron partial density of states (PDOS) of O ions in (a) NCM523, (b) NCM721, and (c) LiNiO$_2$.
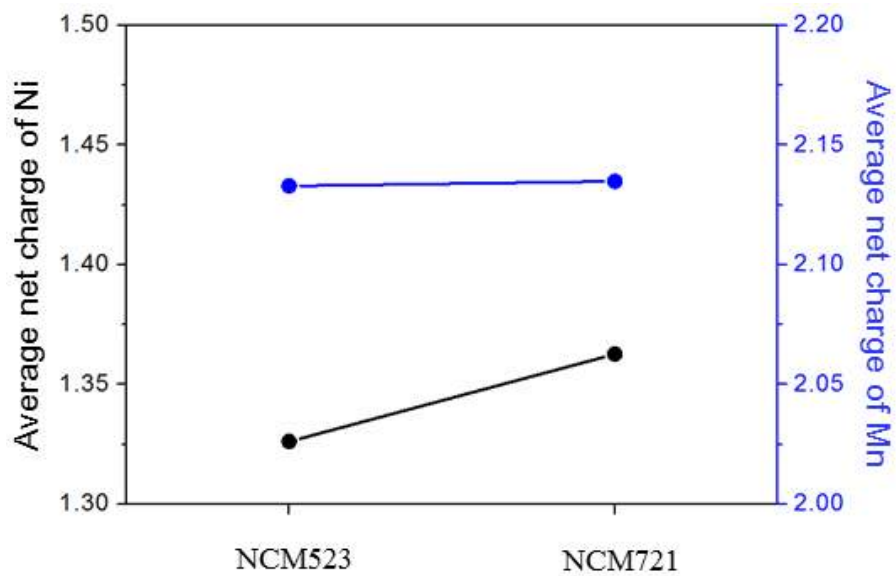
Figure A.6 Average net charge of Ni ions (black circles) and Mn ions (blue circles) in NCM523 and NCM721.
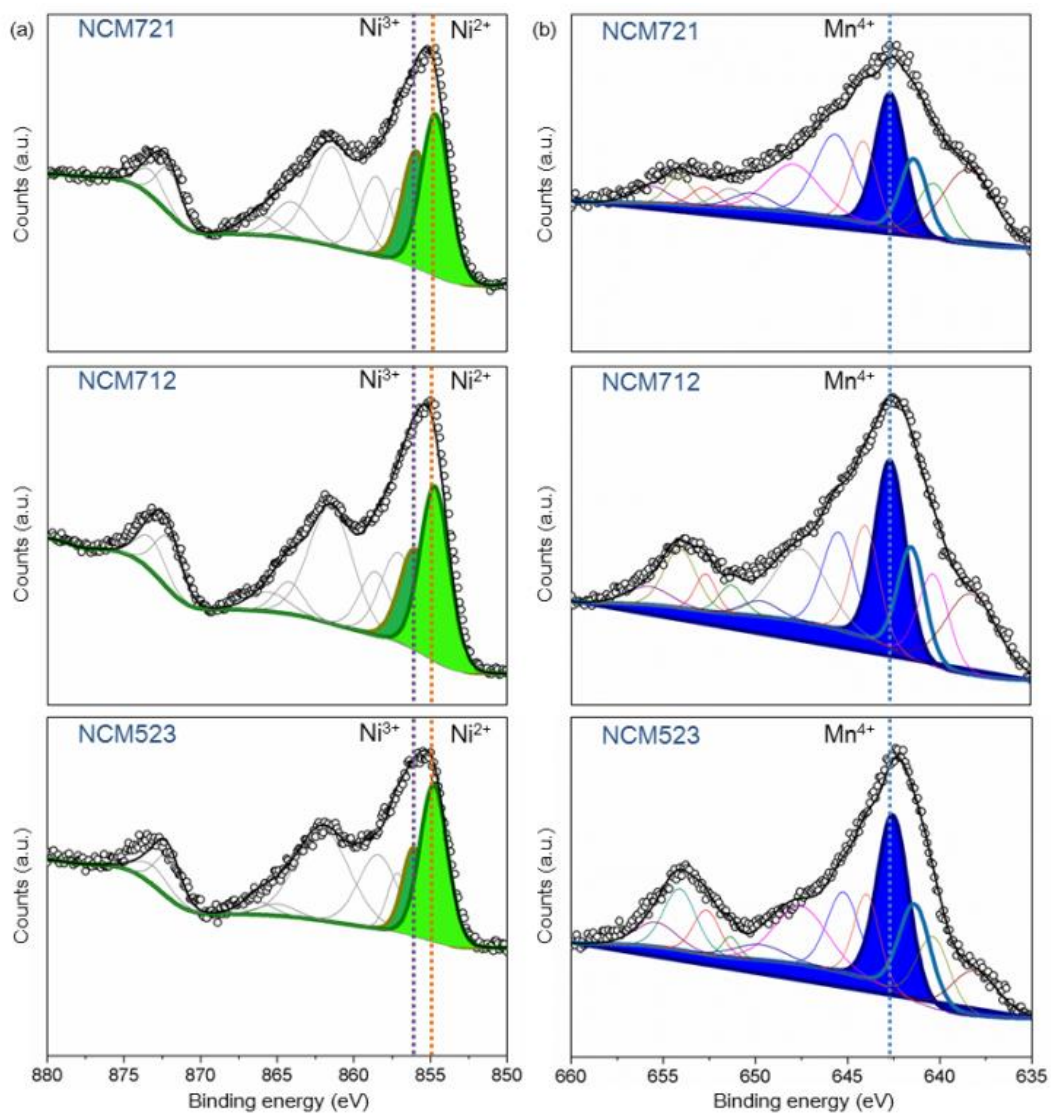
Figure A.7 X-ray photoelectron spectroscopy (XPS) spectra of (a) Ni $2p$ and (b) Mn $2p$ in NCM523, NCM712, and NCM721.
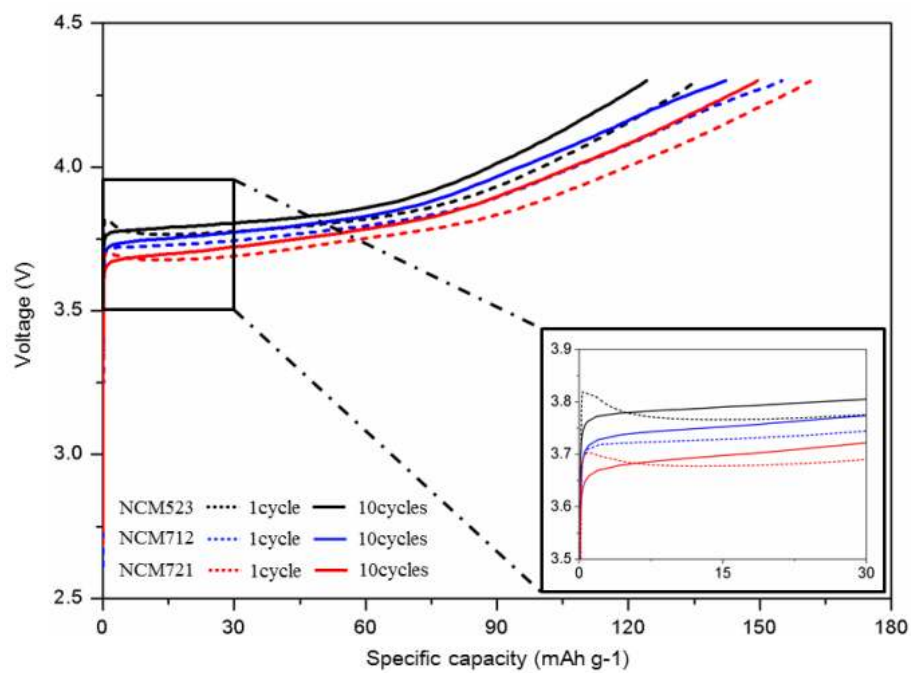
Figure A.8 First charge (dashed lines) and 10th charge (solid lines) of the three samples with a constant specific current of 0.5 C rate and a voltage ranging from 2.5 V to 4.3 V vs. Li/Li$^+$.
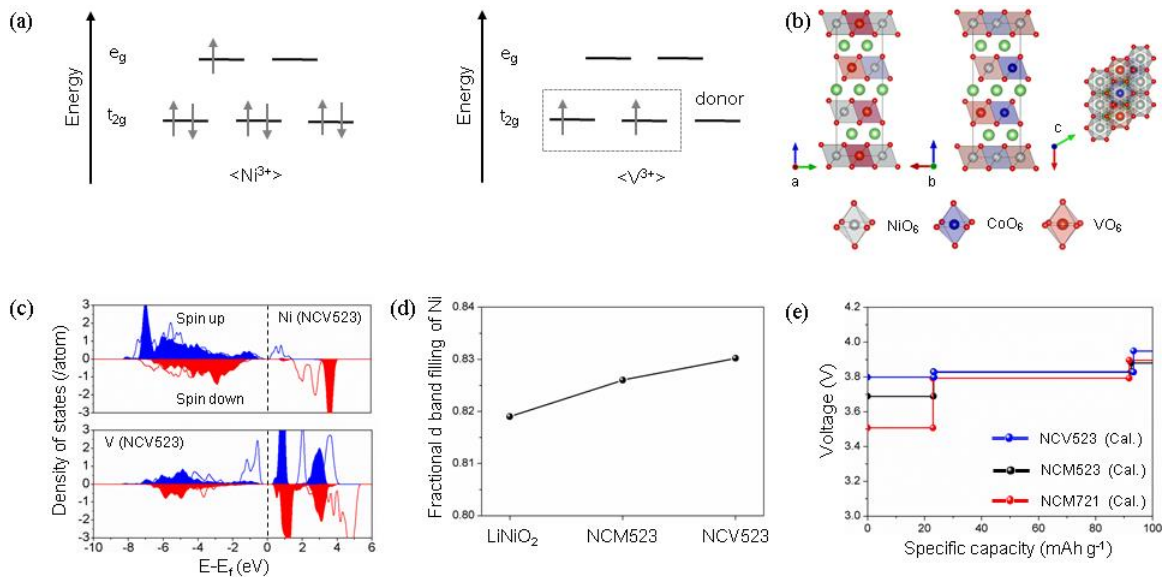
Figure A.9 (a) Occupied electrons in $3d$ orbitals of Ni^{3+} and V^{3+} positioned in an octahedral site and the corresponding schematic energy levels known as e_g and t_{2g} band. (b) Atomic models of NCV523 with octahedra of NiO_6, CoO_6, and VO_6. (c) $3d$-electron partial density of states (PDOS) of Ni and V ions in NCV523 (shaded regions), and each pristine layered oxide: $LiNiO_2$ and $LiVO_2$ (solid line). (d) Fractional band fillings of Ni ions in pristine layered oxide ($LiNiO_2$), NCM523 and NCV523. (e) Calculated de-lithiation potentials for NCM721, NCM523 and NCV523.

Table A.1 Comparison of lattice parameters of the NCM layered structures obtained from experiment (Rietveld refinement results) and first-principles calculation.

Composition	Lattice parameters				R_{wp}	R_{exp}
	a (Å)		c (Å)			
	Exp.	DFT	Exp.	DFT		
$LiNi_{0.5}Co_{0.2}Mn_{0.3}O_2$ (NCM523)	2.8687	2.8740	14.2350	14.1172	2.61	1.25
$LiNi_{0.7}Co_{0.1}Mn_{0.2}O_2$ (NCM712)	2.8738		14.2237		2.44	1.29
$LiNi_{0.7}Co_{0.2}Mn_{0.1}O_2$ (NCM721)	2.8665	2.8664	14.1895	14.0666	2.69	1.17

Table A.2 Chemical compositions results of inductively coupled plasma mass spectroscopy (ICP-MS) for NCM523, 712 and 721.

Compounds	Elements	Content (ppm)	Weight (g)	Wt (%)	Mol (%)	Fraction
NCM523	Li	71182	13.92	7.12	200.50	1.09
	Ni	276213	54.00	27.62	92.01	0.50
	Co	113478	22.19	11.35	37.65	0.20
	Mn	154665	30.24	15.47	55.04	0.30
NCM712	Li	71441	13.97	7.14	201.23	1.04
	Ni	404976	79.17	40.50	134.90	0.70
	Co	60718	11.87	6.07	20.14	0.11
	Mn	106300	20.78	10.63	37.83	0.19
NCM721	Li	68686	13.43	6.87	193.46	1.04
	Ni	390132	76.27	39.01	129.95	0.70
	Co	108584	21.23	10.86	36.02	0.19
	Mn	55528	10.86	5.55	19.76	0.11

Table A.3 Relative peak area ratios of NCM721, NCM712, and NCM523.

Compounds	Area ratios	
	Ni^{3+}/Ni^{2+}	Mn^{3+}/Mn^{4+}
NCM721	0.6944	0.4625
NCM712	0.5974	0.4565
NCM523	0.4580	0.4559

115

APPENDIX B: Understanding of Surface Redox Behaviors of Li_2MnO_3 in Li-Ion Batteries: First-Principles Prediction and Experimental Validation

The development of rechargeable LIBs has progressed rapidly to meet the demand for consumer electronic devices such as cellular phones and laptop computers. Recently, a growing demand for large-scale energy storage applications (electric vehicle and grid electric energy storage systems) requires further performance improvement of LIBs or development of alternative energy storage technology.[2, 9, 86, 109-111] A current challenge is to increase the energy density of LIBs, which is mainly determined by the reversible capacity and operating voltage of the cathode materials. Accordingly, considerable effort has been invested in the search for advanced cathode materials with high capacities and operating voltages.

Although the bulk properties of cathode materials have been intensively studied by many research groups,[112-114] only a few studies have focused on the surface properties of cathode materials so far. Recently, several groups reported and highlighted experimental observations of the phase transformation of layered cathode materials to a spinel structure on the particle surface upon initial charging (Li^+ extraction) and subsequent transformation to a rock-salt phase after cycling.[98, 115-117] However, the initial delithiation and the origin of the phase transformations of layered cathode materials at the surface are still unclear and

controversial.

Among various cathode materials currently under development, Li-rich compounds such as xLi$_2$MnO$_3$·(1-x)LiMO$_2$ (M = Ni, Co, Mn) are regarded as the most promising candidates. Such compounds have many advantages of high capacity, low cost, and eco-friendliness.[118-120] Within the two-component composite structures, Li$_2$MnO$_3$ plays an essential role in increasing the reversible capacity of the compounds, and it independently possesses a high theoretical capacity of 460 mAh g^{-1} (if all the lithium is utilized). Although Li$_2$MnO$_3$ is not electrochemically active below 4.5 V (vs. Li/Li$^+$), Li$^+$ can be extracted from the host structure beyond 4.5 V, which is mainly responsible for reserving additional capacity.[121-122]

During the initial delithiation process, however, Li$_2$MnO$_3$ is known to transform into a layered LiMnO$_2$ structure, and subsequent cycling induces a gradual phase transformation to a spinel-like structure (LiMn$_2$O$_4$), resulting in lowering the voltage plateau and a large irreversible capacity accompanied by undesirable oxygen loss activated over the Li$^+$ removal of 1 mol.[10, 123-127] To overcome those limitations, diverse approaches have been examined to improve the electrochemical properties of the cathode materials: i) adjusting the relative ratio of different transition metal ions,[79, 128-129] ii) integrating functional coating layers on the particles,[107, 130-133] and iii) optimizing the morphology (e.g. particle size and specific surface area).[134-135] Despite all these efforts, however, no

117

fundamental solution has been found yet.

Considering the fact that the electrochemical reaction of Li_2MnO_3 may be initiated from the surface and interfaces between different phases of the cathode materials, more attention should be paid to the surface research. Such efforts would be very helpful in determining the origin of the phase transformation and, by extension, identifying the fundamental mechanism. For an exact understanding of these fundamental aspects, detailed atomic-scale theoretical studies are necessary.

In this work, the theoretical study of the delithiation potential and electronic structures of Li_2MnO_3 with the proposed surface model was helpful to demonstrate the causes of the phase transformation at the surface of the Li_2MnO_3 during the initial charge process. The theoretical modelling and experimental validation of the delithiation potential of Li_2MnO_3 were in good agreement with each other. The proposed surface model in our research is useful for further study on the fundamental problems occurring near the surface or interface between different phases of Li_2MnO_3 (Figure B.1-2). Based on our theoretical and experimental findings in this work, we conclude that surface delithiation at a low redox potential (below 4.5 V $vs.$ Li/Li$^+$) mainly happens along with the Li$^+$ pathway direction, and results from the electronic instability of Mn $3d$ electrons occupying a higher energy state at the surface of Li_2MnO_3 as compared with inner Mn atoms (Figure B.3-8 and Table B1). Therefore, the Li$^+$ positioned at the

118

surface are electrochemically activated prior to the Li^+ located in bulk, leading to gradual phase transformation (from the surface to the bulk) into a spinel-like phase. The theoretical predictions are validated by various experimental observations (Figure B.9-14). The underlying understanding of the surface of Li_2MnO_3 not only provides specific surface coatings to suppressing the propagation of the phase transformation caused from the low voltages, but also suggests a conceptual basis for developing diverse approaches (e.g. surface doping and preferential surface growth) with respect to the phase transformation of cathode materials in LIBs. We also believe that the proposed surface model can be further applied to many other related materials in various fields.
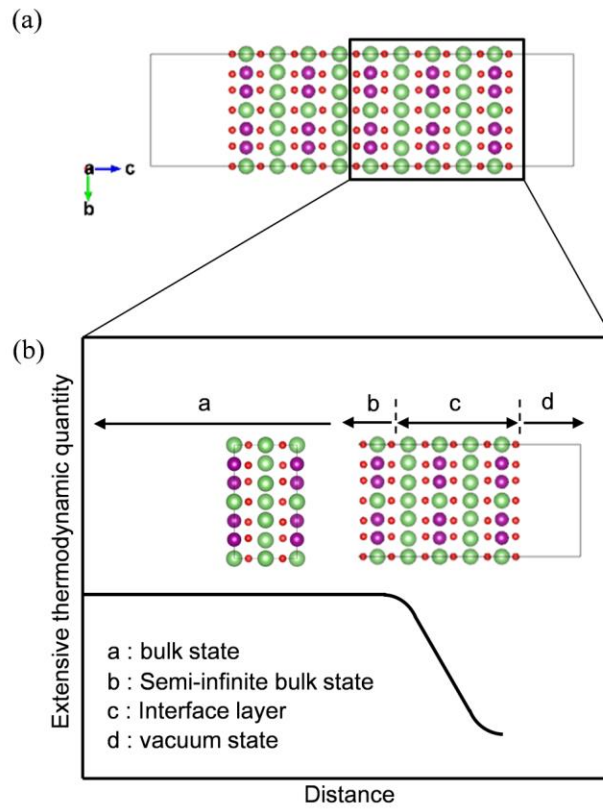
Figure B.1 A schematic of extensive thermodynamic quantities in terms of de-lithiation potential with respect to the distance across the Gibbs dividing surface. Purple, green and red spheres indicate manganese, lithium, and oxygen atoms, respectively. The interface model separates out three different regions: the semi-infinite bulk phase, vacuum as a virtual phase, and interface layers between the two phases.
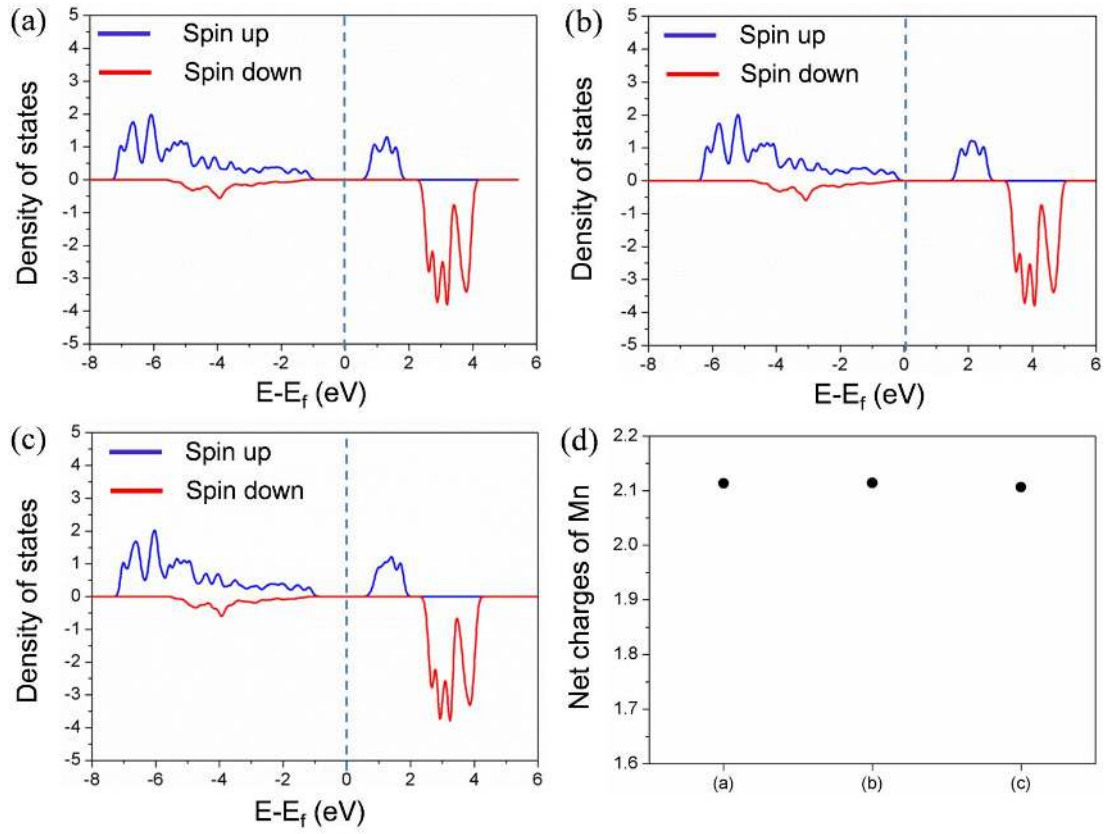
Figure B.2 $3d$-electron PDOS of Mn within the semi-infinite bulk of (a) Figure B.3a, (b) Figure B.3c and (c) Figure B.4a. (d) Net charge of Mn indicated from (a) to (c) in this Figure.
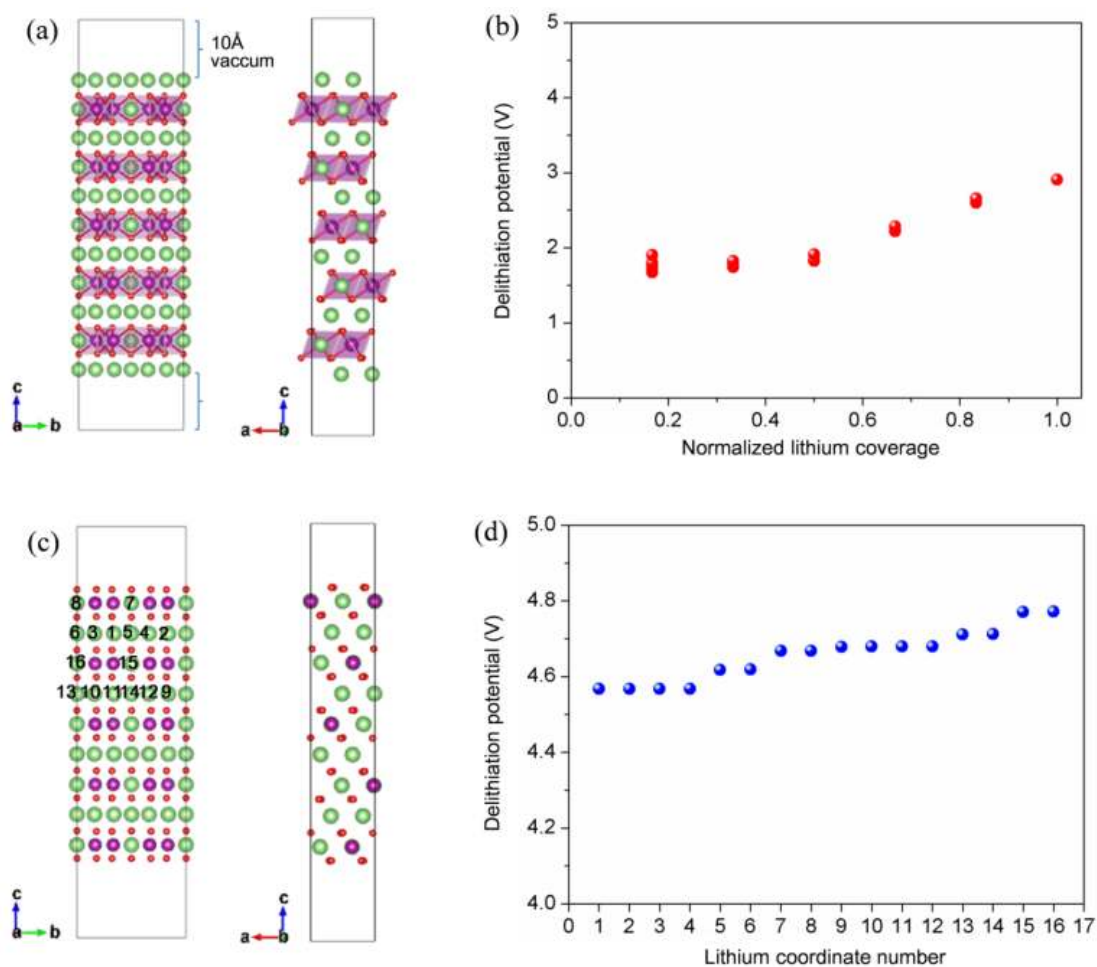
Figure B.3 (a) Li covered (001) surface model of Li_2MnO_3, and with inserted vacuum layer of 10 Å. Purple, green, and red spheres indicate manganese, lithium, and oxygen atoms, respectively. (b) Delithiation potential of covered Li as a function of normalized lithium coverage. (c) Surface model without the Li coverage, with inserted vacuum layer of 10 Å. (d) Delithiation potential with respect to lithium coordinates. The numbers of lithium coordinates are indicated.
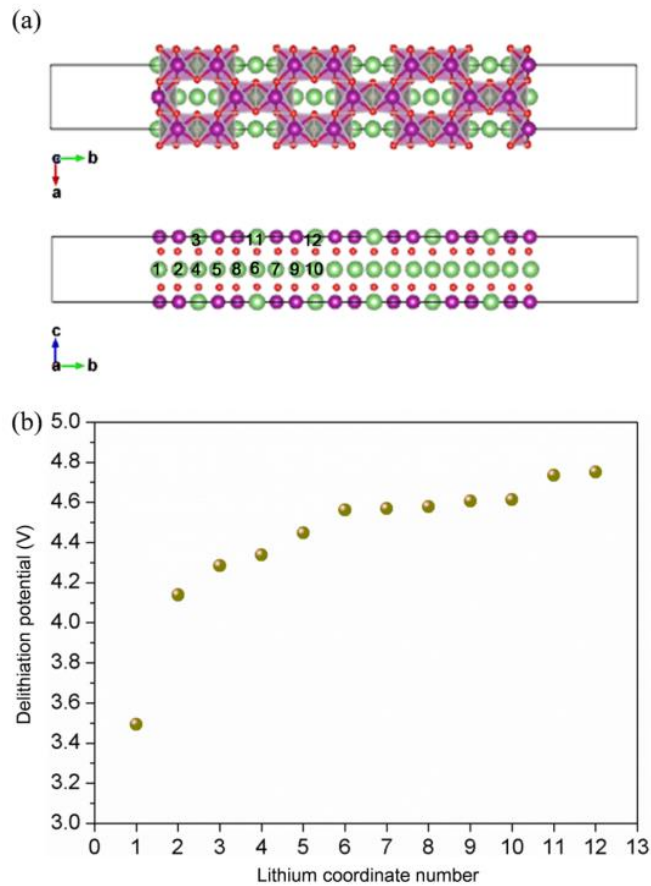
Figure B.4 (a) (020) surface model of Li_2MnO_3, with inserted vacuum layer of 10 Å. Purple, green and red spheres indicate manganese, lithium and oxygen atoms, respectively. (b) Delithiation potential as a function of lithium coordinate numbers denoted on the the green spheres in sequence.
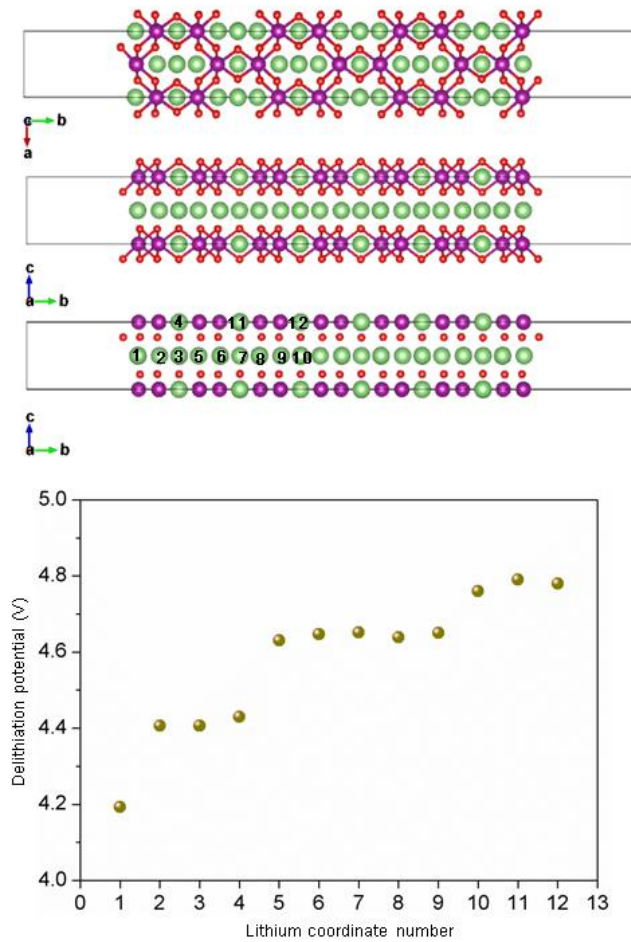
Figure B.5 Oxygen terminated (020) surface model of Li_2MnO_3, with inserted vacuum layer of 10 Å. Purple, green and red spheres indicate manganese, lithium and oxygen atoms, respectively. Delithiation potential as a function of lithium coordinate numbers denoted on the green spheres in sequence.
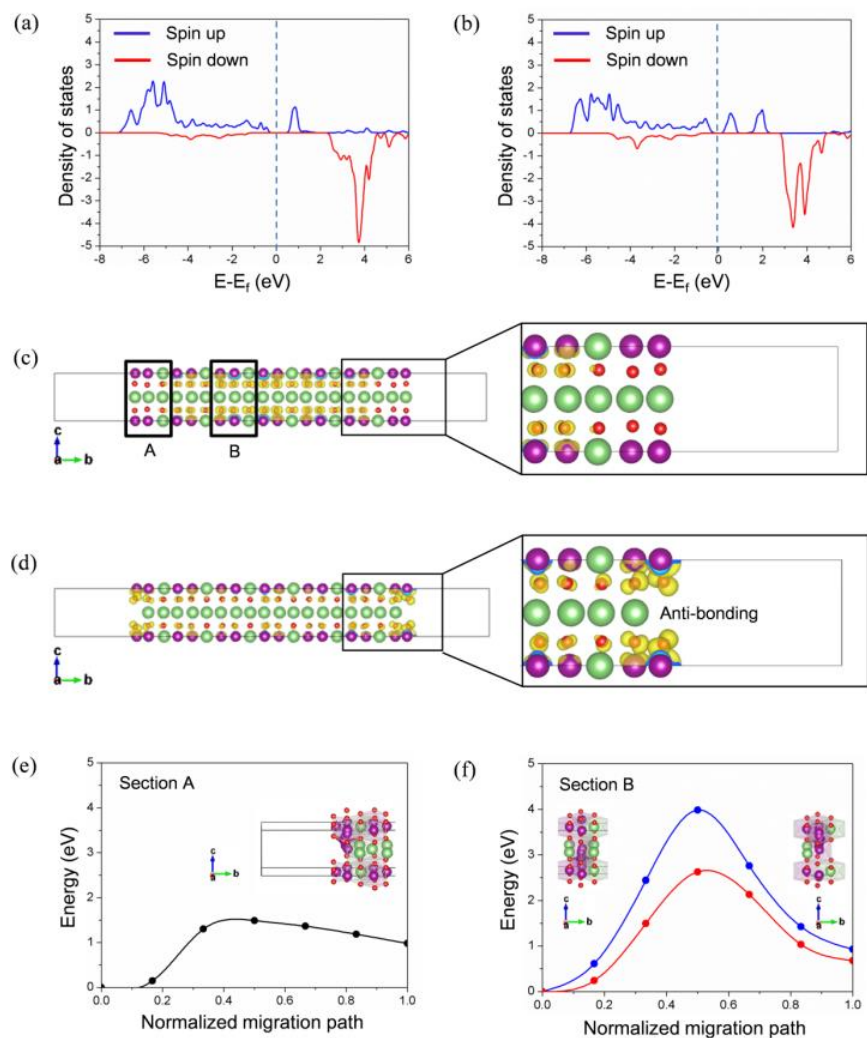
Figure B.6 (a) 3*d*-electron PDOS of Mn exposed to vacuum and (b) 3*d*-electron PDOS of inner Mn. (c) Electron distribution of the unoccupied orbitals around energy states (≈2 eV) and (d) At the same energy level as (c), electron distribution of the orbitals created by the lithium removal. Migration energy barriers for Mn in (e) the surface region described as section A, (f) the bulk region described as section B.

서울대학교
SEOUL NATIONAL UNIVERSITY
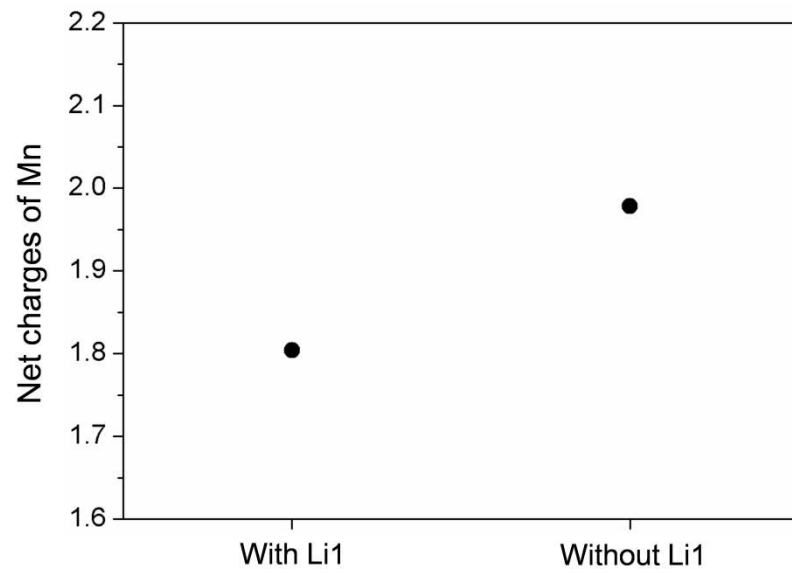
Figure B.7 Net charge of the outermost Mn before and after Li1 (Figure B.4a) removal in the (020) surface model.

서울대학교
SEOUL NATIONAL UNIVERSITY
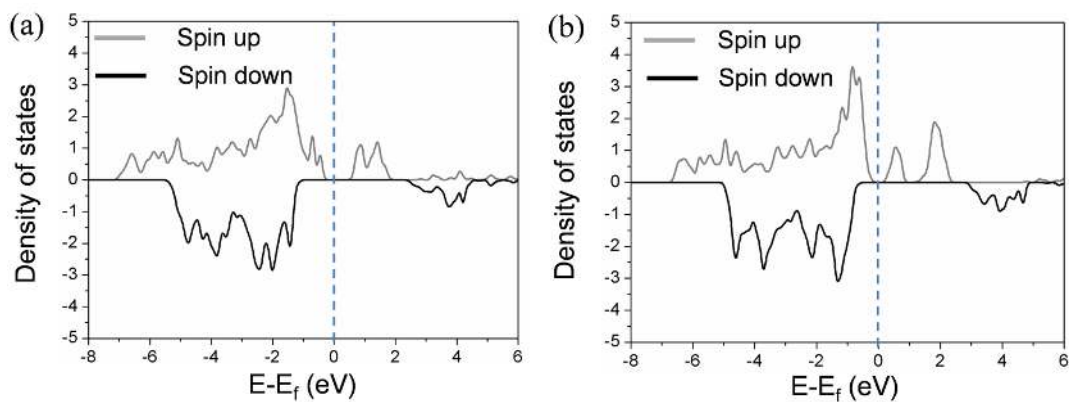
Figure B.8 (a) 2*p*-electron PDOS of O connected with the outermost Mn in the (020) surface model before Li1 removal, and (b) after Li1 removal.
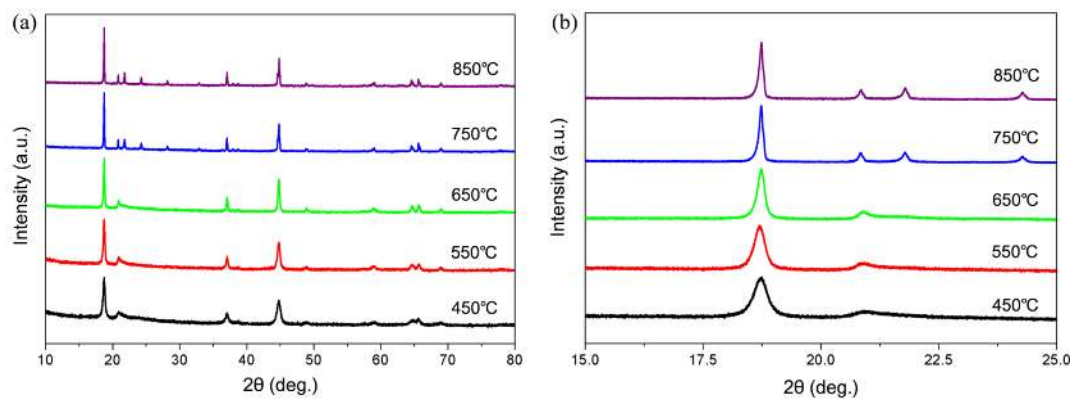
Figure B.9 (a) XRD patterns of the Li_2MnO_3 synthesized at $450 - 850$ °C and (b) detailed XRD patterns of Li_2MnO_3 at $2\theta = 15 - 25$ ° from (a).
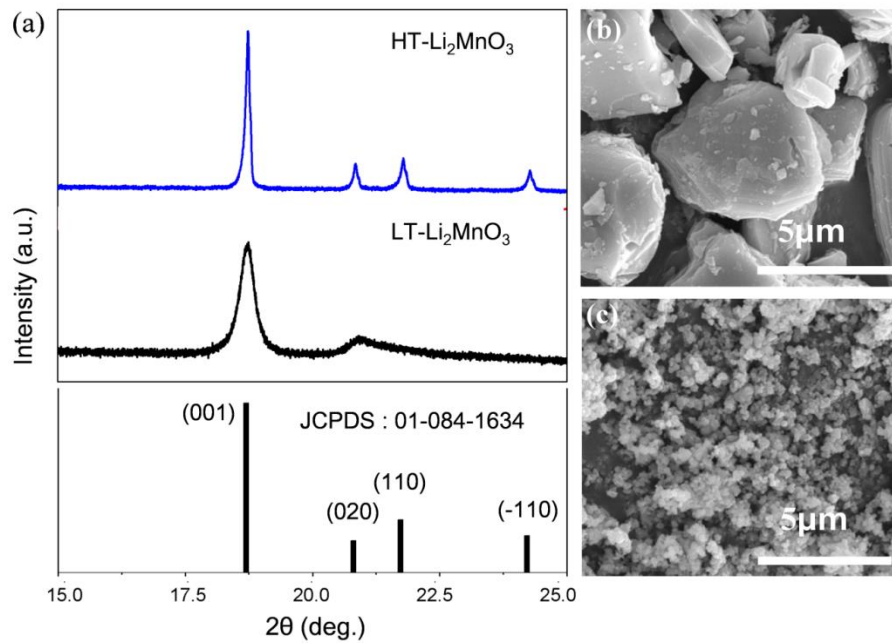
Figure B.10 (a) Detailed powder XRD patterns of HT-Li$_2$MnO$_3$ and LT-Li$_2$MnO$_3$ synthesized at 850 and 450 °C, respectively. Corresponding FESEM images of (b) HT-Li$_2$MnO$_3$ and (c) LT-Li$_2$MnO$_3$ particles.
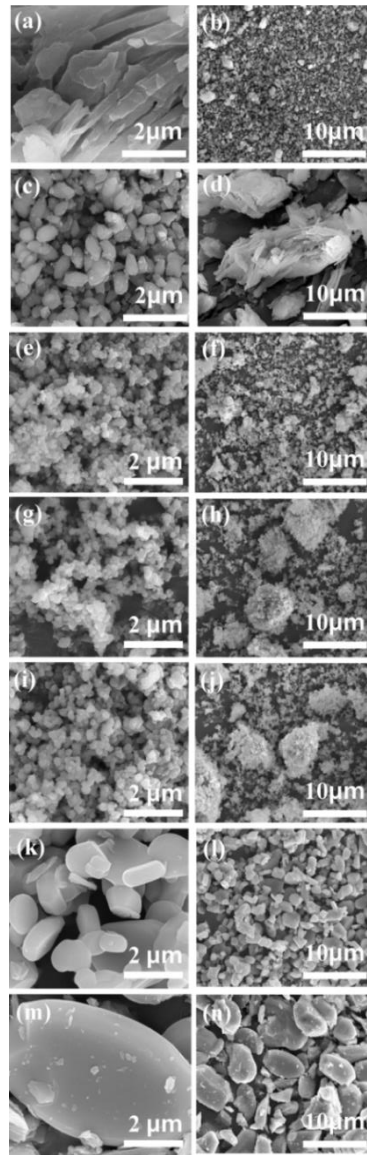
Figure B.11 High magnification (left) and low magnification (right) field-emission scanning electron microscope (FESEM) images of (a,b) LiOH and (c,d) $MnCO_3$ precursors. Pristine Li_2MnO_3 particles synthesized at different temperatures: (e,f) 450 °C, (g,h) 550 °C, (i,j) 650 °C, (k,l) 750 °C, and (m,n) 850 °C.
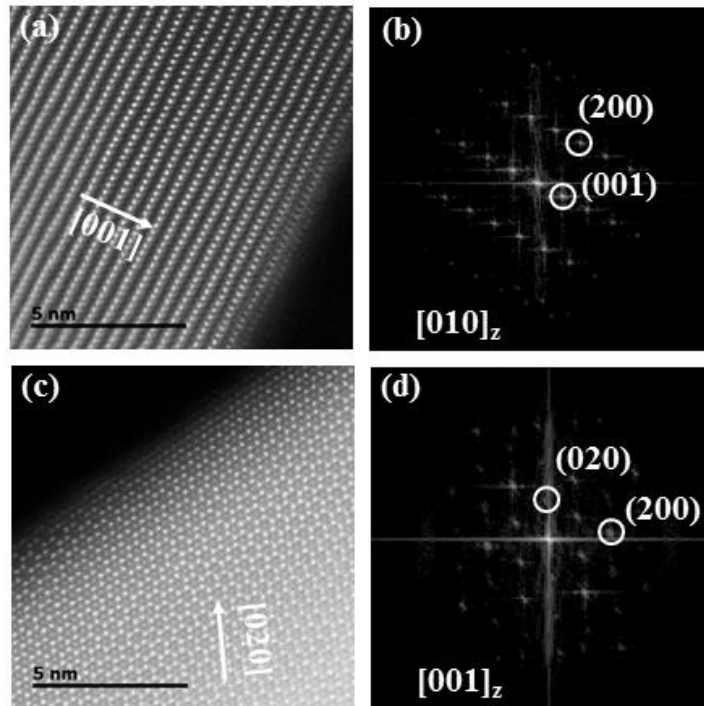
Figure B.12 (a) (001) surface of dark-field STEM image of HT-Li$_2$MnO$_3$ synthesized at 850 °C, pictured near the surface on a 5 nm scale. The white arrow indicates the stacking orientation along with the [001] direction around the surface region. (b) FFT results showing the monoclinic Li$_2$MnO$_3$ structure (space group : C2/m, [010]$_z$ direction). (c) (020) surface of dark-field STEM image of HT-Li$_2$MnO$_3$ synthesized at 850 °C, pictured near the surface on a 5 nm scale. (d) FFT results showing the monoclinic Li$_2$MnO$_3$ structure (space group : C2/m, [001]$_z$ direction).
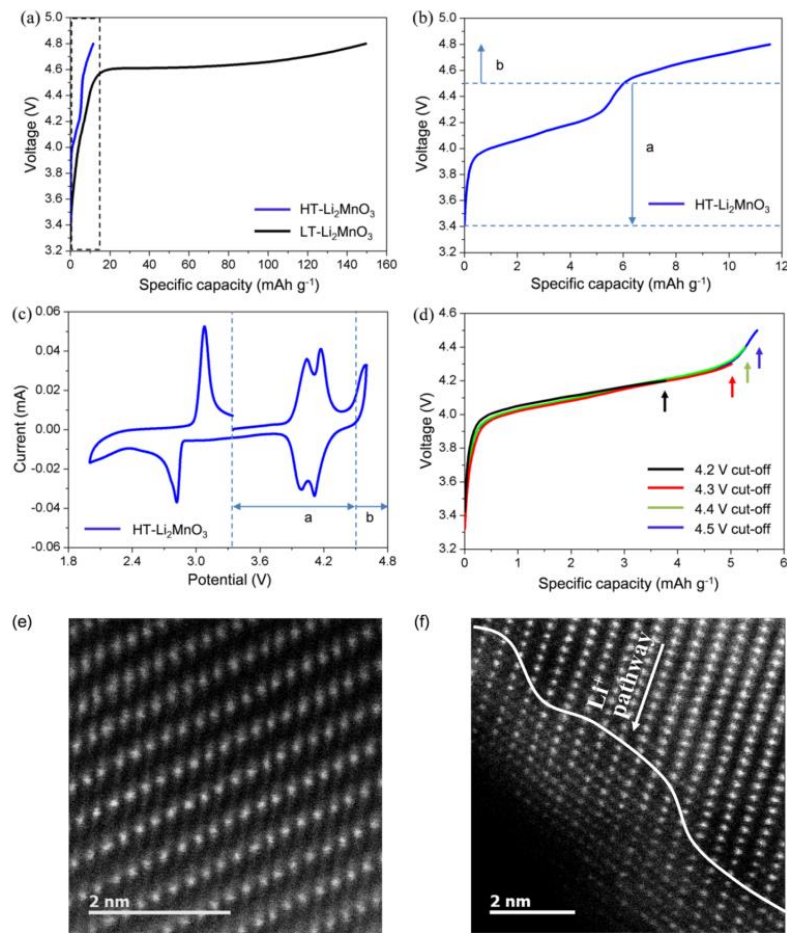
Figure B.13 (a) Galvanostatic initial charge profiles of HT-Li$_2$MnO$_3$ (blue line) and LT-Li$_2$MnO$_3$ (black line) recorded with a constant current density of 0.05 C (383 mAg^{-1}) in a voltage ranging from OCV to 4.8 V *vs.* Li/Li$^+$. (b) Detailed initial charge profile of HT-Li$_2$MnO$_3$ with a distinctive plateau below 4.5 V *vs.* Li/Li$^+$. (c) Cyclic voltammogram of HT-Li$_2$MnO$_3$ with a scan rate of 0.1 mVs^{-1} in the same voltage region. (d) Comparision of galvanostatic charge profiles of HT-Li$_2$MnO$_3$ with cut-off voltages of 4.2, 4.3, 4.4, and 4.5 V *vs.* Li/Li$^+$. STEM images of HT-Li$_2$MnO$_3$ after the first charge with cut-off voltage 4.5 V *vs.* Li/Li$^+$, showing (e) the bulk and (f) surface.
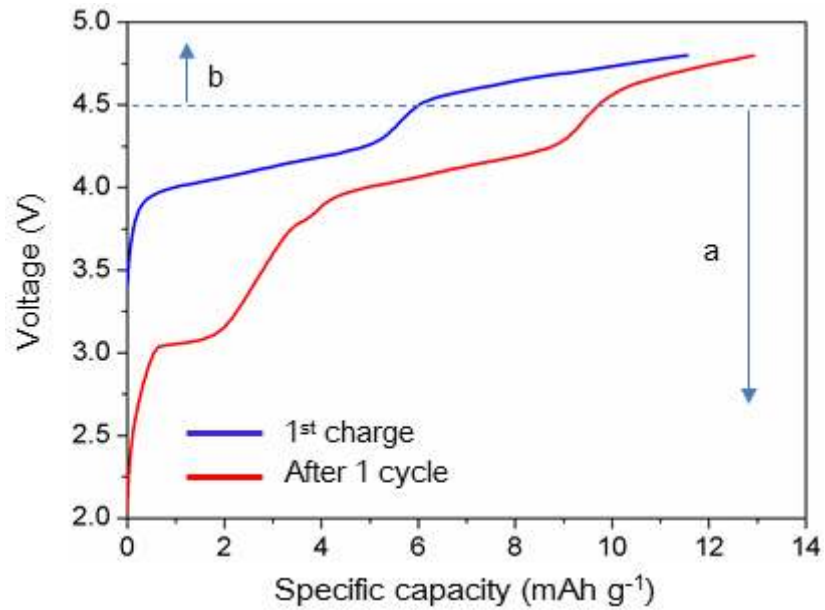
Figure B.14 The first charge (blue line) and after 1cycle (red line) curves of HT-Li$_2$MnO$_3$ with a constant current density of 0.05C in a voltage range from 2 V to 4.8 V *vs.* Li/Li$^+$. The region a and b indicate surface reactions and suppressed bulk reactions with electrolyte decompositions.

Table B.1 Comparison of surface energies of the (020) surface of Li_2MnO_3. Li-layer and Mixed layer refer to the exposure to the vacuum of the Li-layer and the mixed layer, respectively (Mixed 2 layers: A case of the two mixed layers exposure).

	Li-layer	Mixed 1 layer	Mixed 2 layers
Surface energy (eV/ Å^2)	-0.0535	-0.2372	-0.5139

APPENDIX C: Phase Separation and *d* Electronic Orbitals on Cyclic Degradation in Li-Mn-O Compounds: First-Principles Multiscale Modeling and Experimental Observations

LIBs have been considered as solutions for various energy demands ranging from portable electronic devices to large-scale energy storage applications (e.g., electric vehicles (EVs) and energy storage systems (ESSs)).[2, 9] To meet these requirements, Mn spinel $LiMn_2O_4$ has been studied extensively as an alternative cathode material to currently commercialized layered oxides because of its advantages, such as high power, low cost, and eco-friendliness.[110, 136-138] However, cubic spinel $LiMn_2O_4$ experiences capacity degradation for the following reasons: i) Jahn-Teller distortion derived from Mn^{3+} in the pristine structure,[112, 139] and ii) Mn^{2+} dissolution in the acidic electrolyte.[140] To resolve these problems, several research groups have reported the improved electrochemical performance of $LiMn_{2-x}Al_xO_4$ compared to $LiMn_2O_4$.[141-142] They claimed that the enhanced performance of LMAO is mainly attributed to the suppression of the Jahn-Teller distortion. Although direct evidence of the Jahn-Teller distortion and the suppressed effect have been obtained through diverse experiments,[17, 143] the detailed theoretical origins and mechanism on the suppression of the Jahn-Teller distortion have not been understood yet. Furthermore, it is unclear that this Jahn-

Teller distortion generated on the atomic scale affects the particle-level phase transformation and the cyclic degradation. Therefore, multiscale approaches bridging the atomic scale phenomena to mesoscale behaviors are needed to understand the experimental phenomena and overcome the limitations of the atomic scale analyses.[10-11, 38, 48, 53, 82, 144]

In this work, experimental observations and multiscale modeling were performed to obtain a fundamental understanding of the suppression of the Jahn-Teller distortion (e.g., Mn^{3+}) by Al doping. The electrochemical properties of as-synthesized LMO showed a decreasing capacity after cycling, while the cycle performance of LMAO was retained during cycling (Figure C.1,3,5 and Table C.1). To examine the origins and mechanism of electrochemically improved properties, the electronic structures of Mn and O ions were calculated using first-principles (Figure C.2,4,6-7 and Table C.2). The electronic structure of LMO revealed an anisotropic behavior induced by the Jahn-Teller distortion from Mn^{3+}. In contrast, the electronic structure of LMAO exhibited an isotropic shape, suggesting that the stable electronic structure would positively affect the electrochemical performances during cycling. Based on this mechanistic understanding, the multiscale phase separation kinetics showed that the phase separation of $L_{0.828}MO$ to $L_{0.625}MO$ and L_0MO causes an irreversible phase transformation to the inactive $Li_0Mn_2O_4$ phase; in contrast, LMAO has a stable ground state at $x = 0.625$ ($L_{0.375}MAO$), which would prevent the transformation to the inactive phase (Figure C.8-10). Finally, these findings provide an essential

understanding of the cyclic performance closely related to the Jahn-Teller distortion of both the LMO and LMAO. In addition to the isotropic electronic structures are expected to provide a solution to overcome the drawbacks of the Jahn-Teller distortion in the atomic scale, mesoscale phase separation behaviors could help to predict and improve the cyclic performances in newly designed cathode materials for LIBs.
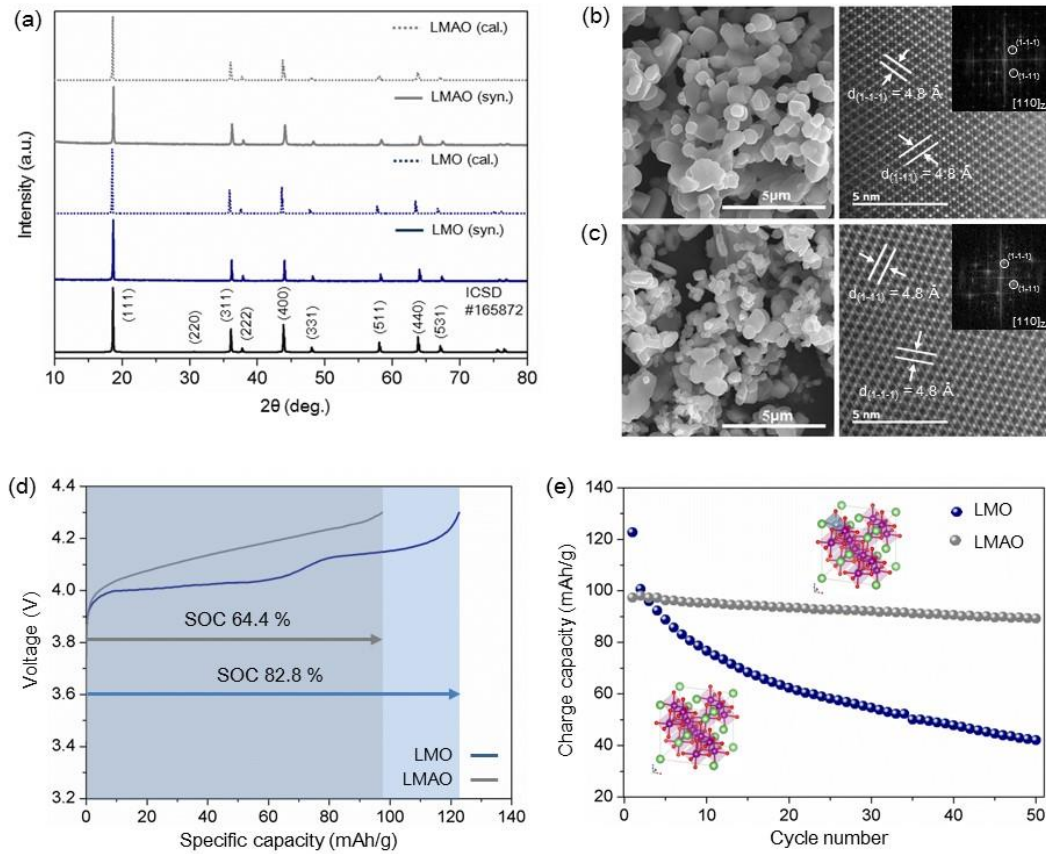
Figure C.1 (a) XRD patterns of the synthesized and calculated LMO and LMAO. FESEM and STEM images of (b) LMO and (c) LMAO particles with *d*-spacings based on the corresponding fast Fourier transformation (FFT) images with a zone axis of [110]. (d) Galvanostatic charge profiles at the first cycle and (e) cyclic performances of LMO (blue line and circles) and LMAO (gray line and circles) in the voltage range, 3.0 V to 4.3 V *vs.* Li/Li+, with a constant current of 0.1 C.
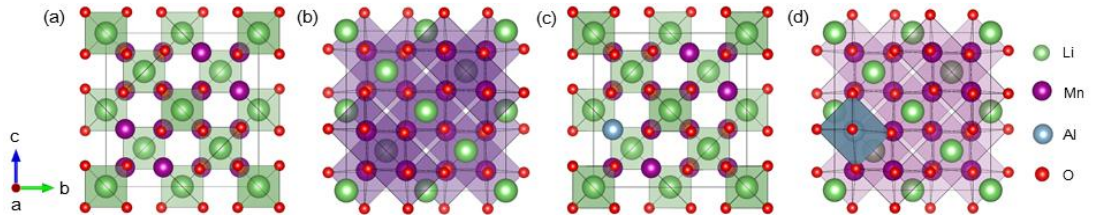
Figure C.2 (a) Tetrahedron of LiO_4 and (b) octahedron of MnO_6 in the atomic model of LMO. (c) LiO_4 and (d) the MnO_6 and AlO_6 in the atomic model of LMAO.
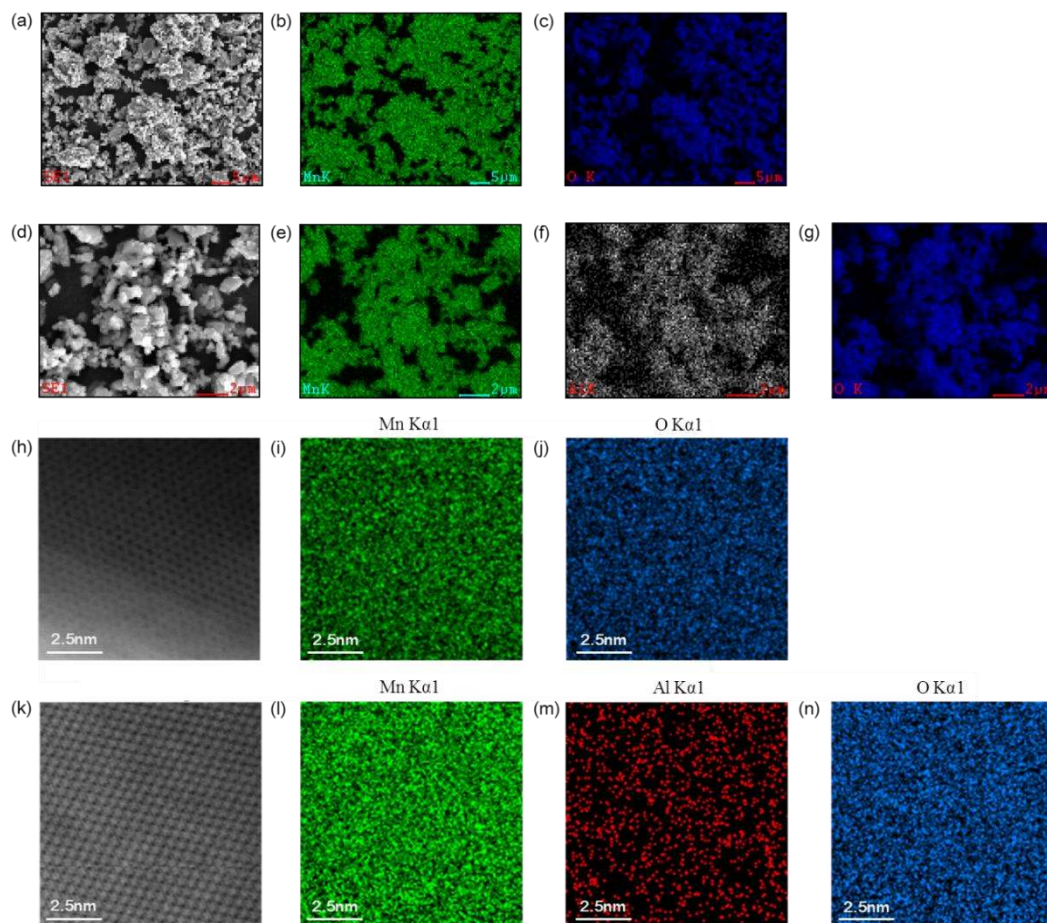
Figure C.3 FESEM images of (a) LMO and (d) LMAO, corresponding EDS elemental mapping of (b and e) Mn (green), (f) Al (gray), and (c and g) O (blue). STEM images of (h) LMO and (k) LMAO with EDS elemental mapping of (i and l) Mn (green), (m) Al (red), and (j and n) O (blue).
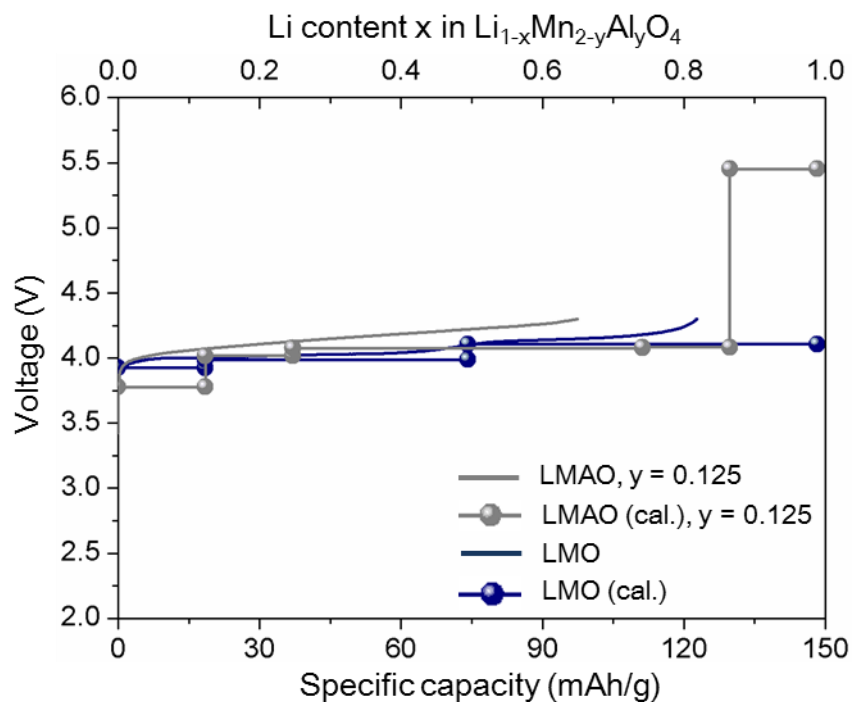
Figure C.4 Experimentally evaluated profiles at the first charge and the calculated delithiation potentials of LMO and LMAO with the removal of Li⁺.
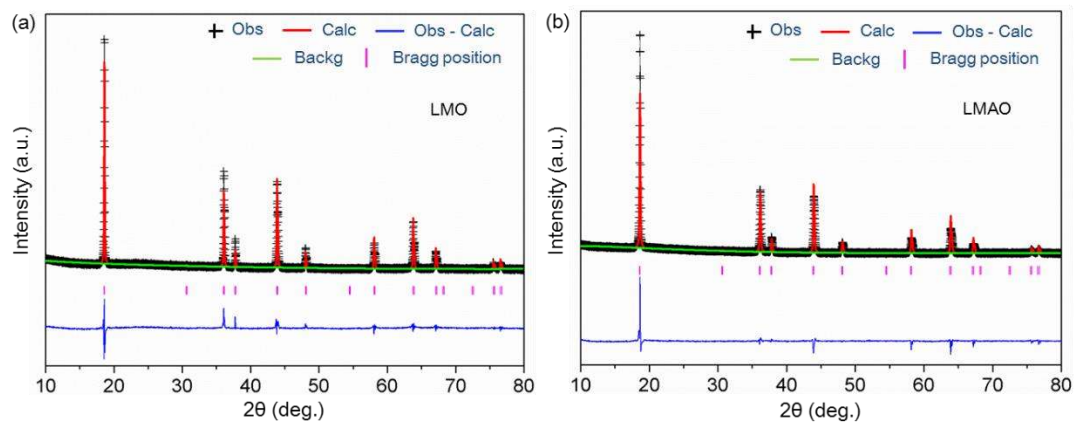
Figure C.5 Rietveld refinement data from X-ray diffraction patterns of (a) LMO and (b) LMAO.
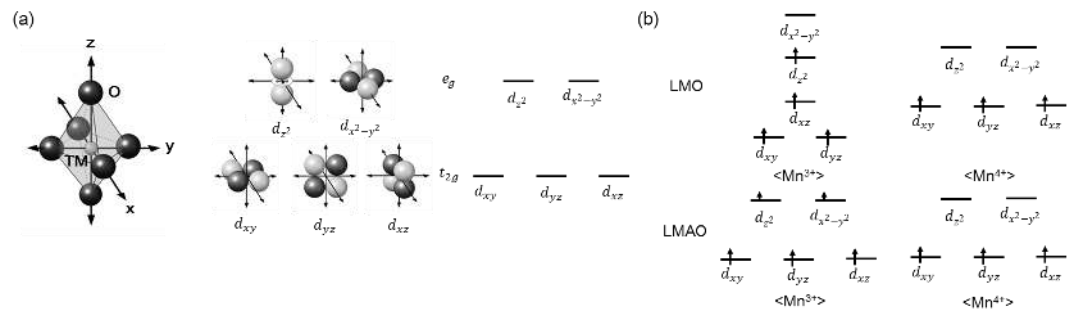
Figure C.6 (a) Regular octahedral 6 coordination geometries of a transition metal (TM) with oxygen atoms (TMO$_6$) and d orbitals of a TM positioned in an octahedral site and the corresponding schematic energy levels known as the e_g band and t_{2g} band within the $3d$ bands. (b) Schematic energy levels and occupied electron configurations of the $3d$ bands from the Mn ions in LMO and LMAO.
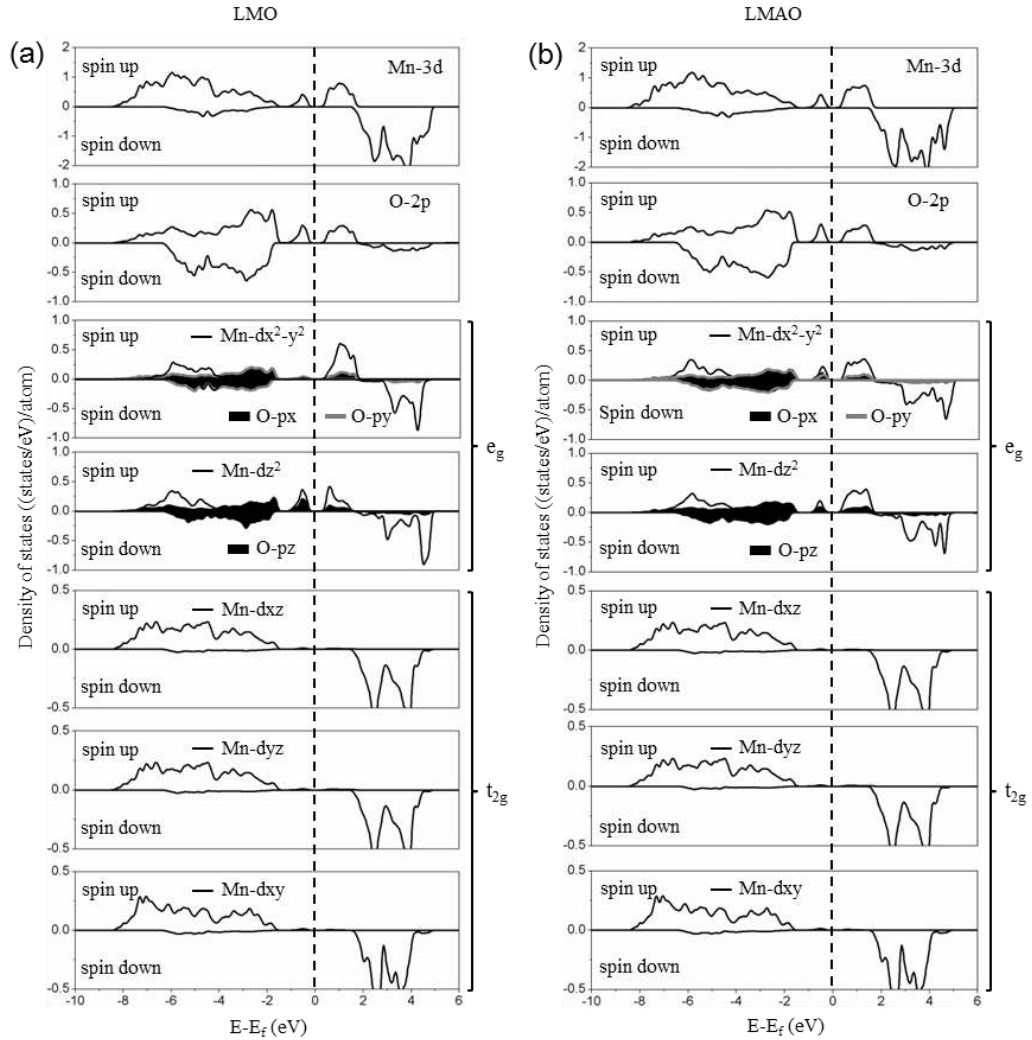
Figure C.7 $3d$-electron PDOS of Mn and $2p$-electron PDOS of O. Corresponding PDOS of the 3 degeneracies of d_{xy}, d_{yz}, d_{xz} in the t_{2g} band and 2 degeneracies of the d_z^2, $d_x^2{}_{-y}^2$ in the e_g band with respect to Mn ions, and similarly, 3 degeneracies of p_x, p_y and p_z with respect to O ions in (a) LMO and (b) LMAO.
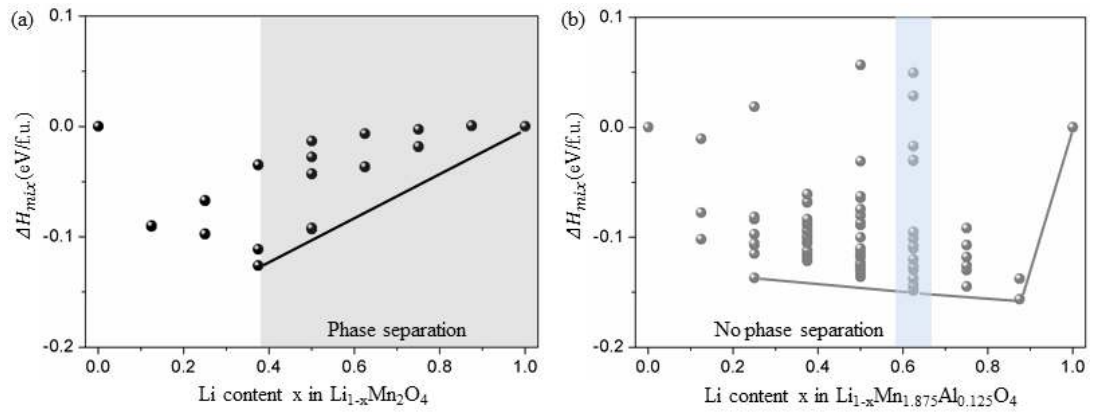
Figure C.8 Zero-temperature mixing enthalpy calculated from first-principles calculations in (a) $L_{1-x}MO$ (black circles) and (b) $L_{1-x}MAO$ (gray circles) from x =0 to 1.
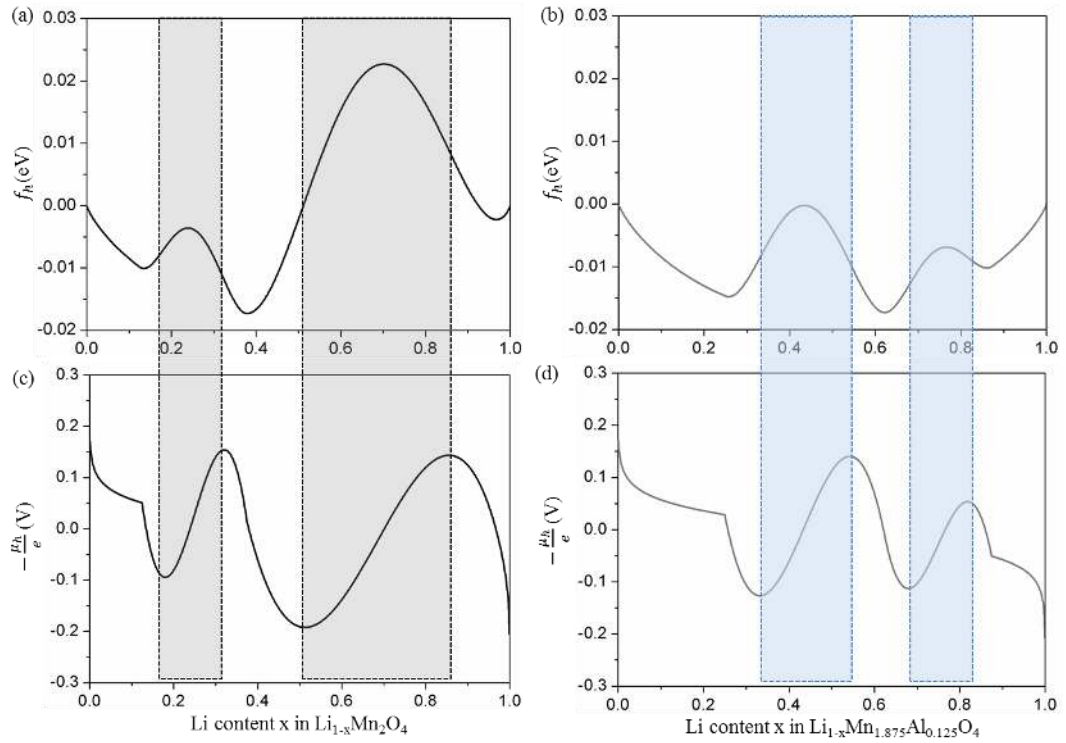
Figure C.9 Homogeneous bulk free energy, f_h, of (a) LMO and (b) LMAO, and the chemical potential, $-\mu_h/e$, of (c) LMO and (d) LMAO at room temperature with respect to the inverse Li content x. The black dashed lines in (a) and (c) are the spinodal points of LMO and the blue dashed lines in (b) and (d) are the spinodal points of LMAO.
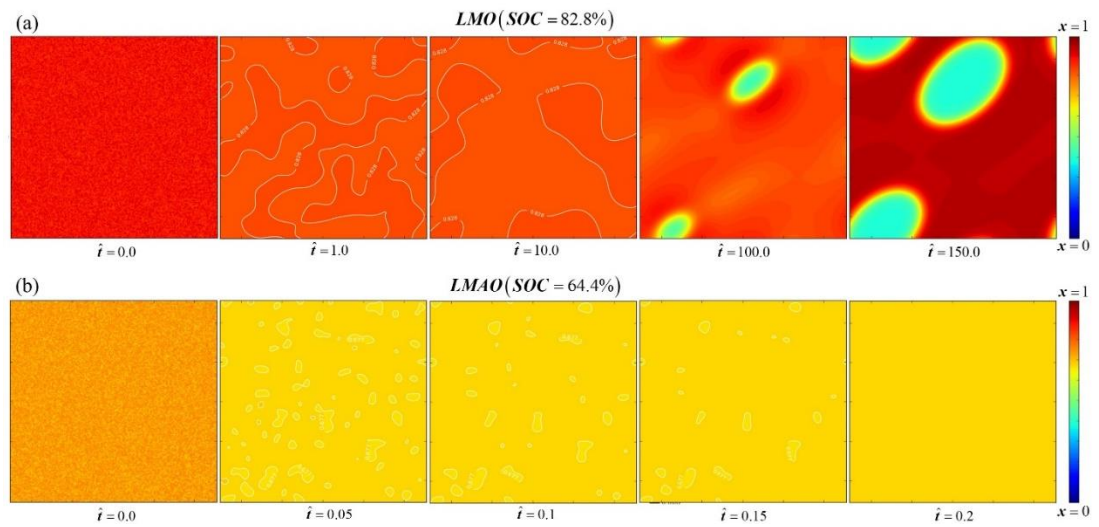
Figure C.10 Phase separation kinetics in (a) LMO (SOC = 82.8%) and (b) LMAO (SOC=64.4%) during relaxation from a solid solution at various dimensionless time $\hat{t}$.

Table C.1 Calculated lattice parameters and Rietveld refinement results of the lattice parameters in LMO and LMAO.

Compounds	a-cal. (Å)	a-exp. (Å)	Rp (%)	Rwp (%)
LMO	8.289	8.244	2.537	4.087
LMAO	8.256	8.232	2.422	4.514

Table C.2 Integration of the entire energy states (Total) and the occupied states (Valence) from the indicated PDOS in Figure C.7. The fractional band fillings from each band were calculated through the total and valence.

Compounds		Mn d orbitals					O p orbitals		
		dxy	dyz	dxz	dz^2	dx^2-y^2	px	py	pz
LMO	Total	1.909	1.897	1.897	1.973	1.995	1.360	1.360	1.360
	Valence	1.044	1.031	1.031	0.955	0.746	1.169	1.169	1.198
	Fractional band filling	0.547	0.543	0.543	0.484	0.374	0.859	0.859	0.880
LMAO	Total	1.863	1.864	1.864	1.945	1.946	1.328	1.328	1.328
	Valence	1.014	1.016	1.015	0.814	0.851	1.159	1.159	1.155
	Fractional band filling	0.545	0.545	0.545	0.419	0.438	0.872	0.873	0.870

APPENDIX D: Hexacyanometallates for Sodium-Ion Batteries: Insights into Higher Redox Potentials Using *d* Electronic Spin Configurations

SIBs have been widely studied as a next-generation rechargeable battery system, which may overcome potential problems (such as reserves and rising price of lithium sources) for LIBs.[5, 30, 145-149] Many researchers have focused on sodium layered oxides (i.e., NaTMO$_2$) as cathodes because not only they have shown similar oxidation states of each element, but also been prepared using comparable synthesizing methods as compared with lithium layered oxides (i.e., LiTMO$_2$).[32, 54, 150-152] Among NaTMO$_2$ compounds, layered oxides containing Ni as a major redox center have intensively researched to obtain high capacity and cyclic performance.[26, 33, 153-154] Although Ni-based sodium layered oxides have indicated good electrochemical performance, great efforts have been devoted to decrease content of this expensive Ni with relatively cheaper elements (e.g., Fe, Mn, etc.).[7, 31, 143, 155-158]

Recently, Wang and co-workers have reported rhombohedral sodium hexacynoferrates (Na$_2$Fe$_2$(CN)$_6$) as a potential cathode material for high gravimetric energy density with two distinct redox behaviours: ~3.11 V vs. Na/Na$^+$ at the first plateau and ~3.30 V vs. Na/Na+ at the second plateau. Using Mn as another earth-abundant element, Na$_2$FeMn(CN)$_6$ has been discovered as a

more promising cathode material with higher gravimetric energy density due to higher redox potential (~ 3.5 V vs. Na/Na$^+$) than $Na_2Fe_2(CN)_6$.[159] Moreover, from the perspective of industry, Fe and Mn as cheap redox elements are not only enabled SIB systems without the expensive elements, but also the hexacyanoferrates are fabricated with an easy accessibility at room temperature.[20] In the hexacynoferrate, the cyan group (-CN) as anions are well ordered to form an octahedron of FeC_6 and an octahedron of FeN_6.[20, 37, 160] Even though TMs in Na (or Li) TMO_2 compounds present one type of electronic spin configuration in TMO_6 octahedron, there are two types of spin configurations in terms of TMs in sodium hexacyanometallates due to the different atomic coordination with the -CN group.[20, 82, 161-162] Although studies of improving battery performance have been extensively performed and analysed on structural changes in $Na_2FeMn(CN)_6$ during the desodiation process,[13] an in-depth theoretical understanding based on crystal field theory with spin configurations for hexacyanometallates has not yet been investigated. Therefore, the fundamental correlation between electrochemical behaviours and d electronic structures, similar to our previously reported work on LIB,[54, 82] should be clarified to control the intrinsic properties of materials with enhanced performance or design new materials for SIB. Specifically, different spin configurations would not only affect structural parameters in hexacyanometallates compounds, it is but also expected that the electrochemical performance (especially redox potentials) of hexacyanometallates could be directly affected by high or low spin-states considering crystal field

151

splitting (CFS) of TMs.

In this work, the theoretical calculations considering d electronic spin configurations of TMs were carried out not only to develop a deep understanding on thermodynamic behaviors with structural changes, but also to predict higher redox potentials in hexacyanometallates, with subsequent validation by XPS analysis and electrochemical measurements of synthesized samples. Through the calculations of mixing enthalpy of all possible configurations of Fe and Mn atoms, the crystal structure with $x = 1$ in $Na_2Fe_{2-x}Mn_x(CN)_6$ was found to be the most stable phase (Figure D.1-2). The lattice parameters increase as the Mn content increased from $x = 0$ to $x = 1$, and this increase is caused by the larger ionic radius of Mn^{2+} at high-spin state (Figure D.3). More specifically, all mixed Fe^{2+} and Mn^{2+} of $Na_2FeMn(CN)_6$ are coordinated by 6C and 6N in octahedral site, respectively, indicating that their electronic structures are the low-spin state and the high-spin state as carefully confirmed by PDOS from first-principles calculations (Figure D.4). Considering CFT of TMs, these electronic structures represent the most stable configuration with the specific spin configurations, leading to higher redox potentials as compared with Fe^{2+} in $Na_2Fe_2(CN)_6$ (Figure D.5-9). These theoretical predictions and detailed investigations are validated by experiments (Figure D.10-12 and Table D.1), and provide insights with a design concept using the electronic spin configuration (i.e., high- and low-spin states) of TMs toward higher redox potentials to realize electrochemically better performance in hexacyanometallates. We also believe that our findings from the

152

theoretical calculations and experimental observations will not only be helpful in understanding the fundamental correlation between redox potentials and electronic structure stability depending on spin states, but also be applied to many intercalation compounds for rechargeable battery applications.
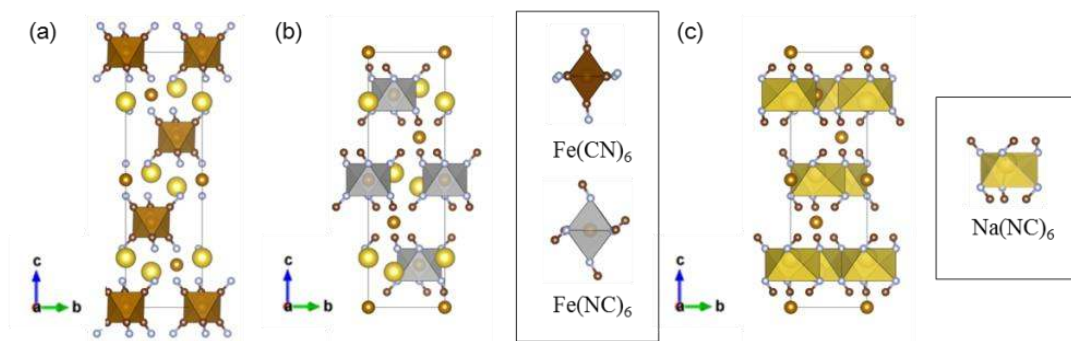
Figure D.1 The atomic model of $Na_2Fe_2(CN)_6$ with highlighted octahedra (a) $Fe(CN)_6$ as brown octahedra, (b) $Fe(NC)_6$ as light gray octahedra, and (c) $Na(NC)_6$ as yellow octahedra.
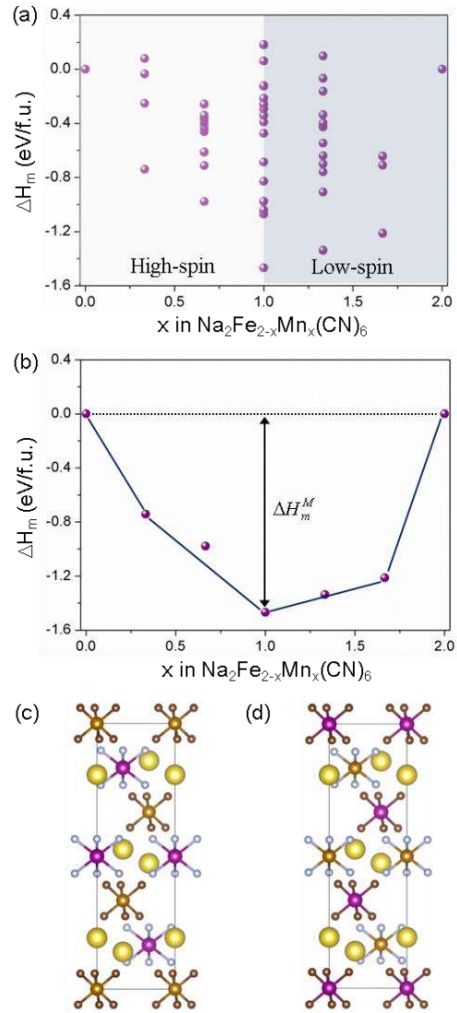
Figure D.2 (a) The mixing enthalpies calculated from $x = 0$ to 2 in $Na_2Fe_{2-x}Mn_x(CN)_6$ with all possible atomic configurations of Fe/Mn. (b) The ground states with respect to Mn ratios from corresponding mixing enthalpies. (c) The atomic model from lowest mixing enthalpy and (d) the atomic model from highest mixing enthalpy. Coloring is as: Yellow sphere are Na; brown sphere are Fe; purple sphere are Mn; dark brown sphere are C; light blue sphere are N.

155
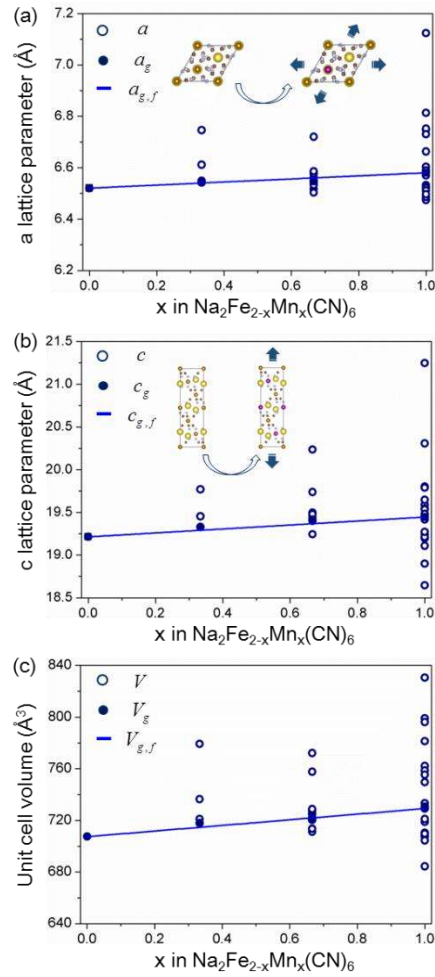
Figure D.3 (a) *a* lattice parameter, (b) c lattice parameter, and (c) unit cell volume (V) as a function of Mn content from $x = 0$ to $x = 1$ in $Na_2Fe_{2-x}Mn_x(CN)_6$. The navy open circles and filled circles are structural parameters (i.g., a, c, and V) based on all possible atomic configurations and those at ground states (i.e., a_g, c_g, and V_g) from Figure D.2a. The blue line shows the fitted structural parameters (i.e., $a_{g,f}$, $c_{g,f}$, and $V_{g,f}$) governed by Vegard's law.

156
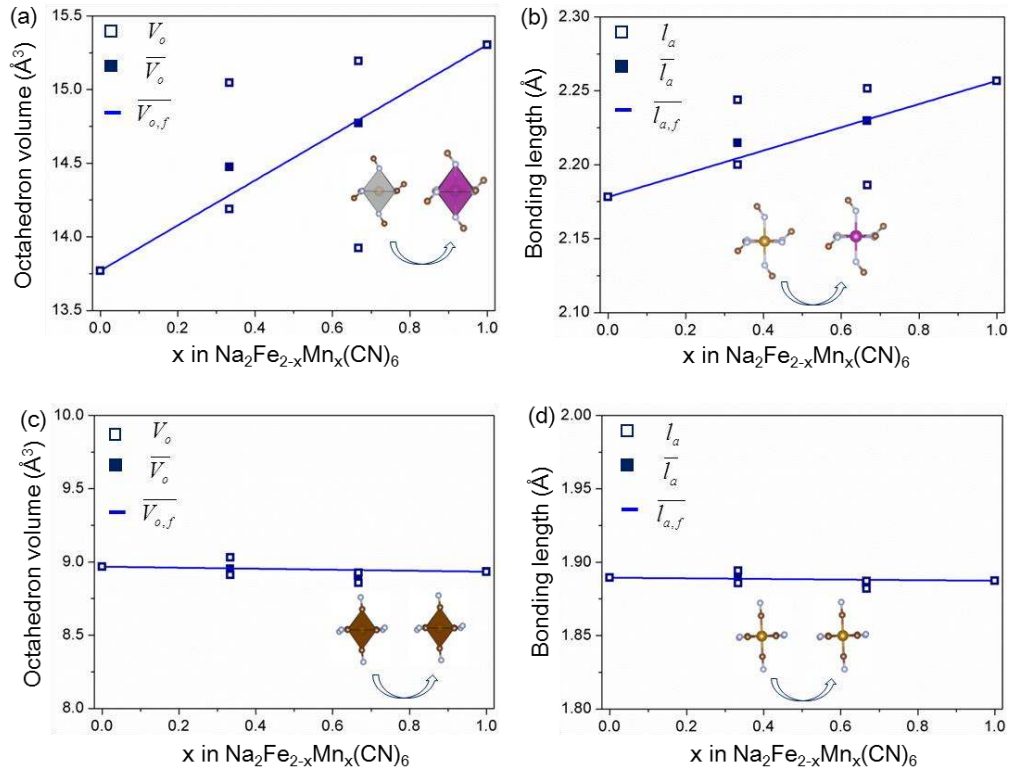
Figure D.4 (a, c) octahedron volumes (V_o) and averaged bonding lengths (l_a)
connected with 6N, and (b, d) those connected with 6C as a function of Mn
content from $x = 0$ to $x = 1$ in $Na_2Fe_{2-x}Mn_x(CN)_6$. The navy open squares and
filled circles are octahedral structure parameters (i.g., V_o, $\overline{V_o}$, l_a, $\overline{l_a}$) based on
the minimum energy phases from Figure D.2a. The blue line shows the fitted
octahedral structure parameters (i.g., $\overline{V_{o,f}}$, $\overline{l_{a,f}}$) governed by Vegard's law.

157
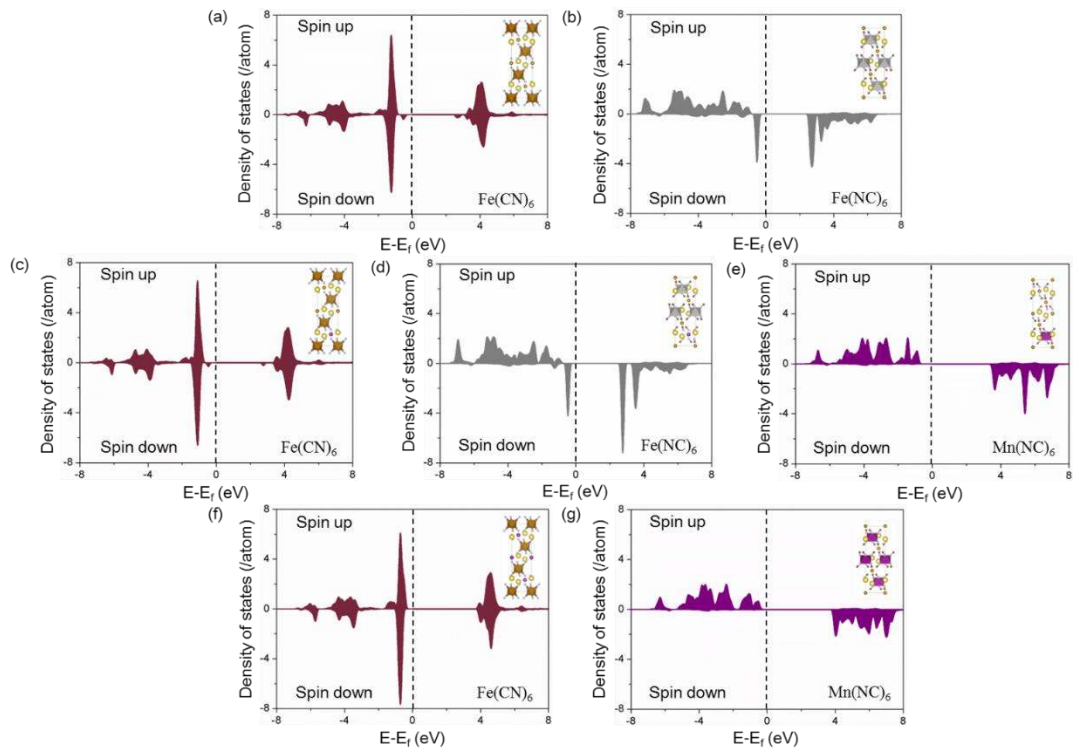
Figure D.5 The projected partial density of states (PDOS) of $3d$ electrons based on the ground phases from Fig. 2b: (a) Fe in $Fe(CN)_6$ and (b) Fe in $Fe(NC)_6$ in $Na_2Fe_2(CN)_6$; (c) Fe in $Fe(CN)_6$, (d) Fe in $Fe(NC)_6$, and (e) $Mn(NC)_6$ in $Na_2Fe_{1.667}Mn_{0.333}(CN)_6$; (f) Fe in $Fe(CN)_6$ and (g) Mn in $Mn(NC)_6$ in $Na_2FeMn(CN)_6$.
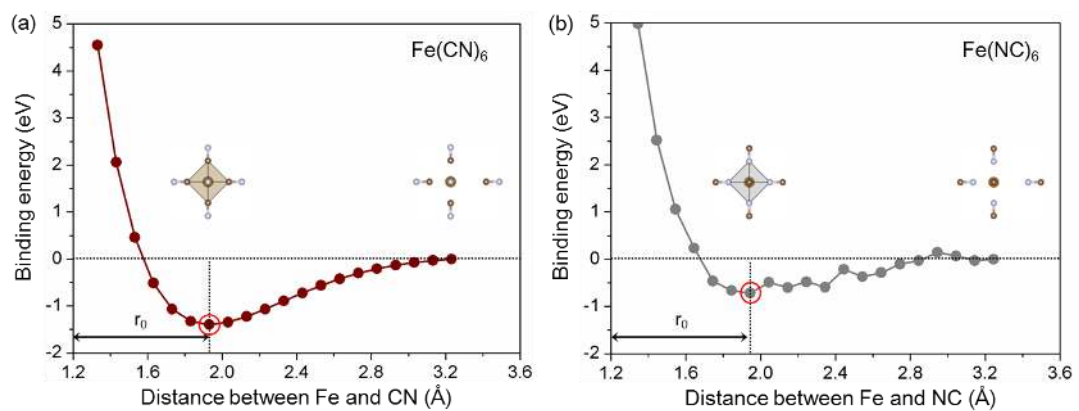
Figure D.6 Binding energy curves as a function of distance between Fe and (a) CN and (b) NC. r_0 refers to the distance at equilibrium state indicated as red circle.
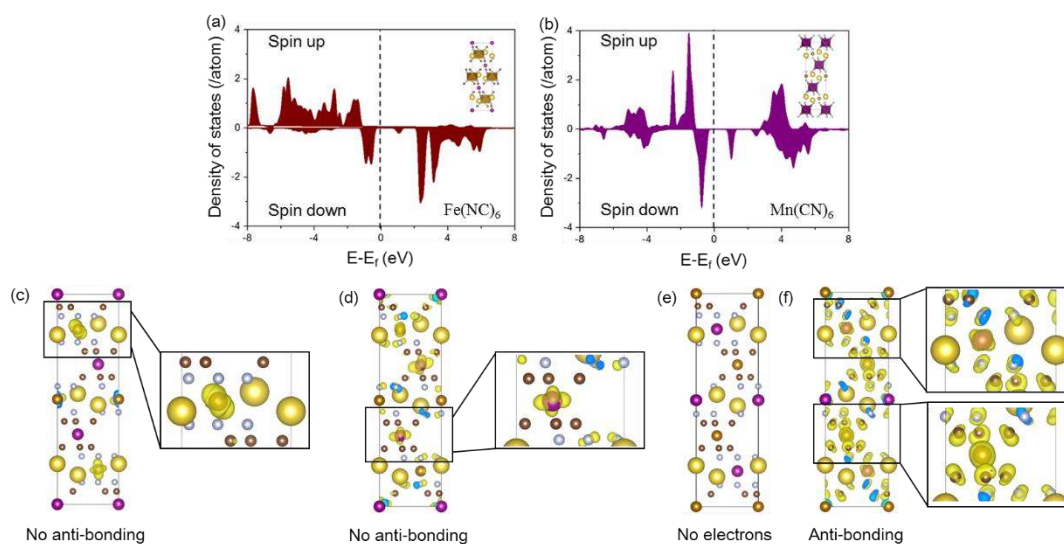
Figure D.7 The projected partial density of states (PDOS) of $3d$ electrons based on the phase of highest mixing enthalpy from Figure D.2a: (a) Fe in $Fe(NC)_6$ and (b) Mn in $Mn(CN)_6$ in $Na_2FeMn(CN)_6$. Spatial electron distribution of the unoccupied orbitals from Fermi level to 3 eV based on Fe and Mn PDOS: (c) Fe around 2.5 eV and (d) Mn around 1 eV. (e) Those of the orbitals between (e) the same range and (f) around 4.5 eV based on PDOS of Figures D.3f and D.3g.
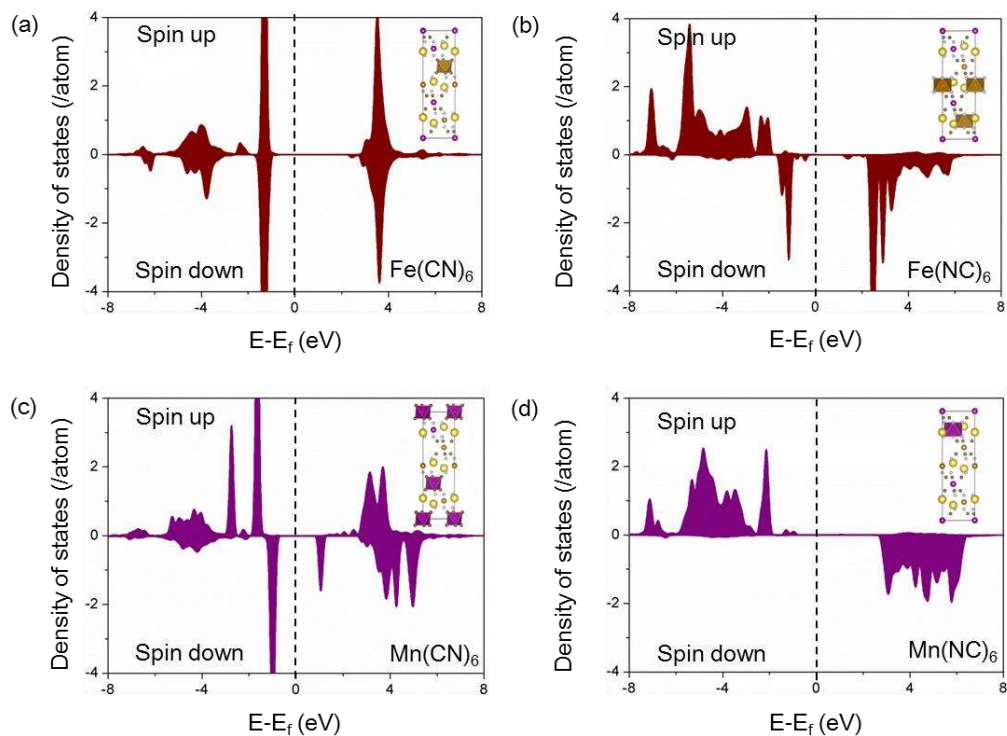
Figure D.8 The projected partial density of states (PDOS) of $3d$ electrons based on a sampled intermediate phase between the lowest and highest mixing enthalpy in $Na_2FeMn(CN)_6$ from Figure D.2a.
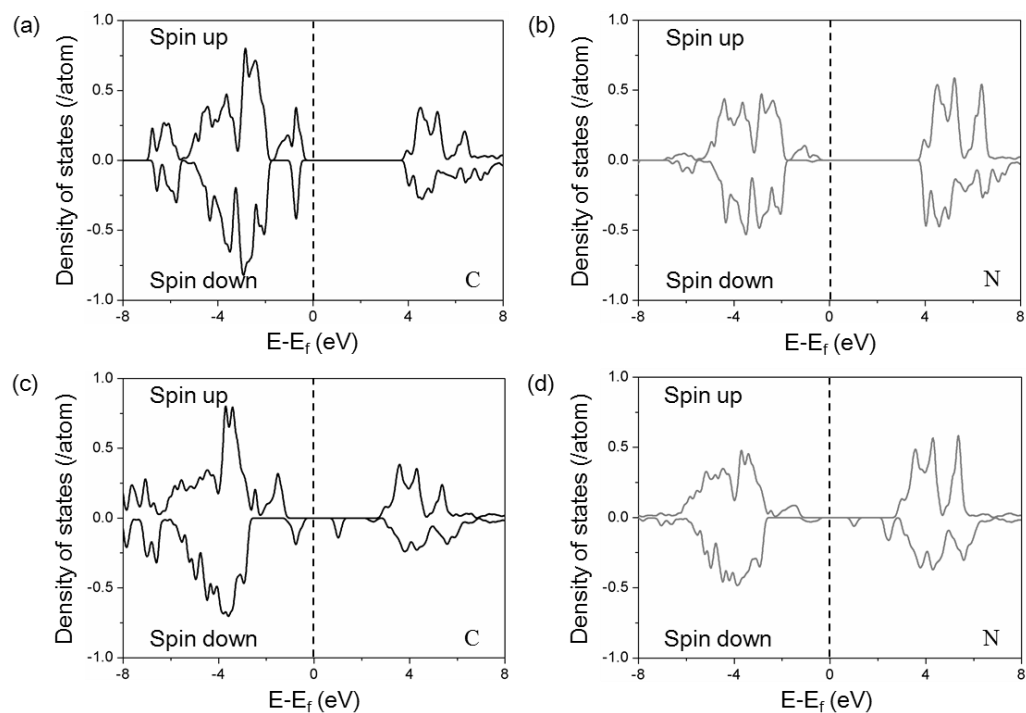
Figure D.9 The projected partial density of states (PDOS) of $2p$ electrons based on the phase of lowest mixing enthalpy ((a) C and (b) N) and the phase of highest mixing enthalpy ((c) C and (d) N) from Figure D.2a in $Na_2FeMn(CN)_6$.
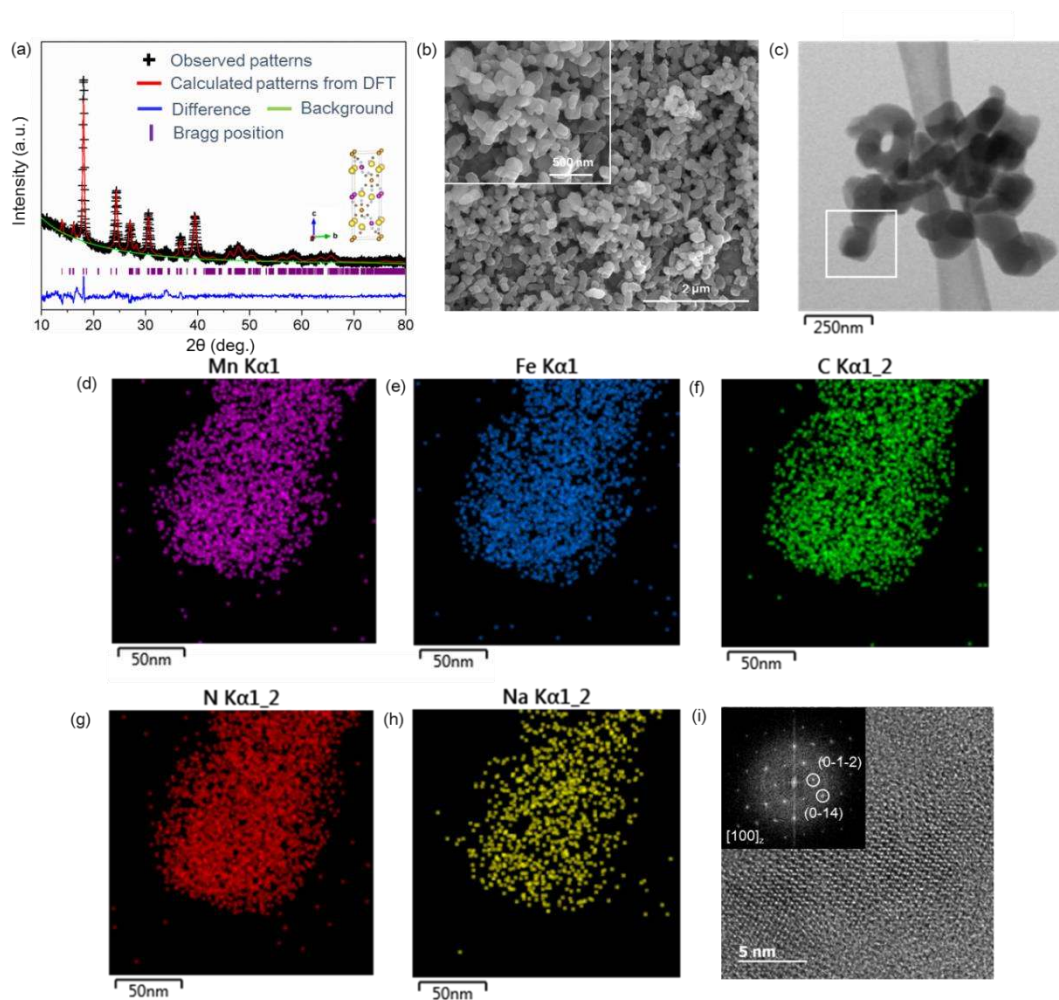
Figure D.10 (a) Rietveld refinement of the X-ray diffraction patterns of prepared NFMCN with the calculated atomic model. (b) Field emission scanning electron microscope (FESEM) and (c) scanning transmission electron microscopy (STEM) images of NFMCN. Energy dispersive X-ray spectroscopy (EDS) elemental mappings ((d) Mn: purple, (e) Fe: blue, (f) C: green, (g) N: red, and (h) Na: yellow) of the white region in (c). (i) FFT results of NFMCN with a zone axis of [100].
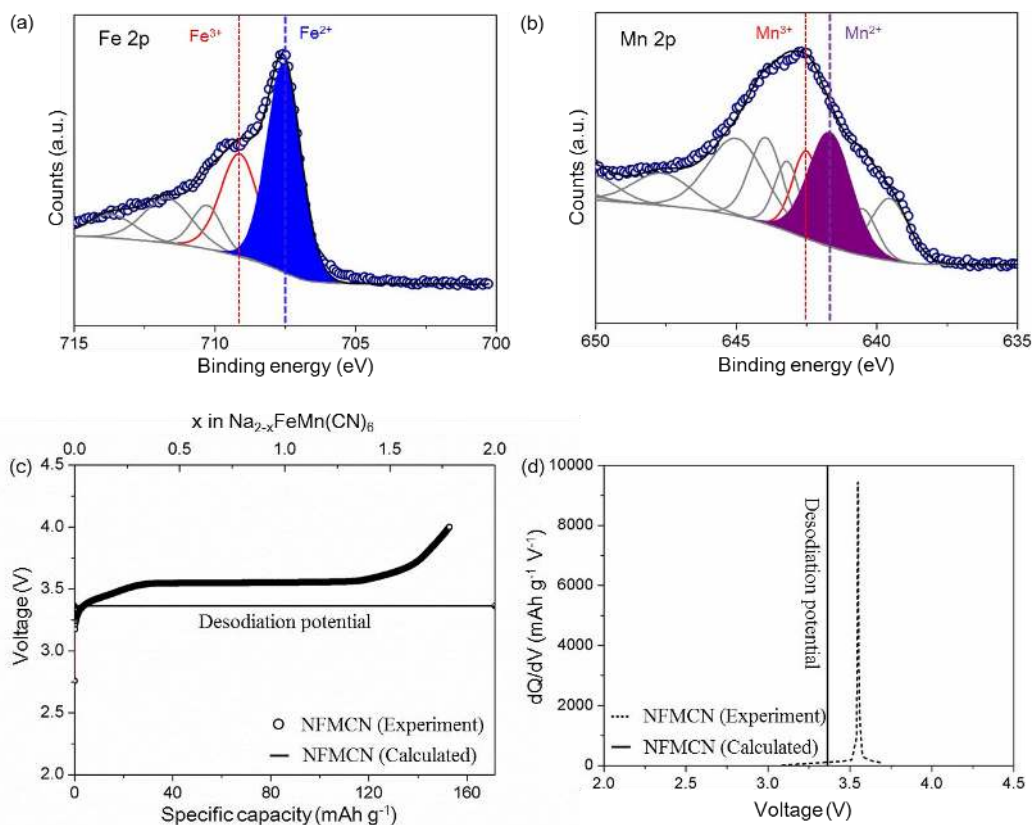
Figure D.11 (a) X-ray photoelectron spectroscopy (XPS) spectra of (a) Fe $2p$ (Fe^{2+}: ~707.5 eV and Fe^{3+}: 709.49 eV) and (b) Mn $2p$ (Mn^{2+}: ~641.6 eV and Mn^{3+}: 642.1 eV) in NFMCN. (c) combined graphs of galvanostatic charge curve of NFMCN with a constant specific current of 0.1 C rate during the first charge to 4.0 V *vs.* Na/Na$^+$ and desodiation potential calculated from first-principles for NFMCN, and (d) corresponding dQ/dV profiles with the calculated potential.
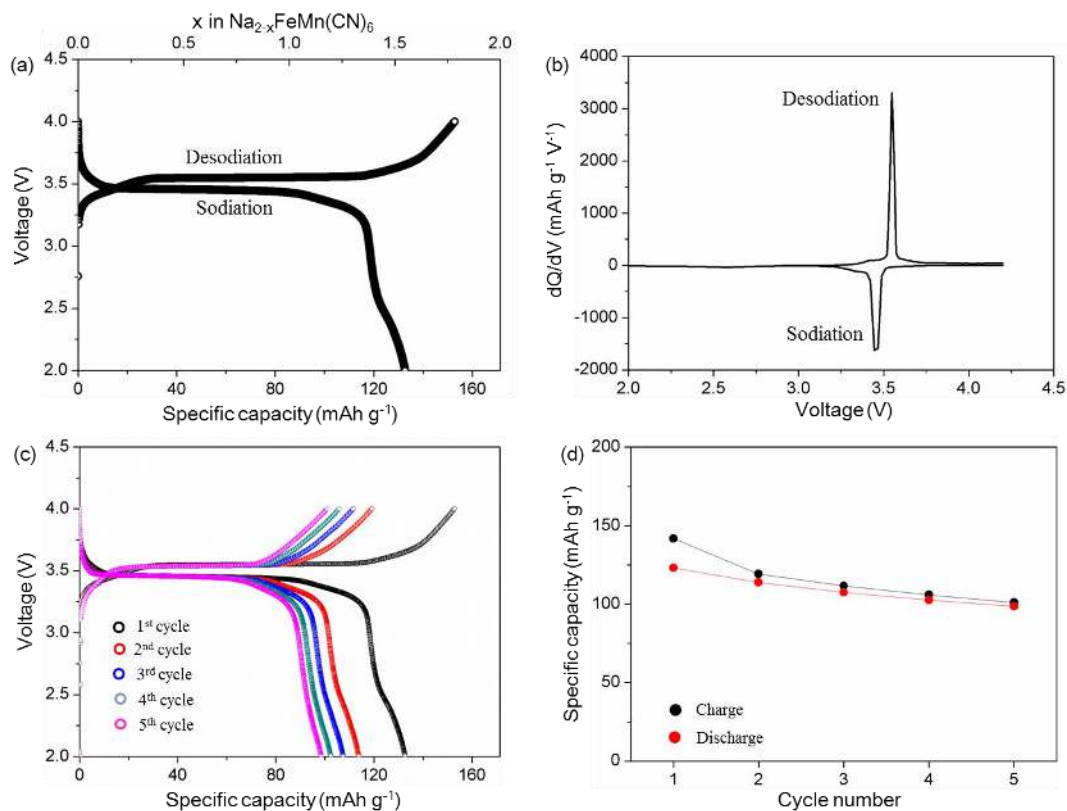
Figure D.12 (a) Initial charge (desodiation) and discharge (sodiation) curves between 2.0 V *vs*. 4.0 Na/Na$^+$ with a constant specific current of 0.1 C rate, and (b) corresponding dQ/dV profiles. (c) Charge and discharge curves from the first to fifth cycles under the same condition as (a). (d) The corresponding specific capacities as a function of cycle number.

Table D.1 Comparison of lattice parameters of NFMCN obtained from Rietveld refinement results and First-principles calculation.

Compound	Lattice parameters				R_{wp}	R_{exp}
	a (Å)		c (Å)			
	Exp.	DFT	Exp.	DFT		
NFMCN	6.5788	6.5803	18.9286	19.4447	5.77	6.42

Bibliography

1.   Kim, D.; Cho, M.; Cho, K., Rational Design of $Na(Li_{1/3}Mn_{2/3})O_2$ Operated by Anionic Redox Reactions for Advanced Sodium-Ion Batteries. *Adv Mater* **2017,** *29* (33).

2.   Tarascon, J. M.; Armand, M., Issues and challenges facing rechargeable lithium batteries. *Nature* **2001,** *414* (6861), 359-367.

3.   Yabuuchi, N.; Kubota, K.; Dahbi, M.; Komaba, S., Research Development on Sodium-Ion Batteries. *Chem Rev* **2014,** *114* (23), 11636-11682.

4.   Etacheri, V.; Marom, R.; Elazari, R.; Salitra, G.; Aurbach, D., Challenges in the development of advanced Li-ion batteries: a review. *Energ Environ Sci* **2011,** *4* (9), 3243-3262.

5.   Palomares, V.; Casas-Cabanas, M.; Castillo-Martinez, E.; Han, M. H.; Rojo, T., Update on Na-based battery materials. A growing research path. *Energ Environ Sci* **2013,** *6* (8), 2312-2337.

6.   Clement, R. J.; Bruce, P. G.; Grey, C. P., Review-Manganese-Based P2-Type Transition Metal Oxides as Sodium-Ion Battery Cathode Materials. *J Electrochem Soc* **2015,** *162* (14), A2589-A2604.

7.   Yabuuchi, N.; Kajiyama, M.; Iwatate, J.; Nishikawa, H.; Hitomi, S.; Okuyama, R.; Usui, R.; Yamada, Y.; Komaba, S., P2-type $Na_x[Fe_{1/2}Mn_{1/2}]O_2$ made from earth-abundant elements for rechargeable Na batteries. *Nat Mater* **2012,** *11* (6), 512-517.

8.   Ma, X. H.; Chen, H. L.; Ceder, G., Electrochemical Properties of Monoclinic $NaMnO_2$. *J Electrochem Soc* **2011,** *158* (12), A1307-A1312.

9.   Dunn, B.; Kamath, H.; Tarascon, J. M., Electrical Energy Storage for the Grid: A Battery of Choices. *Science* **2011,** *334* (6058), 928-935.

10.   Lim, J. M.; Kim, D.; Lim, Y. G.; Park, M. S.; Kim, Y. J.; Cho, M.; Cho, K., The origins and mechanism of phase transformation in bulk Li_2MnO_3: first-principles calculations and experimental studies. *J Mater Chem A* **2015,** *3* (13), 7066-7076.

11.   Kim, D.; Lim, J. M.; Lim, Y. G.; Park, M. S.; Kim, Y. J.; Cho, M.; Cho, K., Understanding of Surface Redox Behaviors of Li_2MnO_3 in Li-Ion Batteries: First-Principles Prediction and Experimental Validation. *Chemsuschem* **2015,** *8* (19), 3255-3262.

12.   Bo, S. H.; Li, X.; Toumar, A. J.; Ceder, G., Layered-to-Rock-Salt Transformation in Desodiated Na_xCrO_2 (x 0.4). *Chem Mater* **2016,** *28* (5), 1419-1429.

13.   Xiao, P. H.; Song, J.; Wang, L.; Goodenough, J. B.; Henkelman, G., Theoretical Study of the Structural Evolution of a $Na_2FeMn(CN)_6$ Cathode upon Na Intercalation. *Chem Mater* **2015,** *27* (10), 3763-3768.

14.   Mayo, M.; Griffith, K. J.; Pickard, C. J.; Morris, A. J., Ab Initio Study of Phosphorus Anodes for Lithium- and Sodium-Ion Batteries. *Chem Mater* **2016,** *28* (7), 2011-2021.

15.   Zhao, J.; Zhao, L. W.; Chihara, K.; Okada, S.; Yamaki, J.; Matsumoto, S.; Kuze, S.; Nakane, K., Electrochemical and thermal properties of hard carbon-type anodes for Na-ion batteries. *J Power Sources* **2013,** *244*, 752-757.

16.   Ong, S. P.; Chevrier, V. L.; Hautier, G.; Jain, A.; Moore, C.; Kim, S.; Ma, X. H.; Ceder, G., Voltage, stability and diffusion barrier differences between sodium-ion and lithium-ion intercalation materials. *Energ Environ Sci* **2011,** *4* (9), 3680-3688.

17.   Kim, H.; Yoon, G.; Park, I.; Park, K. Y.; Lee, B.; Kim, J.; Park, Y. U.; Jung, S. K.; Lim, H. D.; Ahn, D.; Lee, S.; Kang, K., Anomalous Jahn-Teller behavior in a manganese-based mixed-phosphate cathode for sodium ion batteries. *Energ Environ Sci* **2015,** *8* (11), 3325-3335.

18.   Lim, J. M.; Hwang, T.; Park, M. S.; Cho, M.; Cho, K., Design of a p-Type Electrode for Enhancing Electronic Conduction in High-Mn, Li-Rich Oxides. *Chem Mater* **2016,** *28* (22), 8201-8209.

19.   Lim, J. M.; Oh, R. G.; Cho, W.; Cho, K.; Cho, M.; Park, M. S., Power characteristics of spinel cathodes correlated with elastic softness and phase transformation for high-power lithium-ion batteries. *J Mater Chem A* **2017,** *5* (7), 3404-3411.

20.   Wang, L.; Song, J.; Qiao, R. M.; Wray, L. A.; Hossain, M. A.; Chuang, Y. D.; Yang, W. L.; Lu, Y. H.; Evans, D.; Lee, J. J.; Vail, S.; Zhao, X.; Nishijima, M.; Kakimoto, S.; Goodenough, J. B., Rhombohedral Prussian White as Cathode for Rechargeable Sodium-Ion Batteries. *J Am Chem Soc* **2015,** *137* (7), 2548-2554.

21.   You, Y.; Yu, X. Q.; Yin, Y. X.; Nam, K. W.; Guo, Y. G., Sodium iron hexacyanoferrate with high Na content as a Na-rich cathode material for Na-ion batteries. *Nano Res* **2015,** *8* (1), 117-128.

22.   Talaie, E.; Duffort, V.; Smith, H. L.; Fultz, B.; Nazar, L. F., Structure of the high voltage phase of layered P2-$Na_{2/3-z}$[$Mn_{1/2}Fe_{1/2}$]O_2 and the positive effect

of Ni substitution on its stability. *Energ Environ Sci* **2015,** *8* (8), 2512-2523.

23.   Liu, Y. H.; Fang, X.; Zhang, A. Y.; Shen, C. F.; Liu, Q. Z.; Enaya, H. A.; Zhou, C. W., Layered P2-$Na_{2/3}[Ni_{1/3}Mn_{2/3}]O_2$ as high-voltage cathode for sodium-ion batteries: The capacity decay mechanism and Al_2O_3 surface modification. *Nano Energy* **2016,** *27*, 27-34.

24.   Kubota, K.; Asari, T.; Yoshida, H.; Yaabuuchi, N.; Shiiba, H.; Nakayama, M.; Komaba, S., Understanding the Structural Evolution and Redox Mechanism of a $NaFeO_2$-$NaCoO_2$ Solid Solution for Sodium-Ion Batteries. *Adv Funct Mater* **2016,** *26* (33), 6047-6059.

25.   Clement, R. J.; Billaud, J.; Armstrong, A. R.; Singh, G.; Rojo, T.; Bruce, P. G.; Grey, C. P., Structurally stable Mg-doped P2-$Na_{2/3}Mn_{1-y}Mg_yO_2$ sodium-ion battery cathodes with high rate performance: insights from electrochemical, NMR and diffraction studies. *Energ Environ Sci* **2016,** *9* (10), 3240-3251.

26.   Komaba, S.; Yabuuchi, N.; Nakayama, T.; Ogata, A.; Ishikawa, T.; Nakai, I., Study on the Reversible Electrode Reaction of $Na_{1-x}Ni_{0.5}Mn_{0.5}O_2$ for a Rechargeable Sodium-Ion Battery. *Inorg Chem* **2012,** *51* (11), 6211-6220.

27.   Sun, J.; Lee, H. W.; Pasta, M.; Yuan, H. T.; Zheng, G. Y.; Sun, Y. M.; Li, Y. Z.; Cui, Y., A phosphorene-graphene hybrid material as a high-capacity anode for sodium-ion batteries. *Nat Nanotechnol* **2015,** *10* (11), 980-U184.

28.   Singh, P.; Shiva, K.; Celio, H.; Goodenough, J. B., Eldfellite, $NaFe(SO_4)_2$: an intercalation cathode host for low-cost Na-ion batteries. *Energ Environ Sci* **2015,** *8* (10), 3000-3005.

29.   Wang, L.; Lu, Y. H.; Liu, J.; Xu, M. W.; Cheng, J. G.; Zhang, D. W.; Goodenough, J. B., A Superior Low-Cost Cathode for a Na-Ion Battery. *Angew Chem Int Edit* **2013,** *52* (7), 1964-1967.

30.   Kim, D.; Lim, J. M.; Park, M. S.; Cho, K.; Cho, M., Phase Separation and d Electronic Orbitals on Cyclic Degradation in Li-Mn-O Compounds: First-Principles Multiscale Modeling and Experimental Observations. *Acs Appl Mater Inter* **2016,** *8* (26), 16631-16639.

31.   Kim, D.; Kang, S. H.; Slater, M.; Rood, S.; Vaughey, J. T.; Karan, N.; Balasubramanian, M.; Johnson, C. S., Enabling Sodium Batteries Using Lithium-Substituted Sodium Layered Transition Metal Oxide Cathodes. *Adv Energy Mater* **2011,** *1* (3), 333-336.

32.   Berthelot, R.; Carlier, D.; Delmas, C., Electrochemical investigation of the P2-Na_xCoO_2 phase diagram. *Nat Mater* **2011,** *10* (1), 74-U3.

33.   Yuan, D. D.; Wang, Y. X.; Cao, Y. L.; Ai, X. P.; Yang, H. X., Improved Electrochemical Performance of Fe-Substituted $NaNi_{0.5}Mn_{0.5}O_2$ Cathode

Materials for Sodium-Ion Batteries. *Acs Appl Mater Inter* **2015,** *7* (16), 8585-8591.

34.	Yue, J. L.; Zhou, Y. N.; Yu, X. Q.; Bak, S. M.; Yang, X. Q.; Fu, Z. W., O3-type layered transition metal oxide $Na(NiCoFeTi)_{1/4}O_2$ as a high rate and long cycle life cathode material for sodium ion batteries. *J Mater Chem A* **2015,** *3* (46), 23261-23267.

35.	Manikandan, P.; Ramasubramonian, D.; Shaijumon, M. M., Layered P2-type $Na_{0.5}Ni_{0.25}Mn_{0.75}O_2$ as a high performance cathode material for sodium-ion batteries. *Electrochim Acta* **2016,** *206*, 199-206.

36.	Singh, G.; Tapia-Ruiz, N.; del Amo, J. M. L.; Maitra, U.; Somerville, J. W.; Armstrong, A. R.; de Ilarduya, J. M.; Rojo, T.; Bruce, P. G., High Voltage Mg-Doped $Na_{0.67}Ni_{0.3-x}Mg_xMn_{0.7}O_2$ (x=0.05, 0.1) Na-Ion Cathodes with Enhanced Stability and Rate Capability. *Chem Mater* **2016,** *28* (14), 5087-5094.

37.	Tang, Y.; Zhang, W. X.; Xue, L. H.; Ding, X. L.; Wang, T.; Liu, X. X.; Liu, J.; Li, X. C.; Huang, Y. H., Polypyrrole-promoted superior cyclability and rate capability of $NaxFe[Fe(CN)_6]$ cathodes for sodium-ion batteries. *J Mater Chem A* **2016,** *4* (16), 6036-6041.

38.	Stournara, M. E.; Qi, Y.; Shenoy, V. B., From Ab Initio Calculations to Multiscale Design of Si/C Core-Shell Particles for Li-Ion Anodes. *Nano Lett* **2014,** *14* (4), 2140-2149.

39.	Ngandjong, A.; Rucci, A.; Maiza, M.; Shukla, G.; Vazquez-Arenas, J. G.; Franco, A. A., A Multiscale Simulation Platform Linking Lithium Ion Battery Electrode Fabrication Process With Performance At The Cell Level. *J Phys Chem Lett* **2017**.

40.	Kashkooli, A. G.; Farhad, S.; Lee, D. U.; Feng, K.; Litster, S.; Babu, S. K.; Zhu, L. K.; Chen, Z. W., Multiscale modeling of lithium-ion battery electrodes based on nano-scale X-ray computed tomography. *J Power Sources* **2016,** *307*, 496-509.

41.	Bhattacharya, P.; Viceconti, M., Multiscale modeling methods in biomechanics. *Wires Syst Biol Med* **2017,** *9* (3).

42.	Lynch, B.; Bancelin, S.; Bonod-Bidaud, C.; Gueusquin, J. B.; Ruggiero, F.; Schanne-Klein, M. C.; Allain, J. M., A novel microstructural interpretation for the biomechanics of mouse skin derived from multiscale characterization. *Acta Biomater* **2017,** *50*, 302-311.

43.	Shin, H.; Baek, K.; Han, J. G.; Cho, M., Homogenization analysis of polymeric nanocomposites containing nanoparticulate clusters. *Compos Sci Technol* **2017,** *138*, 217-224.

44.   Shin, H.; Kim, B.; Han, J. G.; Lee, M. Y.; Park, J. K.; Cho, M., Fracture toughness enhancement of thermoplastic/epoxy blends by the plastic yield of toughening agents: A multiscale analysis. *Compos Sci Technol* **2017,** *145*, 173-180.

45.   Xiang, C. X.; Weber, A. Z.; Ardo, S.; Berger, A.; Chen, Y. K.; Coridan, R.; Fountaine, K. T.; Haussener, S.; Hu, S.; Liu, R.; Lewis, N. S.; Modestino, M. A.; Shaner, M. M.; Singh, M. R.; Stevens, J. C.; Sun, K.; Walczak, K., Modeling, Simulation, and Implementation of Solar-Driven Water-Splitting Devices. *Angew Chem Int Edit* **2016,** *55* (42), 12974-12988.

46.   Friederich, P.; Gomez, V.; Sprau, C.; Meded, V.; Strunk, T.; Jenne, M.; Magri, A.; Symalla, F.; Colsmann, A.; Ruben, M.; Wenzel, W., Rational In Silico Design of an Organic Semiconductor with Improved Electron Mobility. *Adv Mater* **2017,** *29* (43).

47.   Zographos, N.; Zechner, C.; Martin-Bragado, I.; Lee, K.; Oh, Y. S., Multiscale modeling of doping processes in advanced semiconductor devices. *Mat Sci Semicon Proc* **2017,** *62*, 49-61.

48.   Cubuk, E. D.; Wang, W. L.; Zhao, K. J.; Vlassak, J. J.; Suo, Z. G.; Kaxiras, E., Morphological Evolution of Si Nanowires upon Lithiation: A First-Principles Multiscale Model. *Nano Lett* **2013,** *13* (5), 2011-2015.

49.   Tasaki, K., Solvent decompositions and physical properties of decomposition compounds in Li-ion battery electrolytes studied by DFT calculations and molecular dynamics simulations. *J Phys Chem B* **2005,** *109* (7), 2920-2933.

50.   Leung, K.; Budzien, J. L., Ab initio molecular dynamics simulations of the initial stages of solid-electrolyte interphase formation on lithium ion battery graphitic anodes. *Phys Chem Chem Phys* **2010,** *12* (25), 6583-6586.

51.   Meethong, N.; Huang, H. Y. S.; Speakman, S. A.; Carter, W. C.; Chiang, Y. M., Strain accommodation during phase transformations in olivine-based cathodes as a materials selection criterion for high-power rechargeable batteries. *Adv Funct Mater* **2007,** *17* (7), 1115-1123.

52.   Hu, S. Y.; Li, Y. L.; Rosso, K. M.; Sushko, M. L., Mesoscale Phase-Field Modeling of Charge Transport in Nanocomposite Electrodes for Lithium-Ion Batteries. *J Phys Chem C* **2013,** *117* (1), 28-40.

53.   Bai, P.; Cogswell, D. A.; Bazant, M. Z., Suppression of Phase Separation in LiFePO$_4$ Nanoparticles During Battery Discharge. *Nano Lett* **2011,** *11* (11), 4890-4896.

54.   Lim, J. M.; Kim, D.; Park, M. S.; Cho, M.; Cho, K., Underlying

mechanisms of the synergistic role of Li_2MnO_3 and $LiNi_{1/3}Co_{1/3}Mn_{1/3}O_2$ in high-Mn, Li-rich oxides. *Phys Chem Chem Phys* **2016,** *18* (16), 11411-11421.

55. Persson, K.; Hinuma, Y.; Meng, Y. S.; Van der Ven, A.; Ceder, G., Thermodynamic and kinetic properties of the Li-graphite system from first-principles calculations. *Phys Rev B* **2010,** *82* (12).

56. Wolverton, C.; Zunger, A., First-principles prediction of vacancy order-disorder and intercalation battery voltages in Li_xCoO_2. *Phys Rev Lett* **1998,** *81* (3), 606-609.

57. Mori, T.; Tanaka, K., Average Stress in Matrix and Average Elastic Energy of Materials with Misfitting Inclusions. *Acta Metall Mater* **1973,** *21* (5), 571-574.

58. Benveniste, Y., A New Approach to the Application of Mori-Tanaka Theory in Composite-Materials. *Mech Mater* **1987,** *6* (2), 147-157.

59. Latz, A.; Zausch, J., Thermodynamic derivation of a Butler-Volmer model for intercalation in Li-ion batteries. *Electrochim Acta* **2013,** *110*, 358-362.

60. Li, Y. Y.; El Gabaly, F.; Ferguson, T. R.; Smith, R. B.; Bartelt, N. C.; Sugar, J. D.; Fenton, K. R.; Cogswell, D. A.; Kilcoyne, A. L. D.; Tyliszczak, T.; Bazant, M. Z.; Chueh, W. C., Current-induced transition from particle-by-particle to concurrent intercalation in phase-separating battery electrodes. *Nat Mater* **2014,** *13* (12), 1149-1156.

61. Bai, P.; Bazant, M. Z., Charge transfer kinetics at the solid-solid interface in porous electrodes. *Nat Commun* **2014,** *5*.

62. Zhao, K. J.; Pharr, M.; Hartle, L.; Vlassak, J. J.; Suo, Z. G., Fracture and debonding in lithium-ion batteries with electrodes of hollow core-shell nanostructures. *J Power Sources* **2012,** *218*, 6-14.

63. Brassart, L.; Zhao, K. J.; Suo, Z. G., Cyclic plasticity and shakedown in high-capacity electrodes of lithium-ion batteries. *Int J Solids Struct* **2013,** *50* (7-8), 1120-1129.

64. Pharr, M.; Suo, Z. G.; Vlassak, J. J., Measurements of the Fracture Energy of Lithiated Silicon Electrodes of Li-Ion Batteries. *Nano Lett* **2013,** *13* (11), 5570-5577.

65. Sun, B.; Suo, Z.; Evans, A. G., Emergence of Cracks by Mass-Transport in Elastic Crystals Stressed at High-Temperatures. *J Mech Phys Solids* **1994,** *42* (11), 1653-&.

66. Zhang, J. P.; Zhao, X. H.; Suo, Z. G.; Jiang, H. Q., A finite element method for transient analysis of concurrent large deformation and mass transport in gels. *J Appl Phys* **2009,** *105* (12).

67.   Hassanzadeh-Aghdam, M. K.; Ansari, R.; Darvizeh, A., Micromechanical modeling of thermal expansion coefficients for unidirectional glass fiber-reinforced polyimide composites containing silica nanoparticles. *Compos Part a-Appl S* **2017,** *96*, 110-121.

68.   Occhialini, C. A.; Handunkanda, S. U.; Curry, E. B.; Hancock, J. N., Classical, quantum, and thermodynamics of a lattice model exhibiting structural negative thermal expansion. *Phys Rev B* **2017,** *95* (9).

69.   Hellenkamp, M.; Pfeifer, H., Thermally induced stresses on radiant heating tubes including the effect of fluid-structure interaction. *Appl Therm Eng* **2016,** *94*, 364-374.

70.   Partyka, P. P.; Godsey, G. A.; Galie, J. R.; Kosciuk, M. C.; Acharya, N. K.; Nagele, R. G.; Galie, P. A., Mechanical stress regulates transport in a compliant 3D model of the blood-brain barrier. *Biomaterials* **2017,** *115*, 30-39.

71.   Franco, A. A., Multiscale modelling and numerical simulation of rechargeable lithium ion batteries: concepts, methods and challenges. *Rsc Adv* **2013,** *3* (32), 13027-13058.

72.   Fang, C.; Huang, Y. H.; Zhang, W. X.; Han, J. T.; Deng, Z.; Cao, Y. L.; Yang, H. X., Routes to High Energy Cathodes of Sodium-Ion Batteries. *Adv Energy Mater* **2016,** *6* (5).

73.   Soderlind, P.; Klepeis, J. E., First-principles elastic properties of alpha-Pu. *Phys Rev B* **2009,** *79* (10).

74.   Hohenberg, P.; Kohn, W., Inhomogeneous Electron Gas. *Phys Rev B* **1964,** *136* (3b), B864-+.

75.   Kohn, W.; Sham, L. J., Self-Consistent Equations Including Exchange and Correlation Effects. *Phys Rev* **1965,** *140* (4a), 1133-&.

76.   Kresse, G.; Furthmuller, J., Efficiency of ab-initio total energy calculations for metals and semiconductors using a plane-wave basis set. *Comp Mater Sci* **1996,** *6* (1), 15-50.

77.   Perdew, J. P.; Chevary, J. A.; Vosko, S. H.; Jackson, K. A.; Pederson, M. R.; Singh, D. J.; Fiolhais, C., Atoms, Molecules, Solids, and Surfaces - Applications of the Generalized Gradient Approximation for Exchange and Correlation. *Phys Rev B* **1992,** *46* (11), 6671-6687.

78.   Hubbard, J., Electron Correlations in Narrow Energy Bands. *Proc R Soc Lon Ser-A* **1963,** *276* (1364), 238-+.

79.   Xiao, P. H.; Deng, Z. Q.; Manthiram, A.; Henkelman, G., Calculations of Oxygen Stability in Lithium-Rich Layered Cathodes. *J Phys Chem C* **2012,** *116* (44), 23201-23204.

80.   Kim, D.; Hwang, T.; Lim, J. M.; Park, M. S.; Cho, M.; Cho, K., Hexacyanometallates for sodium-ion batteries: insights into higher redox potentials using d electronic spin configurations. *Phys Chem Chem Phys* **2017,** *19* (16), 10443-10452.

81.   Van Vleck, J. H., Theory of the variations in paramagnetic anisotropy among different salts of the iron group. *Phys Rev* **1932,** *41* (2), 208-215.

82.   Kim, D.; Lim, J. M.; Lim, Y. G.; Yu, J. S.; Park, M. S.; Cho, M.; Cho, K., Design of Nickel-rich Layered Oxides Using d Electronic Donor for Redox Reactions. *Chem Mater* **2015,** *27* (18), 6450-6456.

83.   Birch, F., Finite Elastic Strain of Cubic Crystals. *Phys Rev* **1947,** *71* (11), 809-824.

84.   Cahn, J. W.; Hilliard, J. E., Free Energy of a Nonuniform System .1. Interfacial Free Energy. *J Chem Phys* **1958,** *28* (2), 258-267.

85.   Lim, J. M.; Cho, K.; Cho, M., Phase transformations with stress generations in electrochemical reactions of electrodes: Mechanics-based multiscale model for combined-phase reactions. *Extreme Mech Lett* **2017,** *11*, 89-95.

86.   Mizushima, K.; Jones, P. C.; Wiseman, P. J.; Goodenough, J. B., Li_xCoO_2 "(O<x≤1) - a New Cathode Material for Batteries of High-Energy Density. *Mater Res Bull* **1980,** *15* (6), 783-789.

87.   Cho, J.; Kim, Y. J.; Park, B., Novel $LiCoO_2$ cathode material with Al_2O_3 coating for a Li ion cell. *Chem Mater* **2000,** *12* (12), 3788-3791.

88.   Li, H.; Wang, Z. X.; Chen, L. Q.; Huang, X. J., Research on Advanced Materials for Li-ion Batteries. *Adv Mater* **2009,** *21* (45), 4593-4607.

89.   Jung, Y. S.; Lu, P.; Cavanagh, A. S.; Ban, C.; Kim, G. H.; Lee, S. H.; George, S. M.; Harris, S. J.; Dillon, A. C., Unexpected Improved Performance of ALD Coated $LiCoO_2$/Graphite Li-Ion Batteries. *Adv Energy Mater* **2013,** *3* (2), 213-219.

90.   Van der Ven, A.; Aydinol, M. K.; Ceder, G.; Kresse, G.; Hafner, J., First-principles investigation of phase stability in Li_xCoO_2. *Phys Rev B* **1998,** *58* (6), 2975-2987.

91.   Ohzuku, T.; Ueda, A.; Nagayama, M.; Iwakoshi, Y.; Komori, H., Comparative-Study of $LiCoO_2$, $LiNi_{1/2}Co_{1/2}O_2$ and $LiNiO_2$ for 4-Volt Secondary Lithium Cells. *Electrochim Acta* **1993,** *38* (9), 1159-1167.

92.   Oh, E. J.; Kim, T. W.; Lee, K. M.; Song, M. S.; Jee, A. Y.; Lim, S. T.; Ha, H. W.; Lee, M.; Choy, J. H.; Hwang, S. J., Unilamellar Nanosheet of Layered Manganese Cobalt Nickel Oxide and Its Heterolayered Film with Polycations.

Acs Nano **2010,** *4* (8), 4437-4444.

93.   Ngala, J. K.; Chernova, N. A.; Ma, M. M.; Mamak, M.; Zavalij, P. Y.; Whittingham, M. S., The synthesis, characterization and electrochemical behavior of the layered $LiNi_{0.4}Mn_{0.4}Co_{0.2}O_2$ compound. *J Mater Chem* **2004,** *14* (2), 214-220.

94.   Sun, Y. K.; Chen, Z. H.; Noh, H. J.; Lee, D. J.; Jung, H. G.; Ren, Y.; Wang, S.; Yoon, C. S.; Myung, S. T.; Amine, K., Nanostructured high-energy cathode materials for advanced lithium batteries. *Nat Mater* **2012,** *11* (11), 942-947.

95.   Hwang, B. J.; Tsai, Y. W.; Carlier, D.; Ceder, G., A combined computational/experimental study on $LiNi_{1/3}Co_{1/3}Mn_{1/3}O_2$. *Chem Mater* **2003,** *15* (19), 3676-3682.

96.   Jo, M.; Noh, M.; Oh, P.; Kim, Y.; Cho, J., A New High Power $LiNi_{0.81}Co_{0.1}Al_{0.09}O_2$ Cathode Material for Lithium-Ion Batteries. *Adv Energy Mater* **2014,** *4* (13).

97.   Wu, L. J.; Nam, K. W.; Wang, X. J.; Zhou, Y. N.; Zheng, J. C.; Yang, X. Q.; Zhu, Y. M., Structural Origin of Overcharge-Induced Thermal Instability of Ni-Containing Layered-Cathodes for High-Energy-Density Lithium Batteries. *Chem Mater* **2011,** *23* (17), 3953-3960.

98.   Jung, S. K.; Gwon, H.; Hong, J.; Park, K. Y.; Seo, D. H.; Kim, H.; Hyun, J.; Yang, W.; Kang, K., Understanding the Degradation Mechanisms of $LiNi_{0.5}Co_{0.2}Mn_{0.3}O_2$ Cathode Material in Lithium Ion Batteries. *Adv Energy Mater* **2014,** *4* (1).

99.   Xu, Z. L.; Xiao, L. L.; Wang, F.; Wu, K. C.; Zhao, L. T.; Li, M. R.; Zhang, H. L.; Wu, Q. G.; Wang, J. B., Effects of precursor, synthesis time and synthesis temperature on the physical and electrochemical properties of $Li(Ni_{1-x-y}Co_xMn_y)O_2$ cathode materials. *J Power Sources* **2014,** *253*, 433-434.

100.   Bak, S. M.; Hu, E. Y.; Zhou, Y. N.; Yu, X. Q.; Senanayake, S. D.; Cho, S. J.; Kim, K. B.; Chung, K. Y.; Yang, X. Q.; Nam, K. W., Structural Changes and Thermal Stability of Charged $LiNi_xMn_yCo_zO_2$ Cathode Materials Studied by Combined In Situ Time-Resolved XRD and Mass Spectroscopy. *Acs Appl Mater Inter* **2014,** *6* (24), 22594-22601.

101.   Conry, T. E.; Mehta, A.; Cabana, J.; Doeff, M. M., Structural Underpinnings of the Enhanced Cycling Stability upon Al-Substitution in $LiNi_{0.45}Mn_{0.45}Co_{0.1-y}Al_yO_2$ Positive Electrode Materials for Li-ion Batteries. *Chem Mater* **2012,** *24* (17), 3307-3317.

102.   Hua, W. B.; Zhang, J. B.; Zheng, Z.; Liu, W. Y.; Peng, X. H.; Guo, X. D.;

Zhong, B. H.; Wang, Y. J.; Wang, X. L., Na-doped Ni-rich $LiNi_{0.5}Co_{0.2}Mn_{0.3}O_2$ cathode material with both high rate capability and high tap density for lithium ion batteries. *Dalton T* **2014,** *43* (39), 14824-14832.

103.   Luo, W. B.; Li, X. H.; Dahn, J. R., Synthesis, Characterization, and Thermal Stability of $Li[Ni_{1/3}Mn_{1/3}Co_{1/3-z}(MnMg)_{z/2}]O_2$. *Chem Mater* **2010,** *22* (17), 5065-5073.

104.   Fey, G. T. K.; Chen, J. G.; Subramanian, V.; Osaka, T., Preparation and electrochemical properties of Zn-doped $LiNi_{0.8}Co_{0.2}O_2$. *J Power Sources* **2002,** *112* (2), 384-394.

105.   Tatsumi, K.; Sasano, Y.; Muto, S.; Yoshida, T.; Sasaki, T.; Horibuchi, K.; Takeuchi, Y.; Ukyo, Y., Local atomic and electronic structures around Mg and Al dopants in $LiNiO_2$ electrodes studied by XANES and ELNES and first-principles calculations. *Phys Rev B* **2008,** *78* (4).

106.   Sun, Y. K.; Myung, S. T.; Park, B. C.; Prakash, J.; Belharouak, I.; Amine, K., High-energy cathode material for long-life and safe lithium batteries. *Nat Mater* **2009,** *8* (4), 320-324.

107.   Cho, Y.; Oh, P.; Cho, J., A New Type of Protective Surface Layer for High-Capacity Ni-Based Cathode Materials: Nanoscaled Surface Pillaring Layer. *Nano Lett* **2013,** *13* (3), 1145-1152.

108.   Kang, K. S.; Meng, Y. S.; Breger, J.; Grey, C. P.; Ceder, G., Electrodes with high power and high capacity for rechargeable lithium batteries. *Science* **2006,** *311* (5763), 977-980.

109.   Armstrong, A. R.; Bruce, P. G., Synthesis of layered $LiMnO_2$ as an electrode for rechargeable lithium batteries. *Nature* **1996,** *381* (6582), 499-500.

110.   Thackeray, M. M.; Johnson, P. J.; Depicciotto, L. A.; Bruce, P. G.; Goodenough, J. B., Electrochemical Extraction of Lithium from $LiMn_2O_4$. *Mater Res Bull* **1984,** *19* (2), 179-187.

111.   Johnson, C. S.; Kim, J. S.; Lefief, C.; Li, N.; Vaughey, J. T.; Thackeray, M. M., The significance of the Li_2MnO_3 component in 'composite' xLi_2MnO_3 · $(1-x)LiMn_{0.5}Ni_{0.5}O_2$ electrodes. *Electrochem Commun* **2004,** *6* (10), 1085-1091.

112.   Hong, J.; Seo, D. H.; Kim, S. W.; Gwon, H.; Oh, S. T.; Kang, K., Structural evolution of layered $Li_{1.2}Ni_{0.2}Mn_{0.6}O_2$ upon electrochemical cycling in a Li rechargeable battery. *J Mater Chem* **2010,** *20* (45), 10179-10186.

113.   Mishra, S. K.; Ceder, G., Structural stability of lithium manganese oxides. *Phys Rev B* **1999,** *59* (9), 6120-6130.

114.   Mohanty, D.; Kalnaus, S.; Meisner, R. A.; Rhodes, K. J.; Li, J. L.; Payzant, E. A.; Wood, D. L.; Daniel, C., Structural transformation of a lithium-

rich $Li_{1.2}Co_{0.1}Mn_{0.55}Ni_{0.15}O_2$ cathode during high voltage cycling resolved by in situ X-ray diffraction. *J Power Sources* **2013,** *229*, 239-248.

115.   Lin, F.; Markus, I. M.; Nordlund, D.; Weng, T. C.; Asta, M. D.; Xin, H. L. L.; Doeff, M. M., Surface reconstruction and chemical evolution of stoichiometric layered cathode materials for lithium-ion batteries. *Nat Commun* **2014,** *5*.

116.   Boulineau, A.; Simonin, L.; Colin, J. F.; Canevet, E.; Daniel, L.; Patoux, S., Evolutions of $Li_{1.2}Mn_{0.61}Ni_{0.18}Mg_{0.01}O_2$ during the Initial Charge/Discharge Cycle Studied by Advanced Electron Microscopy. *Chem Mater* **2012,** *24* (18), 3558-3566.

117.   Boulineau, A.; Simonin, L.; Colin, J. F.; Bourbon, C.; Patoux, S., First Evidence of Manganese-Nickel Segregation and Densification upon Cycling in Li-Rich Layered Oxides for Lithium Batteries. *Nano Lett* **2013,** *13* (8), 3857-3863.

118.   Thackeray, M. M.; Johnson, C. S.; Vaughey, J. T.; Li, N.; Hackney, S. A., Advances in manganese-oxide 'composite' electrodes for lithium-ion batteries. *J Mater Chem* **2005,** *15* (23), 2257-2267.

119.   Thackeray, M. M.; Kang, S. H.; Johnson, C. S.; Vaughey, J. T.; Benedek, R.; Hackney, S. A., Li_2MnO_3-stabilized $LiMO_2$ (M = Mn, Ni, Co) electrodes for lithium-ion batteries. *J Mater Chem* **2007,** *17* (30), 3112-3125.

120.   Kang, S. H.; Kempgens, P.; Greenbaum, S.; Kropf, A. J.; Amine, K.; Thackeray, M. M., Interpreting the structural and electrochemical complexity of $0.5Li_2MnO_3 \cdot 0.5LiMO_2$ electrodes for lithium batteries (M = $Mn_{0.5-x}Ni_{0.5-x}Co_{2x}$, $0 \leq x \leq 0.5$). *J Mater Chem* **2007,** *17* (20), 2069-2077.

121.   Amalraj, S. F.; Markovsky, B.; Sharon, D.; Talianker, M.; Zinigrad, E.; Persky, R.; Haik, O.; Grinblat, J.; Lampert, J.; Schulz-Dobrick, M.; Garsuch, A.; Burlaka, L.; Aurbach, D., Study of the electrochemical behavior of the "inactive" Li_2MnO_3. *Electrochim Acta* **2012,** *78*, 32-39.

122.   Armstrong, A. R.; Robertson, A. D.; Bruce, P. G., Overcharging manganese oxides: Extracting lithium beyond Mn^{4+}. *J Power Sources* **2005,** *146* (1-2), 275-280.

123.   Gu, M.; Belharouak, I.; Zheng, J. M.; Wu, H. M.; Xiao, J.; Genc, A.; Amine, K.; Thevuthasan, S.; Baer, D. R.; Zhang, J. G.; Browning, N. D.; Liu, J.; Wang, C. M., Formation of the Spinel Phase in the Layered Composite Cathode Used in Li-Ion Batteries. *Acs Nano* **2013,** *7* (1), 760-767.

124.   Rana, J.; Stan, M.; Kloepsch, R.; Li, J.; Schumacher, G.; Welter, E.; Zizak, I.; Banhart, J.; Winter, M., Structural Changes in Li_2MnO_3 Cathode

Material for Li- Ion Batteries. *Adv Energy Mater* **2014,** *4* (5).

125.   Koyama, Y.; Tanaka, I.; Nagao, M.; Kanno, R., First-principles study on lithium removal from Li_2MnO_3. *J Power Sources* **2009,** *189* (1), 798-801.

126.   Armstrong, A. R.; Holzapfel, M.; Novak, P.; Johnson, C. S.; Kang, S. H.; Thackeray, M. M.; Bruce, P. G., Demonstrating oxygen loss and associated structural reorganization in the lithium battery cathode $Li[Ni_{0.2}Li_{0.2}Mn_{0.6}]O_2$. *J Am Chem Soc* **2006,** *128* (26), 8694-8698.

127.   Lee, E.; Persson, K. A., Structural and Chemical Evolution of the Layered Li-Excess Li_xMnO_3 as a Function of Li Content from First-Principles Calculations. *Adv Energy Mater* **2014,** *4* (15).

128.   Kim, J. S.; Johnson, C. S.; Vaughey, J. T.; Thackeray, M. M.; Hackney, S. A., Electrochemical and structural properties of $xLi_2M'O_3 \cdot (1-x)LiMn_{0.5}Ni_{0.5}O_2$ eIectrodes for lithium batteries (M' = Ti, Mn, Zr; $0 \leq x \leq 0.3$). *Chem Mater* **2004,** *16* (10), 1996-2006.

129.   Zhao, T. L.; Li, L.; Chen, S.; Chen, R. J.; Zhang, X. X.; Lu, J.; Wu, F.; Amine, K., The effect of chromium substitution on improving electrochemical performance of low-cost Fe-Mn based Li-rich layered oxide as cathode material for lithium-ion batteries. *J Power Sources* **2014,** *245*, 898-907.

130.   Park, M. S.; Lee, J. W.; Choi, W.; Im, D.; Doo, S. G.; Park, K. S., On the surface modifications of high-voltage oxide cathodes for lithium-ion batteries: new insight and significant safety improvement. *J Mater Chem* **2010,** *20* (34), 7208-7213.

131.   Jo, M. R.; Kim, Y. I.; Kim, Y.; Chae, J. S.; Roh, K. C.; Yoon, W. S.; Kang, Y. M., Lithium-Ion Transport through a Tailored Disordered Phase on the $LiNi_{0.5}Mn_{1.5}O_4$ Surface for High-Power Cathode Materials. *Chemsuschem* **2014,** *7* (8), 2248-2254.

132.   Lu, J.; Peng, Q.; Wang, W. Y.; Nan, C. Y.; Li, L. H.; Li, Y. D., Nanoscale Coating of $LiMO_2$ (M = Ni, Co, Mn) Nanobelts with Li^+-Conductive Li_2TiO_3: Toward Better Rate Capabilities for Li-Ion Batteries. *J Am Chem Soc* **2013,** *135* (5), 1649-1652.

133.   Liu, B.; Zhang, Q.; He, S. C.; Sato, Y. C.; Zheng, J. W.; Li, D. C., Improved electrochemical properties of $Li_{1.2}Ni_{0.18}Mn_{0.59}Co_{0.03}O_2$ by surface modification with $LiCoPO_4$. *Electrochim Acta* **2011,** *56* (19), 6748-6751.

134.   Liu, J. H.; Chen, H. Y.; Xie, J. N.; Sun, Z. Q.; Wu, N. N.; Wu, B. R., Electrochemical performance studies of Li-rich cathode materials with different primary particle sizes. *J Power Sources* **2014,** *251*, 208-214.

135.   Kim, J. S.; Kim, K.; Cho, W.; Shin, W. H.; Kanno, R.; Choi, J. W., A

Truncated Manganese Spinel Cathode for Excellent Power and Lifetime in Lithium-Ion Batteries. *Nano Lett* **2012,** *12* (12), 6358-6365.

136.   Okubo, M.; Mizuno, Y.; Yamada, H.; Kim, J.; Hosono, E.; Zhou, H. S.; Kudo, T.; Honma, I., Fast Li-Ion Insertion into Nanosized $LiMn_2O_4$ without Domain Boundaries. *Acs Nano* **2010,** *4* (2), 741-752.

137.   Put, B.; Vereecken, P. M.; Labyedh, N.; Sepulveda, A.; Huyghebaert, C.; Radu, I. P.; Stesmans, A., High Cycling Stability and Extreme Rate Performance in Nanoscaled $LiMn_2O_4$ Thin Films. *Acs Appl Mater Inter* **2015,** *7* (40), 22413-22420.

138.   Kim, D. K.; Muralidharan, P.; Lee, H. W.; Ruffo, R.; Yang, Y.; Chan, C. K.; Peng, H.; Huggins, R. A.; Cui, Y., Spinel $LiMn_2O_4$ Nanorods as Lithium Ion Battery Cathodes. *Nano Lett* **2008,** *8* (11), 3948-3952.

139.   Chung, K. Y.; Yoon, W. S.; Kim, K. B.; Yang, X. Q.; Oh, S. M., Suppression of structural fatigue by doping in spinel electrode probed by in situ bending beam method. *J Electrochem Soc* **2004,** *151* (3), A484-A492.

140.   Lu, J.; Zhan, C.; Wu, T. P.; Wen, J. G.; Lei, Y.; Kropf, A. J.; Wu, H. M.; Miller, D. J.; Elam, J. W.; Sun, Y. K.; Qiu, X. P.; Amine, K., Effectively suppressing dissolution of manganese from spinel lithium manganate via a nanoscale surface-doping approach. *Nat Commun* **2014,** *5*.

141.   Myung, S. T.; Komaba, S.; Kumagai, N., Enhanced structural stability and cyclability of Al-doped $LiMn_2O_4$ spinel synthesized by the emulsion drying method. *J Electrochem Soc* **2001,** *148* (5), A482-A489.

142.   Xiao, L. F.; Zhao, Y. Q.; Yang, Y. Y.; Cao, Y. L.; Ai, X. P.; Yang, H. X., Enhanced electrochemical stability of Al-doped $LiMn_2O_4$ synthesized by a polymer-pyrolysis method. *Electrochim Acta* **2008,** *54* (2), 545-550.

143.   Li, X.; Ma, X. H.; Su, D.; Liu, L.; Chisnell, R.; Ong, S. P.; Chen, H. L.; Toumar, A.; Idrobo, J. C.; Lei, Y. C.; Bai, J. M.; Wang, F.; Lynn, J. W.; Lee, Y. S.; Ceder, G., Direct visualization of the Jahn-Teller effect coupled to Na ordering in $Na_{5/8}MnO_2$. *Nat Mater* **2014,** *13* (6), 586-592.

144.   Cogswell, D. A.; Bazant, M. Z., Coherency Strain and the Kinetics of Phase Separation in $LiFePO_4$ Nanoparticles. *Acs Nano* **2012,** *6* (3), 2215-2225.

145.   Fouassier, C.; Delmas, C.; Hagenmuller, P., Structural Development and Physical-Properties of A_xMO_2 Phases (a=Na,K) (M=Cr,Mn,Co) (X $\leq$ 1). *Mater Res Bull* **1975,** *10* (6), 443-449.

146.   Delmas, C.; Fouassier, C.; Hagenmuller, P., Structural Classification and Properties of the Layered Oxides. *Physica B & C* **1980,** *99* (1-4), 81-85.

147.   Pramanik, M.; Tsujimoto, Y.; Malgras, V.; Dou, S. X.; Kim, J. H.;

Yamauchi, Y., Mesoporous Iron Phosphonate Electrodes with Crystalline Frameworks for Lithium-Ion Batteries. *Chem Mater* **2015,** *27* (3), 1082-1089.

148.   Hwang, S. M.; Lim, Y. G.; Kim, J. G.; Heo, Y. U.; Lim, J. H.; Yamauchi, Y.; Park, M. S.; Kim, Y. J.; Dou, S. X.; Kim, J. H., A case study on fibrous porous SnO_2 anode for robust, high-capacity lithium-ion batteries. *Nano Energy* **2014,** *10*, 53-62.

149.   Xue, H.; Zhao, J. W.; Pan, R.; Yang, B. F.; Yang, G. Y.; Liu, H. S., Diverse Ligand-Functionalized Mixed-Valent Hexamanganese Sandwiched Silicotungstates with Single-Molecule Magnet Behavior. *Chem-Eur J* **2016,** *22* (35), 12322-+.

150.   Delmas, C.; Braconnier, J. J.; Fouassier, C.; Hagenmuller, P., Electrochemical Intercalation of Sodium in Na_xCoO_2 Bronzes. *Solid State Ionics* **1981,** *3-4* (Aug), 165-169.

151.   Zandbergen, H. W.; Foo, M.; Xu, Q.; Kumar, V.; Cava, R. J., Sodium ion ordering in Na_xCoO_2: Electron diffraction study. *Phys Rev B* **2004,** *70* (2).

152.   Guignard, M.; Didier, C.; Darriet, J.; Bordet, P.; Elkaim, E.; Delmas, C., P2-Na_xVO_2 system as electrodes for batteries and electron-correlated materials. *Nat Mater* **2013,** *12* (1), 74-80.

153.   Lu, Z. H.; Dahn, J. R., In situ X-ray diffraction study of P2-$Na_{2/3}[Ni_{1/3}Mn_{2/3}]O_2$. *J Electrochem Soc* **2001,** *148* (11), A1225-A1229.

154.   Li, X.; Wu, D.; Zhou, Y. N.; Liu, L.; Yang, X. Q.; Ceder, G., O3-type $Na(Mn_{0.25}Fe_{0.25}Co_{0.25}Ni_{0.25})O_2$: A quaternary layered cathode compound for rechargeable Na ion batteries. *Electrochem Commun* **2014,** *49*, 51-54.

155.   de Boisse, B. M.; Carlier, D.; Guignard, M.; Delmas, C., Structural and Electrochemical Characterizations of P2 and New O3-$Na_xMn_{1-y}Fe_yO_2$ Phases Prepared by Auto-Combustion Synthesis for Na-Ion Batteries. *J Electrochem Soc* **2013,** *160* (4), A569-A574.

156.   Oh, S. M.; Myung, S. T.; Hwang, J. Y.; Scrosati, B.; Amine, K.; Sun, Y. K., High Capacity O3-Type $Na[Li_{0.05}(Ni_{0.25}Fe_{0.25}Mn_{0.5})_{0.95}]O_2$ Cathode for Sodium Ion Batteries. *Chem Mater* **2014,** *26* (21), 6165-6171.

157.   Oh, S. M.; Myung, S. T.; Yoon, C. S.; Lu, J.; Hassoun, J.; Scrosati, B.; Amine, K.; Sun, Y. K., Advanced $Na[Ni_{0.25}Fe_{0.5}Mn_{0.25}]O_2/C-Fe_3O_4$ Sodium-Ion Batteries Using EMS Electrolyte for Energy Storage. *Nano Lett* **2014,** *14* (3), 1620-1626.

158.   Xu, J.; Lee, D. H.; Clement, R. J.; Yu, X. Q.; Leskes, M.; Pell, A. J.; Pintacuda, G.; Yang, X. Q.; Grey, C. P.; Meng, Y. S., Identifying the Critical Role of Li Substitution in P2-$Nax[Li_yNi_zMn_{1-y-z}]O_2$ $(0 < x, y, z < 1)$ Intercalation

Cathode Materials for High-Energy Na-Ion Batteries. *Chem Mater* **2014,** *26* (2), 1260-1269.

159. Song, J.; Wang, L.; Lu, Y. H.; Liu, J.; Guo, B. K.; Xiao, P. H.; Lee, J. J.; Yang, X. Q.; Henkelman, G.; Goodenough, J. B., Removal of Interstitial H2O in Hexacyanometallates for a Superior Cathode of a Sodium-Ion Battery. *J Am Chem Soc* **2015,** *137* (7), 2658-2664.

160. Ling, C.; Chen, J. J.; Mizuno, F., First-Principles Study of Alkali and Alkaline Earth Ion Intercalation in Iron Hexacyanoferrate: The Important Role of Ionic Radius. *J Phys Chem C* **2013,** *117* (41), 21158-21165.

161. Wessells, C. D.; Huggins, R. A.; Cui, Y., Copper hexacyanoferrate battery electrodes with long cycle life and high power. *Nat Commun* **2011,** *2*.

162. Wessells, C. D.; McDowell, M. T.; Peddada, S. V.; Pasta, M.; Huggins, R. A.; Cui, Y., Tunable Reaction Potentials in Open Framework Nanoparticle Battery Electrodes for Grid-Scale Energy Storage. *Acs Nano* **2012,** *6* (2), 1688-1694.

국문 요약

양극재료에서 원자단위부터 매크로 단위까지 발생하는 복잡한 물리적·화학적 반응때문에, 소듐 이온 전지에서의 새로운 고 에너지 밀도 양극재료를 발견하기 위해서는 멀티스케일 설계 접근법에 기반한 합리적인 설계가 필수적인 방법으로 고려 되어진다. 본질적으로 리튬 이온보다 큰 소듐 이온의 반지름을 고려했을때, 소듐 이온 전지의 양극재료들은 소듐 이온의 삽입 탈리 때문에 리튬 이온 전지의 양극 재료들과 비교하여 극심한 구조적 변화와 상 전이들이 전기화학 반응들과 동반하여 작동이 되어지며, 이러한 변화들이 충/방전 동안에 사이클을 저하시킨다. 즉, 원자단위에서의 소듐이동은 양극재료의 정성적·정량적 변화에 영향을 주며, 이는 곧 전체 시스템의 전기화학적 성능의 결과들이 된다. 게다가, 리튬 이온 전지의 양극재료와 비교하여 소듐 이온 전지의 양극재료는 본질적으로 산화/환원 전위 약 0.3 V 가 낮아 저 에너지 밀도 특징을 보이게 된다. 그러므로, 그 두가지 근본적인 소듐 이온의 특성을 고려한 멀티스케일 기반 분석과 설계 접근법은 소듐 이온 전지에서의 합리적인 양극재료 설계에 있어 대단히 중요하다.

원자단위 관점에서의 상 안정도와 관련한 열역학적 혼합 엔탈피, 운동학적 성질, 기계적 상수값, 기계화학적 변형, 그리고 정성적·정량적 전자 구조를 포함하는 제일원리계산에서부터 원자 계산의 열역학적 값과 결합된 균일한 자유에너지로부터 얻어지는 균일한 화학적 전위로 구성되어진 상 분리 시뮬레이션 뿐만 아니라 다항식 함수의 의해 피팅된 기계적 상수값과 기계화학적 변형으로부터 얻어진 기계화학적 응력까지의 멀티스케일 기반 체계를 사용하여 기존 반응 메커니즘(양이온 산화/환원)을 넘어서는 새로운 반응 패러다임(음이온 산화/환원)에 의해 작동되는 소듐 이온 전지의 고 에너지 밀도 양극 재료인 $Na(Li_{1/3}Mn_{2/3})O_2$ (고 전압/충전용량: 소듐 금속 대비 ~4.2V/190mAh g^{-1})를 합리적으로 설계함과 동시에 실험적으로 현실화했다. 이러한 신규 양극 재료의 설계는 리튬 이온

전지 양극 재료인 Li_2MnO_3 의 깊이 있는 이해로부터 수행 되어졌다. 더 나아가, 이렇게 합리적으로 설계된 $Na(Li_{1/3}Mn_{2/3})O_2$ 는 소듐 이온 전지의 진보를 위한 유망한 양극 재료들($Na(Li_{1/3}M_{2/3})O_2$, M : 안정된 M^{4+}특징을 갖는 전이금속)의 신규 물질군의 한가지 예이다.

앞서 새롭게 발견된 $Na(Li_{1/3}Mn_{2/3})O_2$ 재료에서 충/방전 성능과 관련된 상 변화·상 분리와 구조적 붕괴의 문제점을 극복하기 위해서 고 에너지 밀도 양극재인 $Na(Li_{1/3}Mn_{1/2}Cr_{1/6})O_2$ 를 추가적으로 설계했다. 본 소재는 $Na(Li_{1/3}Mn_{2/3})O_2$ 와 비교하여 줄어든 상 변화, 낮은 상 분리 운동학, 그리고 낮은 기계화학적인 변형과 응력을 포함하면서 Cr 의 3d 전자와 O 2p 전자를 전기화학반응에 활용한다. 게다가, 미래 소듐 이온 전지에서의 음이온 산화/환원 반응 사용에 대한 합리적인 통찰력을 제공하기 위하여 좋은 충/방전 성능을 가지는 $Na(Li_{1/3}Mn_{1/2}Cr_{1/6})O_2$ 는 우수한 물질 유사체들($Na(Li_{1/3}M_{2/3(1-y)}M_{cy})O_2$, M : 안정된 M^{4+}특징을 갖는 전이금속, M_c : 활성 양이온 산화/환원 반응을 가지는 M_c^{4+} 전이금속)의 중요한 예로써 고려 되어진다.

멀티스케일 기반 설계 접근법에 의해서 합리적으로 설계되고 실험적으로 검증된 양극 재료들은 소듐 이온 전지에서의 양극 재료의 저 에너지 밀도 한계성을 극복할 수 있는 방향성을 제시한다. 더 나아가, 현재의 멀티스케일 설계 접근법은 다양한 에너지 관련 시스템인 배터리, 캐패시터, 연료전지, 태양전지, 그리고 촉매의 성능을 향상시키고 신규 물질들을 설계하기 위한 목적으로 적용이 가능할 것이다.

주요어: 멀티스케일 설계, 제일원리계산, 상 분리 운동학, 소듐 이온 전지, 화학역학

학번: 2012-23936